Exhumation history of the deepest central Himalayan rocks (Ama Drime range): key P-T-D-t constraints on orogenic models.

E. Kali (1); P.H. Leloup (2); N. Arnaud (3); G. Mahéo (2); Dunyi Liu (4); E. Boutonnet (2); J. VanderWoerd (1); Liu Xiaohan (5); Jing Liu-Zeng (5); Li Haibing (4).

(1) Institut de Physique du Globe de Strasbourg (CNRS, UdS/EOST), UMR 7516, Strasbourg, France
(2) LST, Université de Lyon, ENS Lyon, UCB Lyon1, CNRS UMR 5570. bat Géode, 43 Bd du 11 Novembre 1918, 69622, Villeurbanne cedex, France.
(3) Géosciences Montpellier, Université de Montpellier2, Montpellier France.
(4) Laboratory of Continental Dynamics, Institute of Geology, CAGS, Beijing, China
(5) Institute of Tibetan Plateau Research, Chinese Academy of Sciences, Beijing, China

Abstract
The Ama Drime range located at the transition between the high Himalayan range and South Tibet is a N-S active horst that offsets the STDS. Within the horst, a paragneissic unit, possibly attributed to the UHCS, overly the LoHCS Ama Drime orthogneissic unit containing large metabasite layers and pods that have experienced pressure ≥ 1.4 GPa. Combining structural analysis with new and published P-T estimates as well as U-Th/Pb, $^{39}Ar/^{40}Ar$ and (U-Th)/He ages, the PTtD paths of the main units within and on both sides of the horst are reconstructed. They imply that N-S normal faults initiated prior to 11 Ma, and have accounted for a total exhumation ≤ 0.6 GPa (22km) that probably occurred in two phases: the first one until ~9 Ma and the second one since 6 to 4 Ma at a rate of ~1mm/yr. In the Ama Drime unit, 1 to 1.3 GPa (37 to 48 km) of exhumation occurred after partial melting since ~30 Ma until ~13 Ma, above the MCT and below the STDS when these two fault systems were active together. The switch from E-W (STDS) to N-S (Ama Drime horst) normal faulting between 13 and 12 Ma occurs at the time of propagation of thrusting from the MCT to the MBT. These data are in favor of a wedge extrusion or thrust system rather than a crustal flow model for the building of the Himalaya. We propose that the kinematics of south Tibet Cenozoic extension phases is fundamentally driven by the direction and rate of India underthrusting.

1 Introduction
Syn-convergence arc-parallel and arc-perpendicular extension phases have taken place in mountain ranges such as the Himalaya-Tibet and the Alps, focusing the attention of many scientists that discuss their rheological / kinematics significance. In the Himalaya-Tibet orogen, arc-perpendicular extension is mostly related to Miocene top-to-the-north normal faulting along the South Tibetan Detachment System (STDS, Burg et al., 1984; Burchfiel et al., 1992). This structure has been linked either to gravitational collapse of the range (Dewey, 1988), or thrusting of Himalayan crystalline slab (HCS) above the Main Central Trust (MCT). Some authors consider that the HCS was extruded in a thrust wedge (i.e. Burchfiel & Royden, 1985; Grujic et al., 1996; Guillot & Allemand, 2002, Webb et al., 2007), while other make it a result of ductile channel flow (Nelson et al., 1996; Beaumont et al., 2001; Jamieson et al., 2004). Arc parallel extension is accommodated by

numerous N-S trending normal faults that affect South Tibet with few of them extending across the high Himalayan chain (Molnar & Tapponnier, 1978; Tapponnier et al., 1981; Armijo et al., 1986). Such extension has been attributed either to dissipation of excess potential energy accumulated, either during the thickening of the Asian margin (Molnar & Tapponnier, 1978) or during uplift of the plateau following detachment of the upper mantle part of the Asian lithosphere (e.g. England & Houseman, 1989), or to accommodation of boundary forces and displacements (e.g., Armijo et al., 1986; Yin, 2000; Tapponnier et al., 2001).

In a few localities, such as the Nyainqentanglha graben (Pan & Kidd, 1992), the Gurla-Mandata dome (Murphy et al., 2002), the Lunggar rift (Kapp et al., 2008) and Dinggye rift (e.g., Burchfiel et al., 1992) ductile deformation related to N-S active normal faults has been observed. Most authors consider that ductile and brittle structures are related to the same, continuous extension phase (Harrison et al., 1995; Kapp et al., 2008; Cottle et al., 2009). However, initiation of normal faulting in the KungCo graben has been dated at ≤ 4 Ma, implying that two successive arc-perpendicular extension episodes may have taken place in South Tibet, one around 10-12 Ma and another since ~4-6 Ma (Mahéo et al., 2007).

In order to quantify the amount and clarify the mechanisms of rock exhumation in the HCS, and constrain the timing of arc-perpendicular and arc-parallel extensions in south Tibet, we performed a detailed structural, petrologic and thermochronologic study of the Ama Drime range located at the southern end of the Xainza-Dinggye rift. The targeted area is located northeast of the Chomolangma – Makalu massif of the Himalayan range (Fig. 1). The Ama Drime range is a key area for at least four reasons. a) The Ama Drime is located at the transition between the high chain and the Tibetan plateau, where the STDS is crosscut by N-S active normal faults (Fig. 1b), allowing assessment of the relative and absolute timing of these structures. b) Arc-parallel extension is in brittle and ductile domains so that the continuity of the deformation can be addressed. c) The Ama Drime range contains the only eclogite found so far in the central Himalayas (Lombardo & Rolfo 2000, Groppo et al., 2007) implying exhumation of deep-seated rocks that can be used to quantify the magnitudes of vertical and horizontal movements between the MCT and the STDS. d) The Arun-Phung Chu river that flows along the Ama Drime, is one of the few rivers that leaves the Tibetan Plateau by crossing the central Himalayan chain in between the syntaxes, bringing up the issue of the relation between erosion and exhumation.

Our integrated approach combining structural geology, geomorphology, petrography and multi-method geochronology aims at deciphering and quantifying the structural history of the Ama Drime area and the (P-T-t) evolution of the continental crust, to bring important constraints on orogenic lithospheric deformation models.

2 geological setting

Near the Tibet – Nepal – Sikkim borders a ~150 km stretch of the Himalayan range encompass 4 of the 5 highest summits on Earth, including the Chomolangma (Everest) (8848 m *asl*, Fig. 1b). The Arun – Phung Chu river, flowing towards the South from Tibet, has cut down to ~2200 m *asl* across the range, less than 30 km away from the Makalu summit (8485 m *asl*) (Fig. 1b). Headwards, the Arun River is flowing along the western flank of the Ama Drime range, the only significant topographic range protruding from the Himalaya to the north (Fig. 1b).

The North-South Arun valley provides a complete geological cross section across the central Himalayas. The main litho-tectonic units define stripes, more or less parallel to the range, dipping to the north and separated by major tectonic contacts (Fig. 1b). The central unit, the Himalayan crystalline series (HCS) is a sliver of gneiss and granites, sandwiched between less metamorphosed rocks (Fig. 1b & c). To the bottom (South) the HCS rests on the phyllites and quartzites of the Lesser Himalaya (LH, Tumlingtar unit of Lombardo et al., 1993). To the top (North) the HCS is separated from the weakly metamorphosed Tethyan sedimentary series (TSS) by the South Tibetan detachment (STD).

There has been debate on the internal litho-tectonic subdivision of the HCS. Within the Arun area two main litho-tectonic units have been distinguished within the HCS (e.g., Bordet, 1961; Brunel, 1983; Groppo et al. 2007): the Lesser and Greater Himalayan crystalline sequences (LHCS and GHCS, respectively). The base of the GHCS corresponds to a thrust zone, locally termed ”Barun thrust” whose hanging wall is marked by discontinuous exposure of the Barun orthogneiss (Brunel, 1983). That thrust zone has been considered by some as the main central thrust (MCT of Brunel [1983] and Goscombe & Hand [2000]). Goscombe et al. (2006) also consider it as the main structure of the belt and termed it « High Himal Thrust » (HHT) (Fig. 1b). Most of the GHCS consists of paragneiss and amphibolites, often migmatitic (Brunel, 1983; Lombardo et al., 1993), intruded by Miocene leucogranites including huge laccolithes such as the Makalu-Cho Oyu leucogranite (e.g., Borghi et al., 2003). Towards the top of the GHCS all rocks, except very few late dykes, are affected by ductile, top to the Northeast, ductile shearing in STD shear zone (Burg et al., 1984; Burchfiel et al., 1992; Carosi et al., 1998; Cottle et al., 2007).

Below the GHCS, the LHCS is mostly composed of metapelites overlying the Num / Ulleri orthogneiss (Bordet, 1961; Brunel, 1983; Goscombe et al., 2006). The LHCS series belongs in fact to two distinct basinal sequences deposited on the Indian passive margin, the Mesoproterozoic Lesser Himalayan Sequence and the Neoproterozoic–Cambrian Greater Himalayan Sequence, separated by the Himalayan unconformity (HU) (Goscombe et al., 2006). The LHCS is strongly deformed, is bounded at its base by mylonites and thrust sheets (Bordet, 1961; Meier and Hiltner, 1993), and has often been referred as the MCT zone. The basal contact of the LHCS will be referred here as the Main Central Thrust or MCT (MCT2 of Arita [1983], MCT of Heim and Gansser [1939], Le Fort [1975], DeCelles et al. [2001], and Goscombe et al [2006]).

In order to avoid the ambiguities resulting from various definitions of the MCT and of the GHCS and LHCS series we use in the following a structural terminology: the upper Himalayan crystalline series (UHCS) corresponds to the series bounded at their top by the STDS and at their bottom by the HHT as mapped by Goscombe et al. (2006) (Fig. 1b). The lower Himalayan crystalline series (LoHCS) are bounded at their top by the HHT and are their bottom by the MCT as mapped by Goscombe et al (2006) (Fig. 1b).

In map view, the range-parallel orientation of the MCT and parallel thrusts are locally sinuous, particularly around the main rivers flowing down from the Himalayas

(Fig. 1b). Along the Arun river, such map pattern is attributed to the Arun anticline with a ~N-S axis (Bordet, 1961), and some (e.g., Borghi et al., 2003; Liu et al., 2007) have interpreted the Ama Drime range as the northern prong of the Arun anticline. There is still considerable debate whether the main structures can be traced at the scale of the whole orogen but one possible interpretation is that two main thrusts can be traced for several hundreds of kilometers: the upper MCT (MCTu, joining the Vaikrita, Mahbharat, Chomrong, Barun, HHT and Kakhtang thrusts) and the lower MCT (MCTl joining the Ramgarh and Munsiari thrusts).

3 Geology and structure of the Ama Drime range and the Dinggye – Kharta area.

3.1 Topography, morphology and active tectonics

The Ama Drime range exhibits a double-crested horst morphology that is mostly controlled by active normal faults (Armijo et al., 1986). The range displays several peaks over 6000 m *asl*, the highest being the Nyonno Ri (6730 m *asl*) (Fig. 2a, Fig. DR7). To the East, the range shows for more than 50 km a very steep linear NNE-SSW crest at 5000 to 6700 m *asl*. This 500 to 1000 m high wall is bounded by a ~50° east dipping active normal fault, the Dinggye fault, whose recent activity is attested by spectacular triangular facets and offset moraine ridges (Armijo et al., 1986; Zhang and Guo, 2007; Fig. 3aa). To the west, the Arun River flows parallel to the west dipping Kharta active normal fault (Fig. 2a). The active fault length is shorter (~30 km) than the Dinggye fault and the elevation of the western Ama Drime crest is slightly lower than to the east, but the flank is steeper and the activity of the fault attested by ~1500 m high triangular facets, fluvial terraces and moraines offsets (Fig. 3ab, c).

On both sides of the range, quartz cataclasite outcrops on the topographic scarps (Fig. 3aa, c). Brittle faults strike almost N-S, and generally dip steeply (~45 to 55° on average) to the west on the western side of the range and to the east on the eastern one, in good accordance with the geometry of the active faults deduced from the morphology (Fig. 2a; Fig. 4e, f, g, h, k, m). Slickensides when present indicate almost pure dip slip motions (Fig. 4). On the eastern side of the range, normal faults parallel to the Dinggye fault slice the foothills to at least 5 km away from the topographic front and have tilted to the west the metamorphic series of the STD shear zone (Fig. 2b-1).

Fig. 1: Structure of the central high Himalayas.
a) Simplified geological frame of the India –Asia continental collision. **b)** Simplified structural map of the Himalayas between the Cho Oyu and the Kangchengjunga. Shaded SRTM DEM is shown in background by transparency in the colur version. The South Tibet Detachment (STD) and the North Himalayan domes have been mapped from the interpretation of Landsat 7 satellite data checked against personal field observations and published maps (e.g., Burchfiel et al., 1992; Carosi et al., 1998; Searle, 2007). The HHT (Barun thrust) and MCT are from Goscombe et al. (2006) and Harris et al. (2004). Active faults appear in red and are from Armijo et al. (1986), Landsat 7 satellite data interpretation and field observations. Projection is UTM 45. The grey thick line corresponds to the trace of Fig. 1c cross-section. **c)** Simplified generalized cross section of the Himalayas. NNE – SSW interpretative cross section at ~87°E, few kilometres west of the Ama Drime range. Main geological units as in Fig. 1b, and main structures geometry from Bollinger et al. (2004). The green (colour version) or continuous (b & w version) line corresponds to the upper relief (i.e., Chomolangma) and the blue (colour version) or dashed (b & w version) line to the lower relief (i.e., Arun valley), no vertical exaggeration. The box indicates the approximate location of the Ama Drime rock before their exhumation in the horst (see Fig. 12b). TSS, Tethyan sedimentary series; HCS, Himalayan crystalline series, UHCS, upper Himalayan crystalline series; LoHCS, lower Himalayan crystalline series; LH Lesser Himalaya series; ADP, Ama Drime paragneisses; ADO, AmaDrime orthogneisses; STDS, South Tibet detachment system; HHT, High Himal Thrust; MCT, Main central thrust; MBT, Main boundary thrust; see text section 2 for definitions.

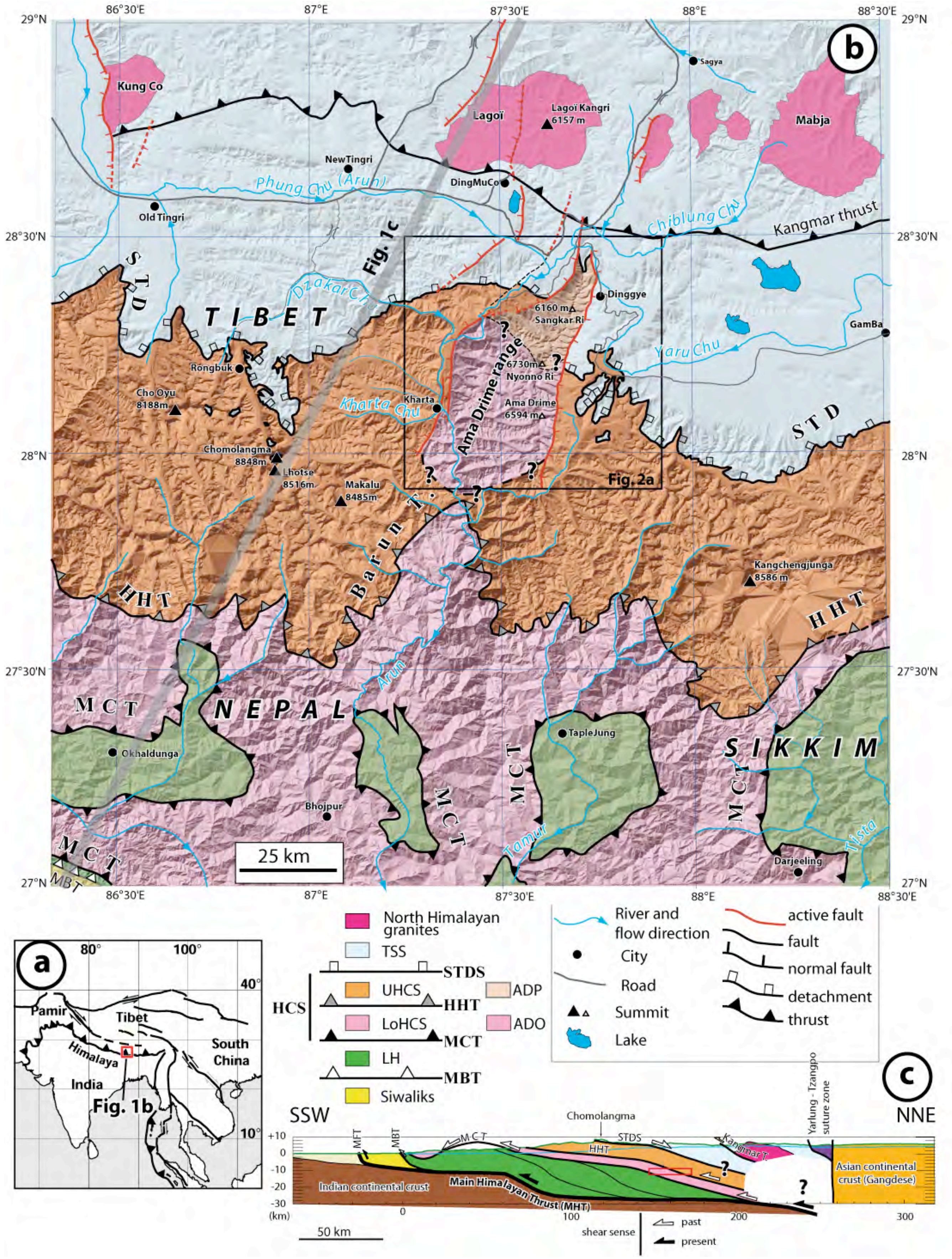

b
Kung Co
Lagoï
Lagoï Kangri 6157 m
Mabja
Sagya
NewTingri
DingMuCo
Old Tingri
Phung Chu (Arun)
Chiblung Chu
Kangmar thrust
Fig. 1c
STD
TIBET
Dzakar Chu
Dinggye
6160 m Sangkar Ri
GamBa
Yaru Chu
Rongbuk
6730m Nyonno Ri
Ama Drime range
Cho Oyu 8188m
Kharta
Kharta Chu
Ama Drime 6594 m
Chomolangma 8848m
Lhotse 8516m
Makalu 8485m
Fig. 2a
Barun T.
HHT
Kangchengjunga 8586 m
MCT
NEPAL
Arun
Okhaldunga
TapleJung
SIKKIM
Bhojpur
25 km
Tamur
Darjeeling
Tista
MBT
29°N
28°30'N
28°N
27°30'N
27°N
86°30'E
87°E
87°30'E
88°E
88°30'E
a
80°
100°
40°
10°
Pamir
Tibet
Himalaya
South China
India
Fig. 1b
North Himalayan granites
TSS
STDS
HCS
UHCS
HHT
ADP
LoHCS
ADO
MCT
LH
MBT
Siwaliks
River and flow direction
City
Road
Summit
Lake
active fault
fault
normal fault
detachment
thrust
c
SSW
NNE
Chomolangma
Yarlung - Tzangpo suture zone
MFT
MBT
MCT
STDS
HHT
Kangmar T.
Indian continental crust
Main Himalayan Thrust (MHT)
Asian continental crust (Gangdese)
+10
0
-10
-20
-30
(km)
0
100
200
300
50 km
shear sense
past
present

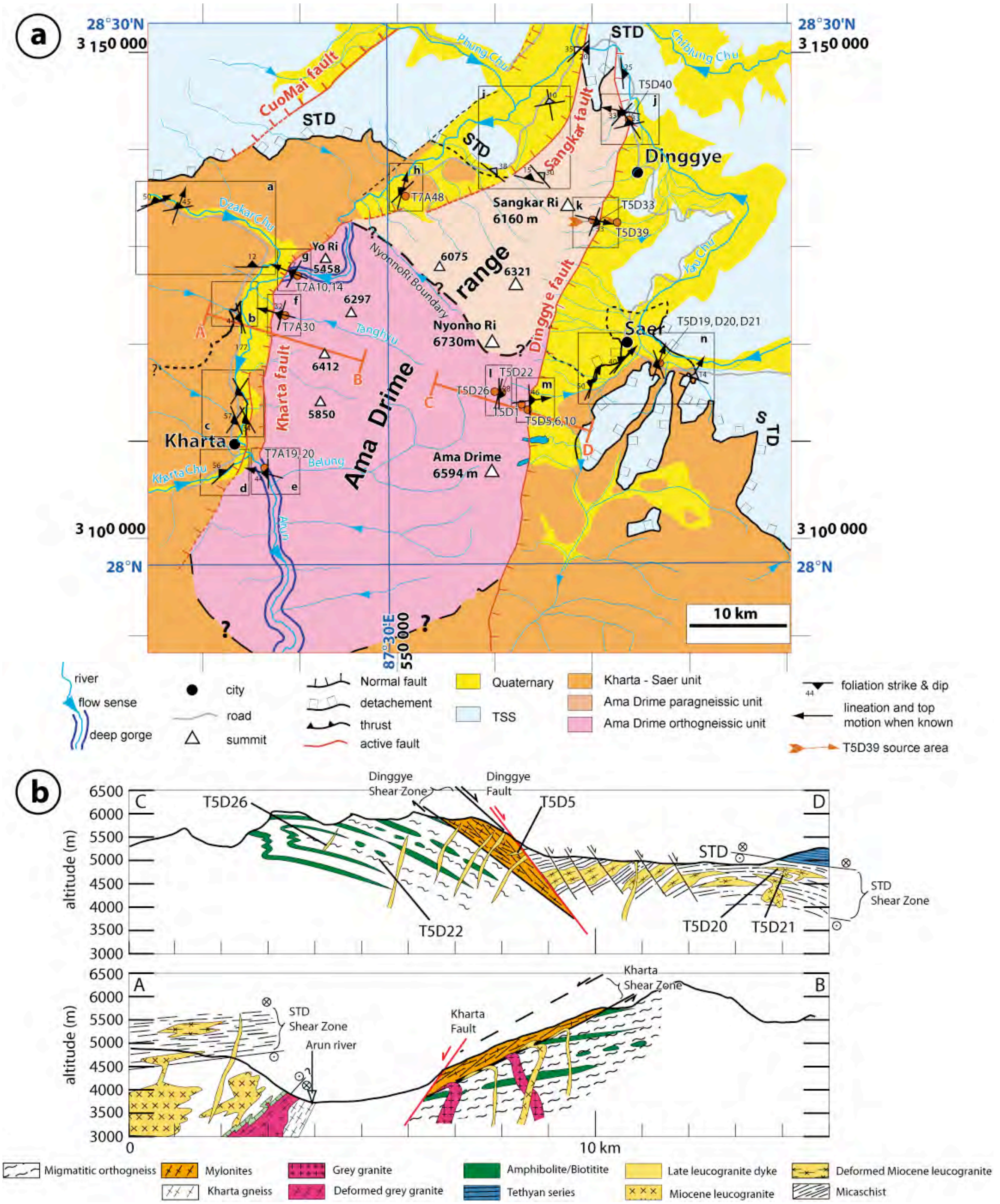

Fig. 2 : Structure of the Ama Drime Range.

a) Structural map of the Dinggye – Kharta area corresponding to the frame on Fig. 1b. Drawn from satellite image interpretation and fieldwork. Projection is UTM45. The Kartha-Saer unit is attributed to the Upper Himalayan crystalline series while the AmaDrime Orthogneisses are attributed to the Lower Himalayan crystalline series (see text). Structural observations are reported as well as samples discussed in this study. For other sample locations see Fig. DR7. Each lettered black box corresponds to a stereonet (Fig. 4). Sections A-B and C-D (Fig. 2b) are located. **b**) Geological schematic cross sections of both flanks of the Ama Drime range. Cross-sections located on Fig. 2a. Drawn from field observations (see text and Fig. 3). No vertical exaggeration.

At the northern end of the range, the Sangkar fault exhibits clear evidences for recent activity with triangular facets and fault scarps (Fig 3-1d). It is probable that the Sangkar and Kharta active faults are linked by an ~E-W active fault (Armijo et al., 1986). At the northern end of the Kharta fault, the Arun – Phung Chu river has a very peculiar course: it enters within the footwall of the active fault, where it carves deep gorges and turns around the Yo Ri promontory before exiting in the Kharta basin (Fig. 2a). This fact was already noticed by Wager (1937) who interpreted the river to be antecedent to the building of the high relief of the Ama Drime, while Armijo et al. (1986) interpreted that pattern as resulting from the capture of the Phung Chu by the Arun River.

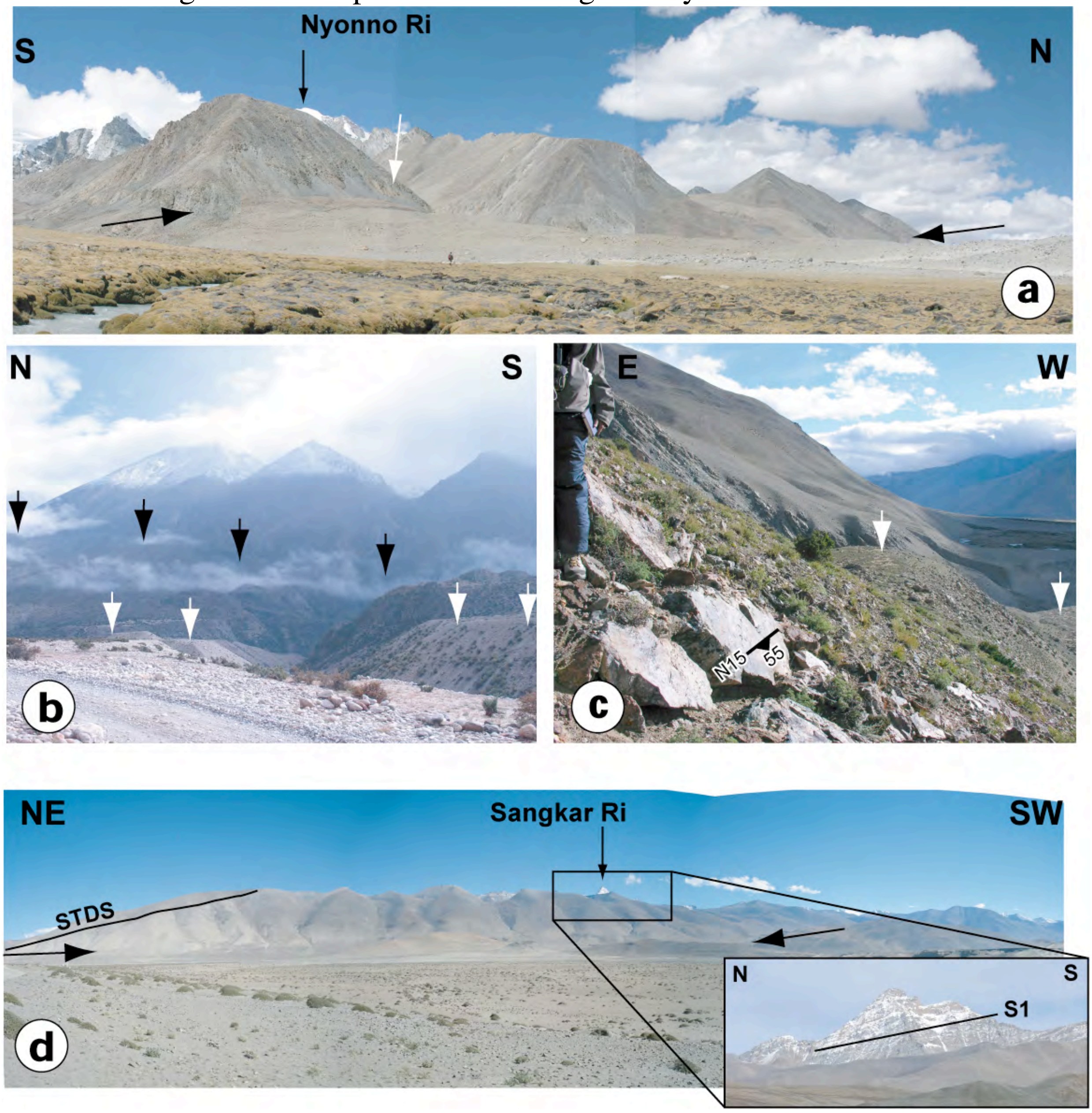

Fig. 3a: Field pictures of the Ama Drime range: active faults bounding the Ama Drime Range
a) Triangular facets along the Dinggye active normal fault. View towards West. The closest facet is ~500 m high. The two converging black arrows indicate the fault trace. White arrow points to quartz cataclasites whose fault surface strikes N06 49E. Nyonno Ri summit (6730 m) in the background. **b)** Triangular facets along the Kharta active normal fault. View towards East. In the background, black arrows indicate the trace of the east branch of the Kharta active fault. Facets are ~1300 m high above the arrows. In the foreground, white arrows indicate the trace of the west branch of the Kharta fault offsetting alluvial terraces of the Kharta Chu. **c)** Along strike view of the north Kharta active normal fault. View towards the SSW from north of the outlet of the upper Arun gorges. White arrows point to a 100 m-high offset of an alluvial terrace. Outcrop in the foreground is a fault surface striking N15 55W at the top of quartz cataclasites. **d)** Sangkar active normal fault. View towards the SE. Trace of the STD on the northern Ama Drime crest is drawn. The two converging black arrows indicate the fault trace. The Sangkar Ri summit (6160 m) sticks out in the background. An enlargement of this summit from a different point of view

shows HC series gently dipping to the north.

Whilst the Eastern and Western crest of the Ama Drime have almost the same altitude, the water divide is located along the eastern one (Fig. 2a), highlighting a profound asymmetry in recent tectonics / erosion that may be in part induced by the Arun river down cutting.

The Ama Drime area shows a relatively high microseismic level documented both by the seismic network of Nepal (Pandey et al., 1995; Cattin & Avouac, 2000) and by temporary seismic networks in Nepal and southern Tibet (Monsalve et al., 2006). In the South of the Ama Drime area, all instrumental $M \geq 5$ and part of the $2 \leq M \leq 4$ earthquakes occur at depths ≥ 50 km, and are thought to take place in the lower Indian crust and upper mantle as a result of continuous subduction and eclogitization (Monsalve et al. 2006; Schulte-Pekum et al., 2005; Baur, 2007). In the north, earthquakes are much shallower (depth ≤ 25 km) and have focal mechanisms compatible with North-South trending normal faulting. This seismic activity occurs on active normal faults that connect the Ama Drime horst to the Xainza rift located north of the Yarlung-Tsanpo suture zone (Pandey et al., 1999; Monsalve et al., 2006).

The Ama Drime range is thus an active horst bounded by two conjugate active normal fault systems, at the southern end of the Xainza-Dinggye fault system (e.g., Armijo et al., 1986).

3.2 Rock lithology, structures and microstructures.

Three main lithologic units can be distinguished in the study area. (1) The Kharta-Saer unit, mostly composed of metasedimentary rocks and rare amphibolites intruded by numerous leucogranites. This unit includes the STD shear zone and the Kharta gneiss. (2) The Ama Drime Orthogneissic unit, which mainly consists in granitic gneisses and migmatites embedding numerous metabasic layers and pods. (3) The Ama Drime Paragneissic unit localized above the Ama Drime Orthogneissic unit, which is mostly represented by paragneisses and pelitic schists. Leucogranite dykes crosscut all units (Fig. 2a, b).

3.2.1 The South Tibetan detachment (STD) and Shear Zone (STDsz).

Near the Ama Drime range, the STD has been described across the Dzakar river (Burg et al., 1984; Cottle et al., 2007), and south of Dinggye (Burchfiel et al., 1992; Leloup et al., 2009; Leloup et al., submitted). The STD separates deformed garnet-micaschists and leucogranites of the UHCS characterized in the STD shear zone (STDsz) by ~E-W foliations gently dipping to the north, NE trending lineation and normal (top to the north) sense of shear, from weakly metamorphosed Tethyan sedimentary series above. In the STDsz, few undeformed leucogranites postdating deformation have also been observed (Leloup et al., 2009; Leloup et al., submitted). As the foliation dips gently, there is no access to a complete section of the STDsz near Saer and its total thickness cannot be assessed. However, along other sections, as near Rongbuk or at the top of the Kula Kangri leucogranite, the STDsz is typically 200 to 300 m thick (Murphy and Harrisson, 1999; Edwards et al., 1996). 100 m below the STD, garnet-micaschists of the STDsz are characterized by the transition from a staurolite-garnet paragenesis (prekynematic?) to sillimanite-garnet (synkinematic) assemblage (Leloup et al., 2009; Leloup et al., submitted). The corresponding PT evolution constrained by pseudosections and garnet isopleths, is characterized by a peak pressure of ~0.6 GPa (~22km) and 550°C followed by a slight heating and decompression until ~0.45 GPa (~27km) and ~625°C, preceding a phase of decompression and cooling (Fig. 5c) (Leloup et al., 2009; Leloup et al., submitted).

Combining published observations, fieldwork, and Landsat satellite image interpretation, Leloup et al. (submitted) propose a map of the STD (Fig. 2a). This mapping confirms that the STD dipping ~10±5° to the NNE, is deflected to the north around the Ama Drime range, and is cut and offset by the N-S active normal faults. The apparent horizontal offsets of the STD are of 35±5 km along the Dinggye active normal fault, and of ~15 km across the Sangkar fault (Fig. 2a), which correspond to vertical offsets of 4.4 to 9.4 and 1.3 to 4 km, respectively (Leloup et al., 2009; Leloup et al., submitted).

At the scale of the orogen the STD is broadly located at the transition between the Tibetan plateau and the high Himalayan chain. However, it has no clear morphological expression, it is crosscut by active N-S normal faults and no crustal earthquake indicative of ~E-W normal faulting has been reported. The STD is thus a fossil structure.

3.2.2 The Kharta area.

Along the Dzakar-Phung Chu valley, ~12 km south of the STD (~8 km below), foliations dip to the west (Fig. 2a, Fig. 4b,c,d). In this area the main lithologies are garnet bearing metapelites, often migmatitic, associated with minor orthogneiss, metabasite and calc-silicate rocks. These lithologies are named the Kartha gneiss and attributed to the GHCS (our UHCS) by Borghi et al. (2003) that document an adiabatic decompression from ~0.8 GPa and ~700°C, prior to a roughly isobaric cooling at ~0.2 GPa (Fig. 5a). Several generations of leucosomes are conspicuous, ranging from concordant leucogranitic Gt-Sill orthogneiss to discordant cordierite bearing leucogranite veins and pods (Borghi et al., 2003). All these rocks are crosscut by Miocene tourmaline leucogranitic dykes (Visonà and Lombardo, 2002). North of Kharta a large granite body that crosscuts the gneiss is overlaid by a west dipping shear zone with N-S lineations (Fig. 4b). The Kharta gneiss exhibits either no lineation or N-S to NE-SW trending lineations (Fig. 2a, Fig. 4c,d). In the absence of clear shear criteria it is difficult to relate this deformation to a precise tectonic episode.

3.2.3 The Ama Drime range.

Except at the very northern tip of the range, above the STD, all rocks comprised between the Kharta – Sangkar and Dinggye active faults are crystalline rocks belonging to the HCS. Along the Belung and Tanghyu valleys most rocks are migmatitic orthogneiss containing large layers and boudins of metabasites that have recorded eclogite facies metamorphism, and that have been attributed to the LHCS (our LoHCS) because of similar rock types (Groppo et al., 2007). Inherited U-Pb zircon and monazite ages from these orthogneisses provide similar 1.7-1.8 Ga age than in the Uleri orthogneisses of the LoHCS (Robinson et al., 2001; Liu et al., 2007; Cottle et al., 2009) confirming the possible correlation. Similar rocks outcrop in the core of the range and south of the Nyonno Ri on the eastern side of the Ama Drime (Fig. 2a, Fig. 3b). These lithologies constitute the Ama Drime Orthogneissic unit (ADO).

Deformed rocks outcropping east of Kharta in the footwall of the Kharta fault have been interpreted by Groppo et al. (2007) as corresponding to the main thrust between the LHCS (LoHCS) and the GHCS (UHCS) (MCTu). In that area, rocks indeed show a strong deformation, with foliations dipping N179 44W on average and lineations striking ESE-WNW to NW-SE (Fig. 2a; Fig 4e). However, analysis of the deformation in rocks that show a clear down dip lineation, reveals top to the west shear senses and thus a normal ductile shear zone. That ductile shear zone is in the direct prolongation of the eastern branch of the Kharta active fault (Fig. 2a). The relative dispersion of the lineations (Fig. 4e) suggests that a previous deformation lineation has been affected by the ductile normal fault. Ductile mylonites with ~N-S foliation and top to the West motion (Fig. 3cl) are observed everywhere in the footwall of the Kharta fault and constitute the Kharta shear zone (Fig. 2a). The mylonites trend N15 32W with lineations striking N284 on average in Tanghyu valley (Fig. 4f). In the upper Arun gorges the foliations strike N29 27W and the lineations N290 (Fig. 2a, Fig. 4g).

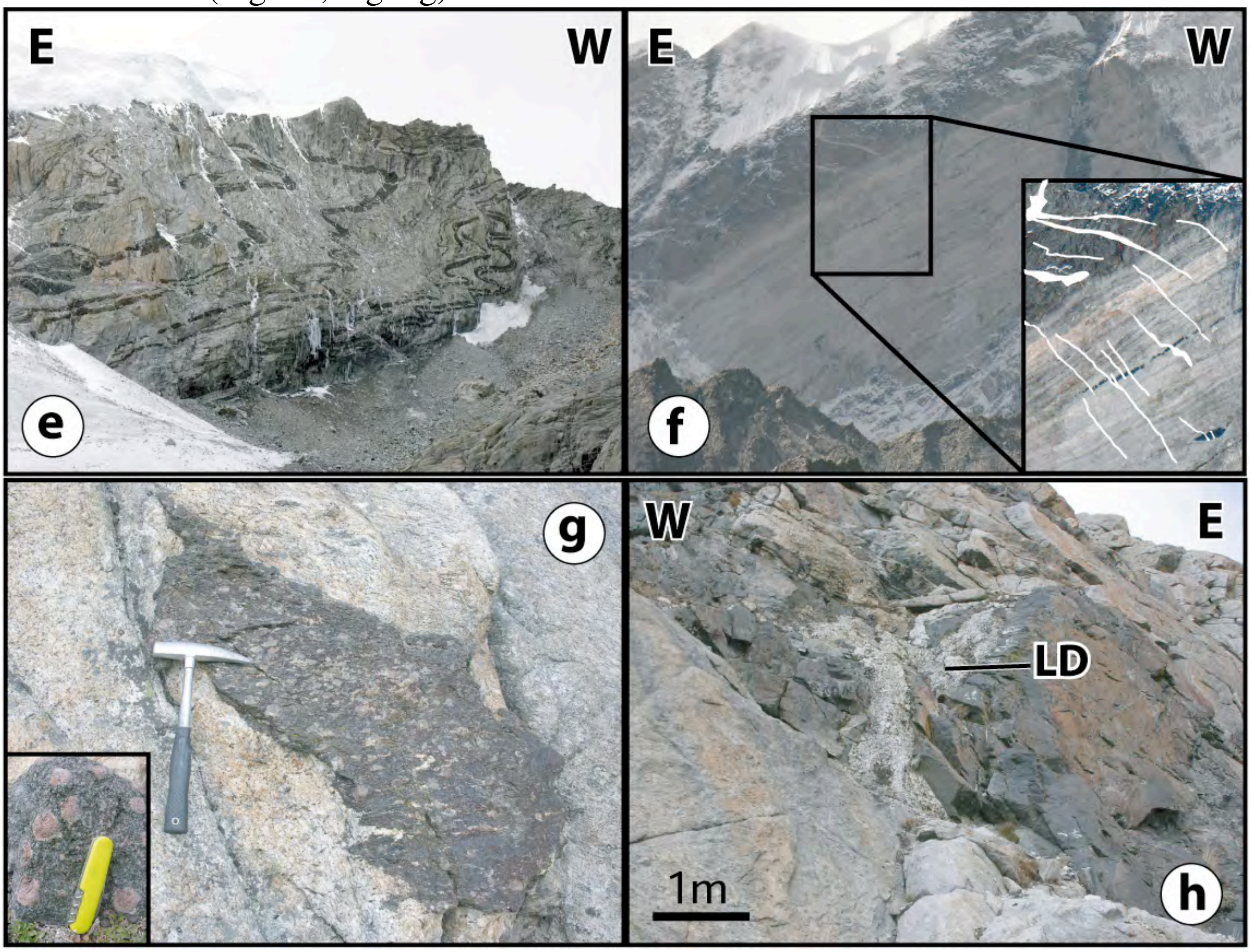

Fig. 3b: Field pictures of the Ama Drime range: orthogneisss of the Ama Drime south of the Nyonno Ri.
e) Folded basic layers within migmatites south of the Nyonno Ri. The cliff is ~400 m high. The fold axes trend ~N-S. **f)** Cliff north of the Ama Drime summit showing leucocratic dykes cutting across previous foliation including boudinaged basic layers (inset with dykes highlighted in white). The visible part of the cliff is ~500 m high. View towards the South **g)** Basic enclave within migmatite. Hammer for scale. Note cm-scale garnets in basic level (inset). Migmatitic sample T5D22 comes from this outcrop. **h)** Basic layer within migmatites cross-cut by a leucocratic pegmatitic dyke (LD, sample T5D26). **e, g, h** from glacial valley south of the Nyonno Ri (zone 1, Fig. 2a).

Similarly, East-dipping mylonites have been described on the eastern side of the range in the footwall of the Dinggye fault defining the Dinggye shear zone (Fig. 2b, Fig. 3ci,j,k) (Zhang and Guo, 2007). The mylonites trend N178 46E SE of the Nyonno Ri and N21 33E east of the Sangkar Ri, with lineations trending N82 and N103, respectively (Fig. 2a, Fig. 4k, m).

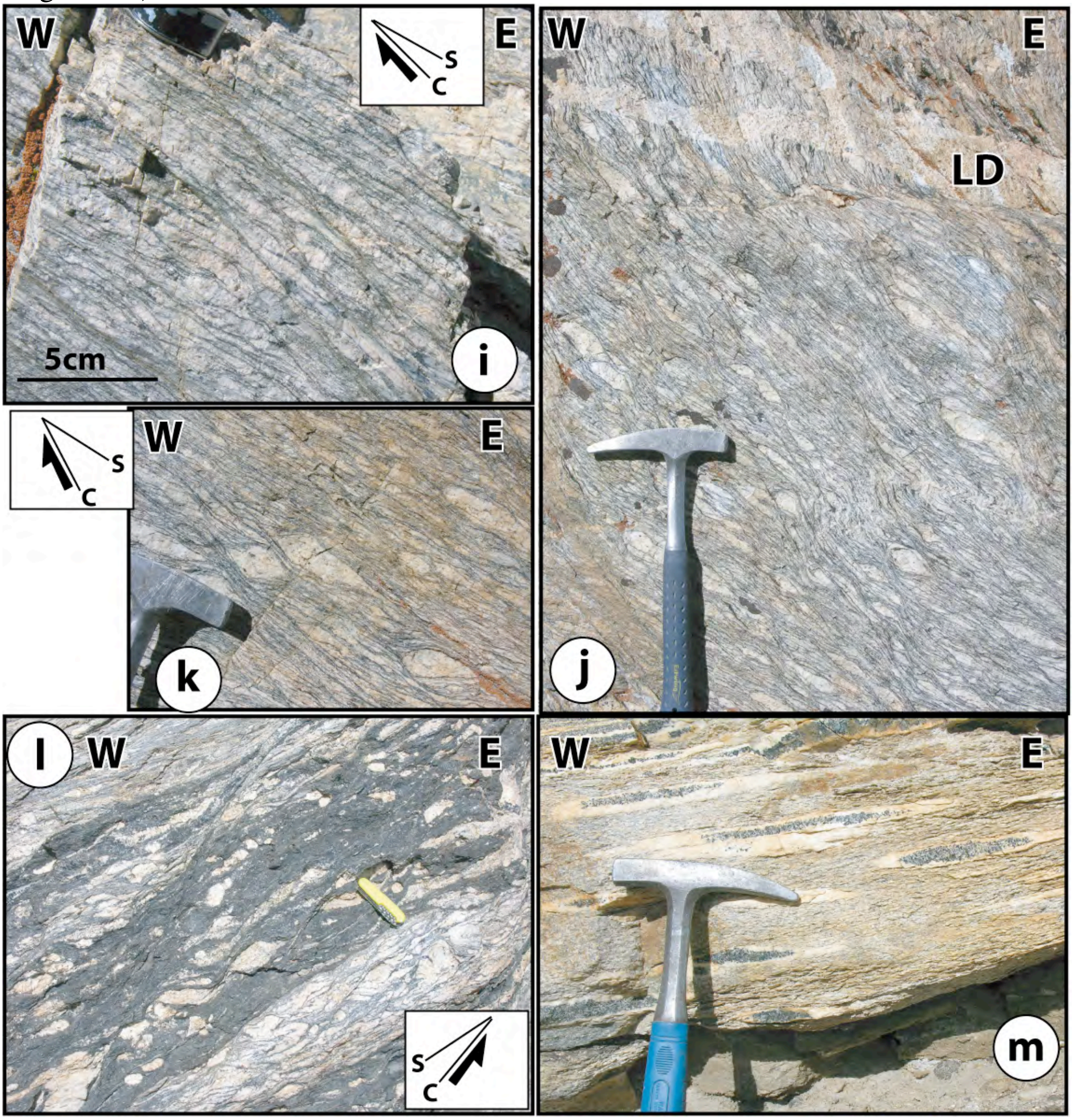

Fig. 3c: Field pictures of the Ama Drime range: normal shear zones on both side of the Ama Drime range.
i) Chlorite-grade C/S deformation in orthogneiss showing top to the east normal motion. Footwall of Dinggye normal fault. Glacial valley south of the Nyonno Ri summit (zone m, Fig. 2a). See Fig. 4m for foliation and lineation attitude. **j)** Late leucocratic dyke (LD, sample T5D5) crosscutting mylonitic orthogneiss (sample T5D6). Footwall of Dinggye normal fault. Hammer gives scale. Glacial valley south of the Nyonno Ri summit (zone m, Fig. 2a). **k)** Close up of Fig. 3cj mylonitic orthogneiss, showing top to the east (normal) shear sense. Hammer gives scale. See Fig. 4m for foliation and lineation attitude. **l)** Mylonitic orthogneiss and biotite-rich enclave. Knife gives scale. Footwall of Kharta normal fault in Arun – Phung Chu gorges (zone g, Fig. 2a). Shear planes indicate top to the west (normal) shear sense. See Fig. 4g for foliation and lineation attitude. **m)** Stretched remnants of tourmaline bearing leucocratic dykes. Hammer gives scale. Footwall of Kharta normal fault in Arun – Phung Chu gorges (zone g, Fig. 2a).

On both sides of the Ama Drime, normal deformation is observed to occur at various temperatures from ductile mylonites to cataclasites with the temperature of deformation decreasing towards the active fault. This pattern is classically interpreted as the progressive uplift of the deep part of the fault in its footwall (e.g., Leloup et al., 1993). All leucocratic dykes appear to be affected by the normal ductile deformation along the western flank (Fig. 2b, Fig. 3cm) while several dykes crosscut the mylonitic foliation along the eastern flank (Fig. 2b, Fig. 3cj). This could indicate that the western shear zone was active until more recent times than its eastern counterpart.

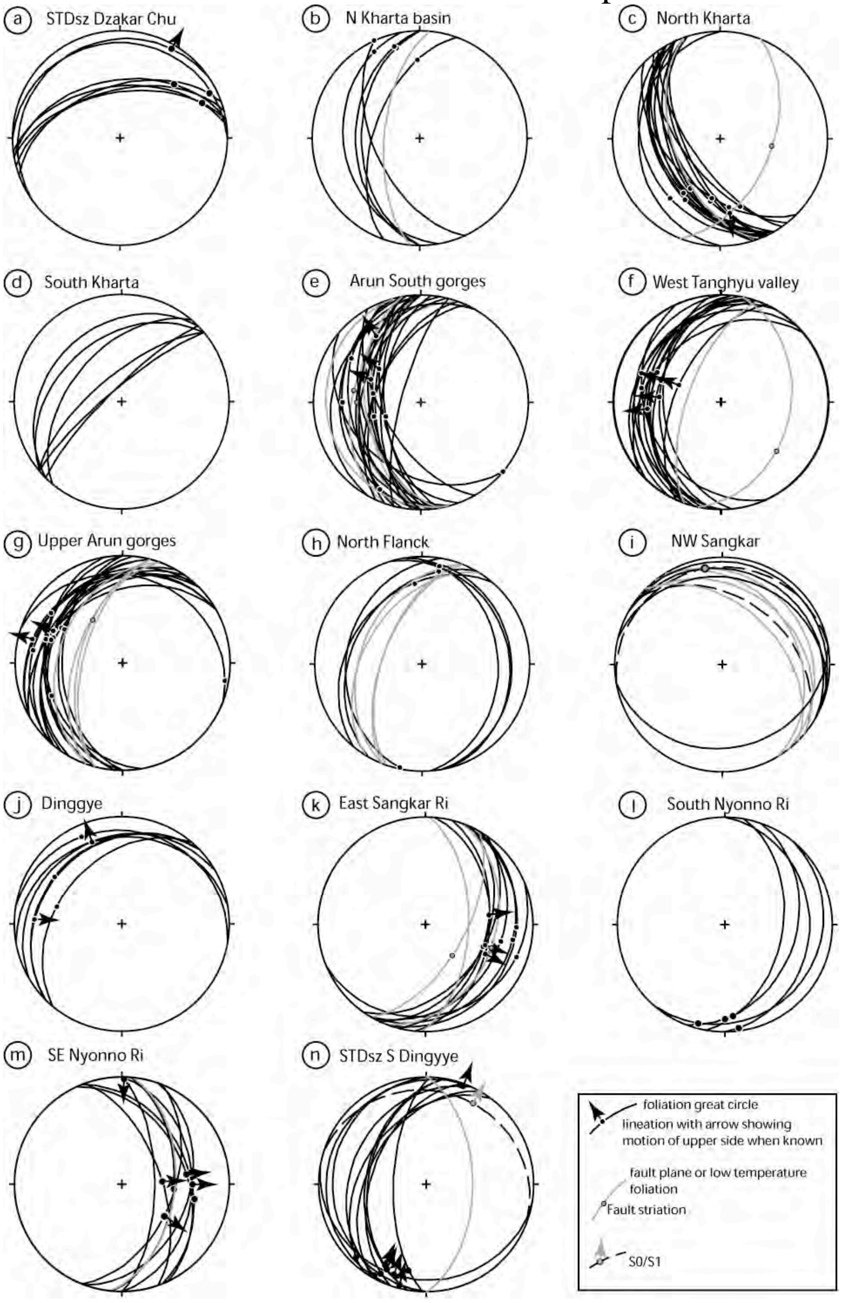

Fig. 4: Structure geometry in the Ama Drime area.

Lower-hemisphere, equal-area stereonet diagrams. Corresponding areas are located on Fig. 2a. All data are listed in Table DR1. Foliations and lineations, and brittle faults (in grey) are plotted.

a) South Tibetan shear zone of the Dzakar Chu valley. **b)** Arun valley below the STDsz (Kharta-Saer unit). **c)** Kharta gneiss immediately north of Kharta. **d)** Kharta gneiss SE of Kharta. **e)** Arun gorges south of Kharta (Kharta sz) (here grey corresponds to low-grade deformations). **f)** Western part of the Tanghyu valley (Ama Drime orthogneisses- Kharta sz). **g)** SW part of the upper Arun-Phung Chu gorge (Ama Drime orthogneisses - Kharta sz). **h)** Kharta-Saer unit north of the Ama Drime. **i)** Foliations in the Ama Drime paragneisses and schistosity (dashed) in the Tethyan Sedimentary Sequence (TSS) NW of the Sangkar Ri. **j)** North of Dinggye (Ama Drime paragneisses). **k)** SE of the Sangkar Ri (Ama Drime paragneisses, Dinggye sz). **l)** South of the Nyonno Ri (Ama Drime orthogneisses). **m)** SE of the Nyonno Ri (Ama Drime orthogneisses, Dinggye sz). **n)** STDsz East of Saer and S0/S1 and lineation in TSS.

In the northern part of the Ama Drime range, north of the Nyonno Ri, lithology change to paragneisses and pelitic schists crosscut by leucogranites here defined as the Ama Drime Paragneissic unit (ADP). The top of this lithologic unit, just bellow the STD is mostly composed of highly sheared pelitic schists and leucogranites similar to those found in the Kharta-Saer unit within the STD sz. Such rocks are visible dipping to the north below the Sangkar Ri summit (Fig 3-1d). Paragneiss also outcrop farther south on the eastern Flank of the range where they are affected by the Dynggye shear zone (zone k, Fig. 2a). Given their structural position, above the ADO attributed to the LoHCS and just below the STD shear zone within the UHCS, such gneisses could be the equivalent of the Kharta gneiss. However, the lack of observation and detailed fieldwork between the Sangkar Ri and the Nyonno Ri leave open other interpretations, as for example a correlation with the LoHCS paragneisses overlying the Uleri Gneiss (Goscombe et al., 2006). We propose a possible map for the boundary between the Ama Drime Paragneissic and Orthogneissic units (Fig. 2a), although precise mapping and characterization would require further fieldwork. We named this boundary the Nyonno Ri boundary.

There are no precise descriptions of the deformation of the orthogneiss in the core of the Ama Drime. Away from the bounding normal faults however the metabasic rocks, when they have not been disrupted in the surrounding migmatites (Fig. 3bg), define kilometre-long layers that are affected by folds with ~horizontal axial planes and ~N-S trending axis (Fig. 3be). South of the Nyonno Ri, deformation at the contact between a ~3 m thick metabasic layer (Fig. 3bh) and the migmatites is characterized by foliation gently dipping to the east and N-S lineations (Fig. 4l).

North of the Ama Drime range, quartzites very similar to those outcropping on the active normal fault scarps further south outcrop ~1 km north of the Kharta-Sangkar fault (Fig. 2a). Foliation in the quartzites trends N24 38W (Fig. 4h) parallel to normal faults that affect and tilt the surrounding micaschists and gneiss. When back-tilted the gneiss show a ~N15 striking lineation parallel to STD shear zone lineations in the area (Fig. 4h).

Some authors (e.g., Borghi et al., 2003; Liu et al., 2007) have proposed that the Ama Drime is the northern continuation of the Arun anticline described by Bordet (1961). The Ama Drime is bounded on both sides not only by active normal faults, but also by ductile ones. In that context it appears more as a horst than a fold. Because low angle ductile normal faults outcrop in the footwall of the steeper active normal faults it is very tempting to interpret these structures as resulting from a single continuous metamorphic core complex – type of deformation (e.g. Zhang and Guo, 2007; Jessup et al., 2008; Cottle et al., 2009).

4 P-T-t-D path of the crystalline rocks of the AmaDrime

4.1 P-T paths.

The petrologic and thermobarometric studies of Lombardo & Rolfo (2000), Liu et al., (2005), Groppo et al. (2007) and Liu et al., (2007) have established that the Ama Drime Orthogneissic unit contains the only eclogite found so far in the central Himalayas. These rocks have recorded pressure of at least 1.4 GPa (~ 52 km depth) and have been granulitized at high temperature (~800°C) during their exhumation (Fig. 5b).

In the following paragraph we present the first petrologic data of the Ama Drime Paragneissic unit within the Ama Drime range. Until now such data were restricted to Kharta-Saer unit in the hanging wall of the Kharta fault (Borghi et al., 2003) (Fig. 5a) or the Dingyye fault (Leloup et al., 2009; Leloup et al., submitted) (Fig. 5c). This study is based on the combination of thin section analyses, measurement of mineral chemical composition (punctual and mapping) on a SX100 Cameca CAMEBAX Microprobe at the University of Montpellier operating at 15kV and 15nA with a counting time of 10s per element, and pseudosection and isopleth calculation using Perple_X software (Connolly [1990]) (detailed procedure available in appendix I) at fixed bulk-rock composition (see appendix I).

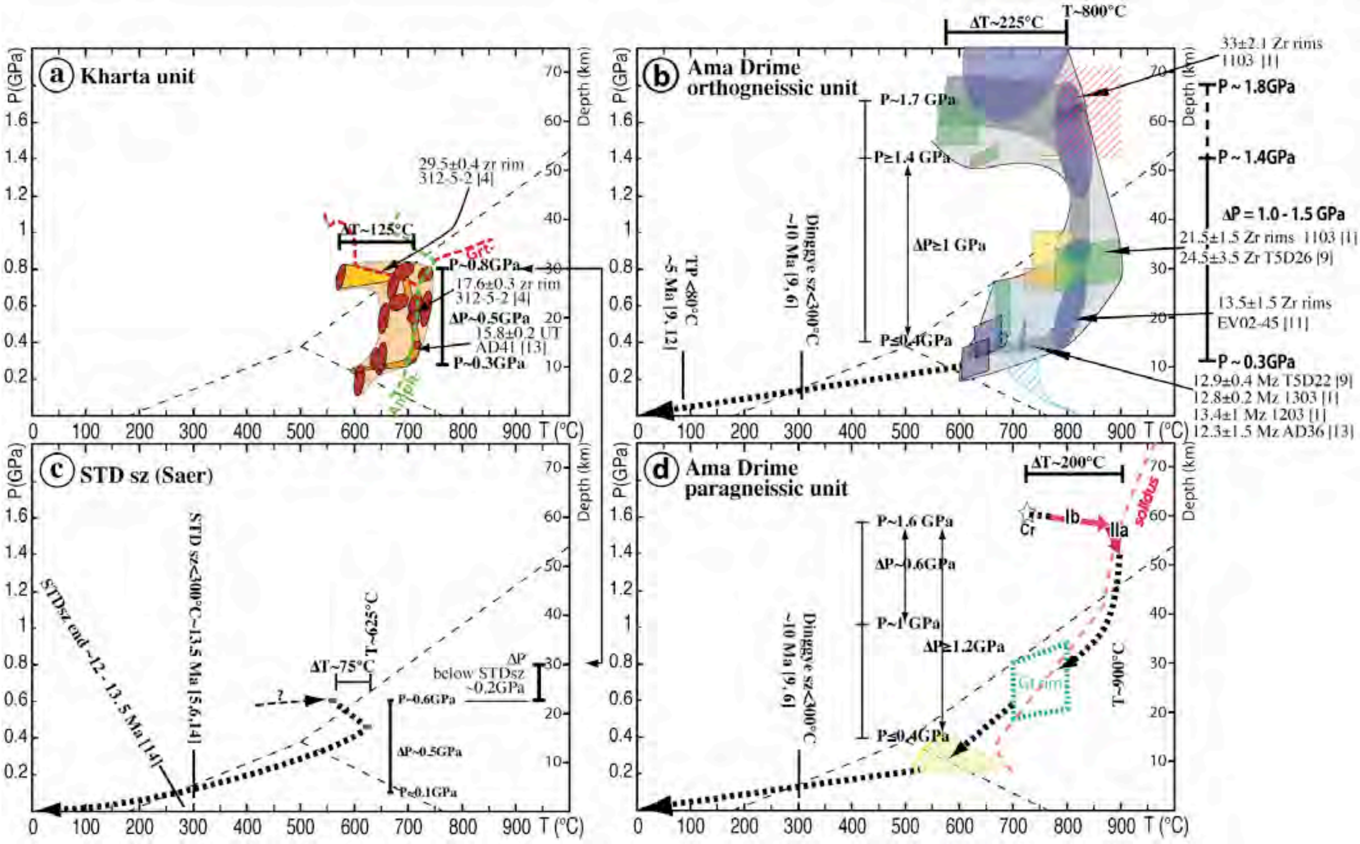

Fig. 5 : P-T paths and corresponding timing constraints.

Aluminosilicates fields are plotted for reference. Samples are located on Fig. 2b and Fig. DR7. Numbers without units are ages in Ma. See text for details.

a) Kharta gneiss (Kharta-Saer unit west of the Kharta fault). P-T constraints from Borghi et al. (2003) [3] for samples Ev 8, 13, 16, 21, 45, 70, 80 and TB25. Ellipses correspond to individual sample / paragenesis P-T determinations. The narrow dark path corresponds to P-T conditions constrained from isoplets. The lighter path connects the largest documented pressure (M2, sample Ev45) with the earliest paragenesis (M1, sample Ev45). The stability fields of amphibole and garnet are drawn for metabasite chemistry (Groppo, 2007) in order to discuss the ages of zircons overgrowths within sample 312-5-2. Age constraints from Li et al., 2003 (sample 312-5-2) [4] and Cottle et al (2009) [13] (sample AD41). **b)** Ama Drime Orthogneisses. P-T data from Liu et al., (2005) [7] (green, samples T01-386 and T01-389); Liu et al., (2007) [1] (yellow, samples 1103 and 1303); Groppo et al., (2007) [8] (blue, samples Ev02-42&45, 97-60), and Cottle et al. (2009) [13] (orange, sample AD43). All samples are amphibolite boudins unless the ones dark framed that correspond to embedding gneiss. Range of initial vapor-absent melting by mica breakdown between 1.4 and 1.8 GPa (red hatching) compiled from Vielzeuf & Holloway (1988); Vielzeuf & Clements (1992); Vielzeuf & Montel (1994); Patiño Douce & Beard (1996); Castro et al. (2000); Harris et al. (2004); Auzanneau et al. (2006) and Indares et al. (2008). Range of monazite crystallization below 0.7 GPa (blue hatching) from Kelsey et al. (2008). Timing constraints from Liu et al. (2007) [1] (samples 1103 and 1303), Rolfo et al. (2005) [11] (Ev02-45), Cottle et al (2009) [13] and this study [9] (sample T5D22). **c)** STD shear zone near Saer. P-T constraints from Leloup et al. (submitted) [14]. The ~300°C timing constraint comes from micas argon dating (Leloup et al., 2009; Leloup et al., submitted [14]; Hodges et al., 1994 [5]; Zhang and Guo, 2007 [6]). **d)** Ama Drime Paragneisses. P-T constraints from this study [9] (T5D33 & 39b, see Fig. 6). The ~300°C timing constraint comes from micas argon dating (This study [9]; Zhang and Guo, 2007 [6]).

4.1.1 P-T path of the Ama Drime Paragneissic unit in the footwall of the Dinggye active fault.

West of Dinggye, in the footwall of the Dinggye active fault, paragneiss and intruding leucogranites are both affected by top to the East (N103) normal ductile shear (k, Fig. 2a and Fig. 4). Sample T5D33 from such paragneisses was collected at an elevation of 5125 m east of the Sangkar Ri, while T5D39b is a boulder collected from the down-stream river fan (Table 1, Fig. 2a). Despite not having sampled in situ, T5D39b was selected because it comes unambiguously from the Sangkar Ri eastern flank and is much fresher than T5D33.

The paragneiss contains biotite, sillimanite, garnet (with biotite, plagioclase, quartz, oxyde and muscovite inclusions), quartz, plagioclase, muscovite, and accessory zircon, apatite and oxides. This paragneiss is locally migmatitic and contains K-feldspar within millimeter-scale unconnected pods. The foliation is defined by biotite, and rare late muscovite while the lineation is outlined by sillimanite. Sample T5D33 is strongly retrogressed and garnet is mostly replaced by chlorite. T5D39b does not show any evidence of such late retrogression and few kyanite relicts have been preserved in the foliation.

Syn-kinematic biotite, sillimanite and muscovite as well as pre- to syn-kinematic garnets indicate top to the East high temperature ductile normal shearing (Fig. 6a).

Four successives paragenesis are recognized in the paragneiss: (P1) Biotite + plagioclase + quartz + muscovite as inclusions in large garnets + garnet core; (P2) Kyanite or sillimanite + biotite + plagioclase + quartz (including myrmekites) + garnet rim (inclusion poor zone) + K-feldspar + melt with kyanite predating sillimanite. Note that locally Kyanite is included in the garnet rim. This paragenesis is found in the main foliation and in the shear planes (Fig. 6a). This implies that a top to the east normal ductile shearing occurred under granulite facies conditions, contemporaneously with partial melting; (P3) Biotite + plagioclase + quartz; (P4) The medium to low temperature evolution is characterized by replacement of aluminosilicates by muscovite, growth of andalusite replacing kyanite and destabilization of garnet replaced by chlorite, muscovite and chlorobiotite. Continuation of top to the east normal motion during medium temperature evolution is evidenced by the truncation of sillimanite with fractures filled by muscovite and the rare occurrence of syn-kinematic muscovite in the foliation (Fig. 6a). The low temperature evolution is associated with the garnet fracturation and chloritization.

Biotites (P1 & P3) show high X_{Fe} [(Fe/(Fe+Mg)] of 0.57 to 0.62 in both samples (Table DR2-1). In sample T5D39b, the Si(IV) amount in muscovite is significantly higher in garnet inclusions (6.4-6.6 a.p.f.u. on the basis of 22 oxygens) than in the matrix (6.1-6.3 a.p.f.u.) (Table DR2-2). This suggests that the muscovite in inclusions (P1) crystallized at higher pressure than muscovite in the matrix (P4) (Powell & Evans, 1983).

X-ray map and microprobe traverse of T5D39b garnet show complex zoning, with a high calcium and inclusion-rich core (garnet I, P1) and a late, low calcium, inclusion-poor rim (garnet II, P2) (Table DR2-3, Figs. 6b & c).

In more details garnet I (P1) can be separated into two zones. The innermost zone (Ia, Fig. 6c) is rich in muscovite and plagioclase inclusions, and does not present clear composition zoning (Alm 0.662 - 0.685, Pyr 0.180 - 0.192, Gros 0.104 - 0.124, Spes 0.031-0.034) (Table DR2-3, Fig. 6c). Detailed analysis of zone Ia X-ray map shows that Grossular and Pyrope contents decrease and Almandine content increase concentrically around the inclusions (Fig. 6b). Such pattern suggests that chemical diffusion occurred around the inclusions after their incorporation, modifying garnet composition. Garnet initial chemistry is only preserved away from the inclusions, and is not present along the Fig. 6c transect. It is characterized by relatively high Grossular content (0.124), low Almandine and Pyrope contents (0.662 and 0.180, respectively) and intermediate Spessartine content (0.032) (Table DR2-3). Zone Ib is characterized by Pyrope and Almandine increase from 0.66 and 0.18 to 0.70 and 0.20, respectively, by Grossular content decrease from 0.13 to 0.08 (Table DR2-3, Fig. 2c) and almost constant Spessartine content (~0.03).

Within garnet rims (zone II, P2), which contain few biotite, quartz, Kyanite and plagioclase inclusions, two zones can be distinguished (Fig. 6c). Zone IIa shows continuous Grossular decrease from 0.08 to 0.05 and Almandine increase from 0.70 to 0.73 but constant Pyrope and Spessartine (~0.19 and ~0.03 respectivelly) (Table DR2-3, Fig. 6c). In zone IIb Grossular is constant (0.05) as almandine and spessartine slightly increase (0.73 to 0.75 and 0.04 to 0.03 respectivelly) and Pyrope decrease from 0.19 to 0.17. Outermost rim is characterized by high Almandine (up to 0.79) and spessartine (>0.05) and relatively low Grossular and Pyrope content (0.03 and 0.13 respectively) (Table DR2-3, Fig. 6c).

In sample T5D33 no garnet with muscovite and plagioclase inclusion (P1, garnet zone I) were observed. Only small porphyroclasts are still visible with zone II compositions (P2).

In sample T5D39b, plagioclases have higher Ca content when included within or in contact with garnet (An 0.25-0.46) than in the matrix (An 0.29-0.24) (Table DR2-4). In sample T5D33 the Ca content of the matrix plagioclase are even higher (An 0.40-0.43) probably because T5D33 is highly retrogressed as evidenced by the replacement of garnet by chlorite. K- Feldspar (P2) are similar in both samples (Or 0.88-0.89).

T5D39b P-T path was obtained using pseudosections, calculations of garnet isopleths and classical thermobarometry (Fig. 6d). Despite some evidences for partial melting, constant chemistry is assumed as melts are only restricted to small unconnected pods at the microscopic scale, and because there are no evidences for local melt escape nor intrusion on macroscopic samples or outcrops.

The garnet chemical zoning presented above yields to the interpretation that high temperatures following paragenesis 1 have induced chemical re-equilibration of plagioclase and biotite inclusions with the surrounding garnet in garnet cores. Garnet composition corresponding to initial garnet growth has thus to be found in garnet cores but away from inclusions, while early plagioclase composition would be preserved in the matrix away from garnets. These compositions correspond to high-pressure (~1.6 GPa) and temperature around 775°C (star Cr on Fig. 6d). Garnet compositions and evolution in zone Ib (Pyrope and Almandine increase and Grossular decrease) reflect P-T conditions during the garnet core growth. They correspond to heating up to ~850°C, at almost constant pressure (~1.6 GPa) (Ib arrow on Fig. 6d). Inner part of zone II (IIa, P2) is compatible with late high temperature growth or re-equilibration at ~875°C during decompression from 1.6 GPa to 1.4 GPa (IIc arrow on Fig. 6d). This high temperature event induced the re-equilibration in garnet cores around biotite and plagioclase inclusions. Based on Fig. 6d pseudosection, presence of Kyanite during the P2 implies that T was still at least at 875°C when decompression reached 1.2 GPa (Ky zone on Fig. 6d). The outer part of zone II most likely corresponds with late diffussion at garnet rim. This late re-equilibration was constrained coupling garnet-biotite thermometry and garnet-sillimanite-plagioclase barometry from the GTP compilation (Reche & Martinez, 1996) for mineral in close contact (plagioclase, biotite and garnet rim). Only calibration based on Fe, Mg, Ca, Mn and Ti exchange were used. Results indicate that this late diffusion occurred at 700-800°C and 0.9-0.5 GPa (green dashed box on Fig. 6d).

These latter PT estimates, compared with the ones obtained for garnet zone IIa, imply that an important decompression event took place from ~1.6 GPa to ~0.7 ± 0.2 GPa and during a small decrease of temperature from ~875 to 750 ± 50°C. This episode was associated with partial melting by muscovite breakdown and successive growth of kyanite and sillimanite (P2, Fig. 6d). The late retrograde evolution is only constrained by the presence of andalusite and the absence of cordierite suggesting pressures comprised between 0.4 and 0.2 GPa and temperature lower than 675°C (yellow area on Fig. 6d).

T5D33 provides similar P-T evolution, but starting at 1.3 GPa and 900°C (Fig.6d) based on pseudosection since only P2 garnet have been preserved. Late diffusion at T5D33 garnet rim is constrained to occur at 0.75±0.2 GPa and 725±75°C (Fig.6d) based on garnet-biotite thermometry and garnet-sillimanite-plagioclase barometry. The retrograde evolution yielded to the crystallisation of Ca rich plagioclases in T5D33.

Samples	General location	zone Fig 3	GPS outcrop	UTM coordinates (zone 45R) easting	nording	Altitude (m)	Rock type	Geochronology and petrology	reference
T5D1	SE Nyonno Ri	m	179	562748	3113774	5217	orthogneiss	**U/He** (ap)	this study
T5D5	SE Nyonno Ri	m	178	563487	3113287	5069	late leucocratic dyke	**U/Pb** (mz SHRIMP Bejing)	this study
T5D6	SE Nyonno Ri	m	178	563487	3113287	5069	orthogneiss	**Ar/Ar** (bio)	this study
T5D10	SE Nyonno Ri	m	184	563427	3114679	5237	garnet migmatitic gneiss	**Ar/Ar** (bio)	this study
T5D19b	STDsz S Dinggye	o	222	576656	3117898	4263	garnet-sillimanite micaschist	**Ar/Ar** (bio); **Petrology**	Leloup et al., submitted
T5D20	STDsz S Dinggye	o	222	576656	3117898	4263	deformed leucogranite	**U/Pb** (zr IMS1270 Nancy, mz SHRIMP Bejing); **Ar/Ar** (bio, mu)	Leloup et al., submitted
T5D21	STDsz S Dinggye	o	222	576656	3117898	4263	undeformed leucogranite	**U/Pb** (zr IMS1270 Nancy, mz SHRIMP Bejing); **Ar/Ar** (mu)	Leloup et al., submitted
T5D22	South Nyonno Ri	l	224	560531	3114923	5346	migmatitic orthogneiss	**U/Pb** (mz SHRIMP Bejing); **U/He** (ap)	This study
T5D26	South Nyonno Ri	l	225	559995	3115086	5419	undeformed late pegmatite	**U/Pb** (zr IMS1270 Nancy); **U/He** (ap)	This study
T5D33	East Sangkar Ri	k	230	570192	3132561	5124	garnet-sillimanite paragneiss	**Ar/Ar** (bio) ; **Petrology**	This study
T5D39b	East Sangkar Ri	k	226	572515	3132527	4613	boulder of garnet-sillimanite paragneiss not in place	**Ar/Ar** (bio) ; **Petrology**	This study
T5D40	North Dinggye	j	237	573786	3142785	4266	undeformed granite	**U/He** (ap)	This study
T7A10	Upper Arun gorges	g	7-33	539159	3127192	3938	orthogneiss	**Ar/Ar** (bio)	This study
T7A14	Upper Arun gorges	g	7-37	538926	3127119	3944	deformed microgranite	**Ar/Ar** (bio)	This study
T7A19	Arun South gorges	e	7-61	536095	3107586	3670	mylonite	**Ar/Ar** (bio)	This study
T7A20	Arun South gorges	e	7-62	535994	3107747	3628	cataclastic orthogneiss	**Ar/Ar** (mu)	This study
T7A33	West Tanghyu valley	f	7-66	537600	3123282	4119	gneiss	**Ar/Ar** (mu)	This study
T7A48b	North flanck	h	7-88	550322	3135144	4408	quartz cataclasite with chlorite and muscovite recrystalisation	**Ar/Ar** (bio, mu)	This study

Table 1 : sample locations and facies.
All samples used in this study are listed. For map location see Fig. 2 and Fig. DR7.

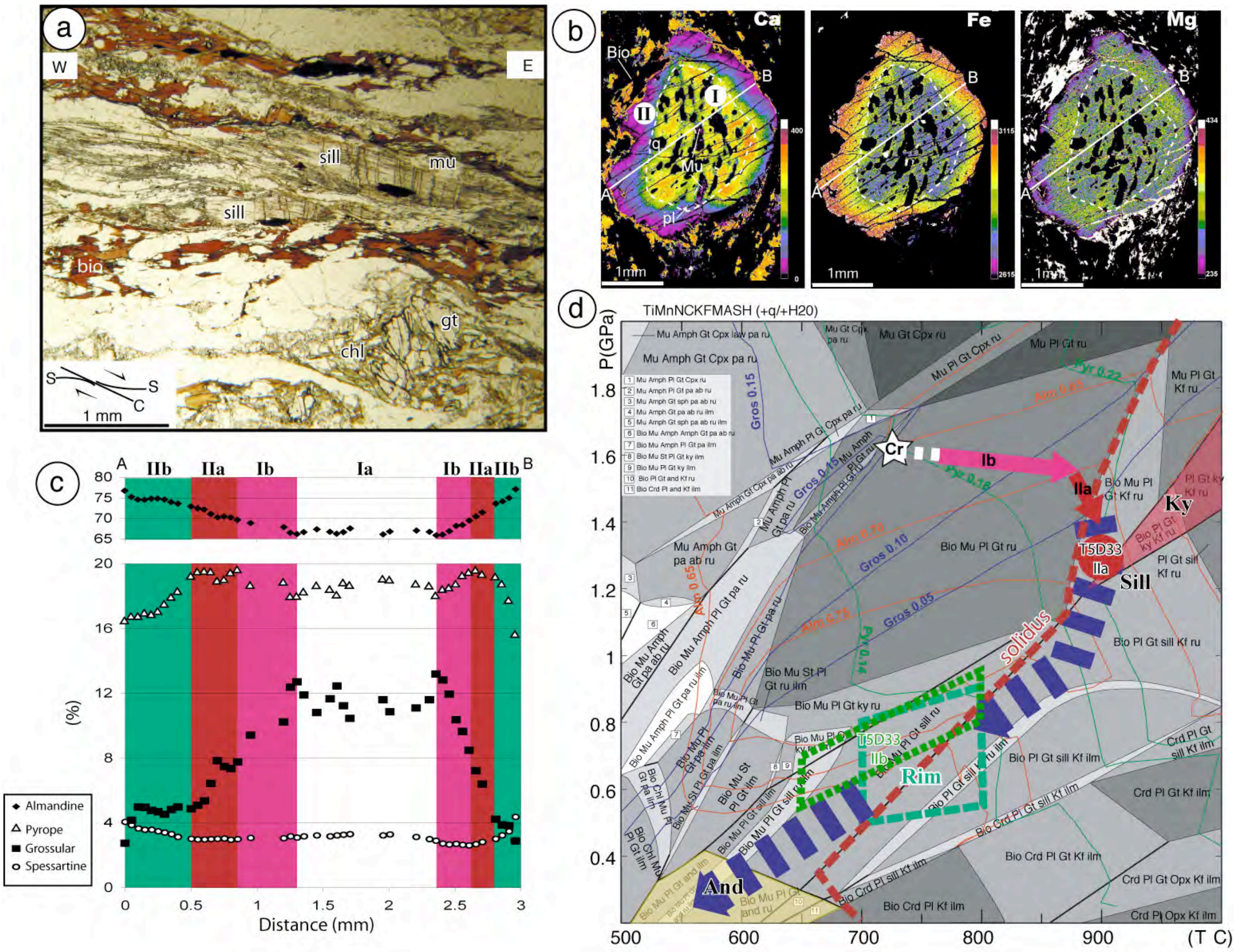

Fig. 6 : P-T path of the Ama Drime Paragneisses in the footwall of the Dinggye normal fault.
a) T5D33 thin section picture microphoto showing syn-sillimanite-bearing top to the east shear planes. Optical microscope, section parallel to lineation and perpendicular to foliation. **b)** X-ray maps showing Ca, Fe and Mg compositional zoning of garnets in sample T5D39b. **c)** Garnet composition along the profile (white line) schown in b). **d)** H_2O satured NCKFMASMnTi pseudosection for garnet-biotite-sillimanite micaschist T5D39b (Perple_X2007) for the corresponding whole-rock composition. White, light grey, medium grey and dark grey fields are di-, tri-, quadri- and quintivariant fields, respectively. Mineral abbreviations follow Holland and Powell (1998). Red, green and blue (color version) or heavy, ligth and dashed (b & w version) lines are almandine, pyrope and grossular isopleths, respectively. T5D39b P-T path is contrained by the white star (Cr : garnet core), pink and red arrows and the green long-dashed box (garnet outer rim). Constraints on T5D33 P-T path are plotted for comparison. In b), c) and d), I and II indicate garnet core (paragenesis 1) and rim (paragenesis 2), respectively.

4.1.2 P-T path of the Ama Drime Orthogneissic unit, comparison with the Paragneissic unit.

Lombardo and Rolfo (2000) were the first to suggest that the rocks now outcropping in the heart of the Ama Drime, here referred as the Ama Drime Orthogneissic unit, were among the deepest in the Himalayan belt. Since then, the P-T path of the Ama Drime unit, has been documented by the studies of Liu et al., (2005), Groppo et al. (2007), Liu et al., (2007) and Cottle et al. (2009). These studies appear to document a common P-T path (Fig. 5b). The path starts with an isobaric heating (ΔT~225°C) at pressures above 1.4 GPa, most probably between 1.6 GPa and 1.8 GPa, prior to reach conditions compatible with partial melting at ~800°C of metapelitic / metagranitic rocks. This is followed by a large nearly adiabatic decompression (ΔP = 1.0 to 1.5 GPa corresponding to 37 to 56 km) at

~800°C, ending around 0.3 GPa (~11 km depth). From this point, cooling starts and the path entered the field were vapor-absent melting for metapelite and metagranite may initiate (Fig. 5b). The end of the P-T path is still poorly constrained.

Such P-T path is broadly similar to the one obtained in the overlying Ama Drime Paragneissic unit (see section 4.1.1), but with a peak temperature ~100°C cooler (Fig. 5d). From these data the Ama Drime Paragneissic unit could simply corresponds to the metamorphosed sedimentary cover of the Ama drime Orthogneissic unit, the two units being exhumed together. However, the two units can also be separated by a tectonic contact along the postulated Nyonno Ri Boundary, which finite offset would be small.

4.2 *Geochronology*

4.2.1 U-Th/Pb

T5D22 is a sample from the migmatitic gneisses, which constitute most of the Ama Drime orthogneissic unit, sampled south of the Nyonno Ri in the footwall of the Dinggye normal fault (Fig. 2b).

Monazites selected for SHRIMP dating are fairly big (100 μm in average) and well crystallized. In thin section, they are observed as inclusion within micas and quartz. No significant relationship appears between the age and the spot locations (Table DR4-2). T5D22 monazite ages show scatter, with $^{208}Pb/^{232}Th$ ages ranging from 11.6 to 14.4 Ma, for an average at 12.85±0.39 Ma (n=15, MSWD=3.3) (Fig. 7a). On a Tera-Wasserburg isochron most data concentrate just above the Concordia (Fig. 7b). If one excludes the youngest and the 3 oldest data points, regression forced through present day common lead and the 11 remaining data, gives an age of 13.54±0.14 Ma (MSWD 1.9) (Fig. 7b). Keeping all points would not change the age (13.59±0.27 Ma) but would significantly alter the MSWD (10.8). The TW regression age is 1Ma older than the $^{208}Pb/^{232}Th$ average one. In the absence of any clue for lead over-correction, the average age is preferred.

As monazite is easily dissolved into the melt during partial melting and appears during final melt crystallization (Kelsey et al., 2008), the 12.9 Ma age most likely represent final melt crystallization.

This age of ~12.9 Ma is close to other monazite ages found in the Ama Drime orthogneisses west of the range: 12.8±0.2 (sample 1303, Liu et al., 2007), 13.4± 1 Ma (sample 1203, Liu et al., 2007), and 12.3±1.5 Ma (sample AD36, Cottle et al., 2009), confirming crystallization of the Ama Drime migmatites at that time (Fig. 9). In such rocks however, zircons rims yield older Cenozoic ages of 33±2.1and 22.9±2.1 in sample 1103, and between 30 and 23 Ma in sample 1303 (Liu et al., 2007) that could correspond to previous magmatic evolution (Fig. 9).

T5D5 is a small (~10 cm wide) leucocratic dyke crosscutting the ductile foliation in the footwall of the Dinggye fault in the Ama Drime orthogneissic unit (Fig. 3cj, Fig. 2b). Monazites are well crystallized and fairly big (100 μm in average). In thin section, they are observed as inclusion within micas and quartz. Some grains were systematically avoided for dating because CL images revealed they were patchy, or had zircon inclusions. Corrected $^{208}Pb/^{232}Th$ ages range from 10.4 Ma to 13.9 Ma (Table DR4-1, Fig. 7a). The average of the whole population is 12.52 ± 0.54 Ma with a fairly strong MSWD at 6. A cumulative probability plot exhibits two maxima at ~11 and ~13 Ma suggesting two age populations (Fig. 7c). Average $^{208}Pb/^{232}Th$ ages of the two sub-populations are 13.09±0.32 Ma (MSWD=1.5) and 10.98±0.39 Ma (MSWD =1.13), respectively (Fig. 7a, Table DR4-1). When plotted in a Tera-Wasserburg diagram, the data display again two statistically different populations, whose ages do not overlap within uncertainties. Regressions forced though present day common lead give intercepts at 13.96±0.27 Ma (13 points, MSWD=1.9) and 12.54±0.47 Ma (5 points, MSWD=1.5) for these two populations (Fig. 7d, table DR4-1).

We interpret these results as indicating a long period of monazite crystallisation with final dyke emplacement at the time of the youngest monazite crystallisation: 10.98±0.39 Ma. This suggests that down to the east ductile normal faulting was over, at least locally, at ~11 Ma. Note that the oldest monazite population in T5D5 is very similar to the monazites from T5D22 (Fig. 9) and thus probably corresponds to inheritance from this main crystalization event.

T5D26 is a pegmatite dyke that cuts across an amphibolite-rich layer (Fig. 3bh) of the Ama Drime orthogneissic unit ~4 km west of the Dinggye active fault (Fig. 2). The dyke is restricted to the basic layer and does not appear to cut the migmatites. However, observation of similar dykes in the high cliff north of the Ama Drime summit reveals that the dykes cut across all facies of the Ama Drime orthogneissic unit even if they are locally restricted to the basic layers probably because of rheology contrasts (Fig. 3bf).

The sample yielded clear elongated zircons with well develop facets and no zoning. In thin section, they are observed as inclusion within micas and quartz. All the analyzed points are concordant but show a wide range in age from 7 to 27 Ma (Fig. 7d, Table DR3), thus yielding the youngest concordant ages from this study. The distribution of $^{206}Pb/^{238}U$ ages, which suffer the least from ^{204}Pb correction shows 9 ages out of 12 ages younger than 12 Ma. The average of these ages (9.8 ± 1.2 Ma, MSWD=126) is interpreted as the best estimate for the pegmatite crystallization. The few older ages, between 21 and 27 Ma, suggest zircons inherited from the surrounding Ama Drime orthogneissic unit (Fig. 9). One cannot exclude however that the data correspond to a discordia chord between ~7 and ~27 Ma. In that case the crystallization age of T5D26 would be 7.3 **±** 0.2 Ma.

The 9.8 ± 1.2 Ma age is close to the crystallization age of T5D5 (10.98±0.39 Ma, see above) that seems to belong to the same dyke generation from field observation (Fig. 2b). On the western side of the range, six monazites of a leucocratic dyke crosscutting a large amphibolite boudin (AD 35, Fig. DR7) yield an age of 11.6±0.4 Ma (Cottle et al., 2009) very close to the final crystallization age we propose for T5D26 and T5D5.

Section/site	Sample				Average 206/238 age for zircon and 208/232 age for monazite					Inverse isochron (Terra Wasserburg) 207/206 vs 238/206				
	Number	facies	Altitude	Mineral type		Age, Ma	MSWD	Number of spots	Spots (crystal n° / boder or core)	Age, Ma	Upper Intercept	MSWD	Number of spots	Spots (crystal n° / boder or core)
Dingyye normal fault	T5D5	late leucocratic dyke	5065	Monazite	population 1	**11.1 ± 0.4**	1,1	6	15c, 13c, 19bc, 3c, 3b, 9bc	12.5 ± 0.5	Common lead	1,5	5	15c, 13c, 19bc, 3c, 3b
					population 2	**13.1 ± 0.3**	1,5	12	18c, 10b, 11c, 7c, 11b, 6c, 12c, 16b, 4c, 14c, 17c, 1c	14.0 ± 0.3	Common lead	1,9	13	9bc, 18c, 10b, 11c, 7c, 11b, 6c, 12c, 16b, 4c, 14c, 17c, 1c
					whole sample	12.5 ± 0.5	6,1	18	all spots					
	T5D22	migmatitic orthogneiss	5346	Monazite		**12.9 ± 0.4**	3,3	15	all spots	13.5 ± 0.1	Common lead	1,9	11	2.2,8.1,7.2,1.3,3.1,7.1 9.1,1.2,4.1,6.1,1.1
	T5D26	undeformed late pegmatite	5419	Zircon		**9.8 ± 1.2**	126	9	6b2, 4b, 1c, 7c, 5b2, 6b1, 8c, 3b, 3c					

Table 2 :U-Th/Pb data summary.

See Fig. 7. For sample locations see Table 1and Fig. 2a. Detailed data are given in Table DR3 and Table DR4. Most reliable results are in bold.

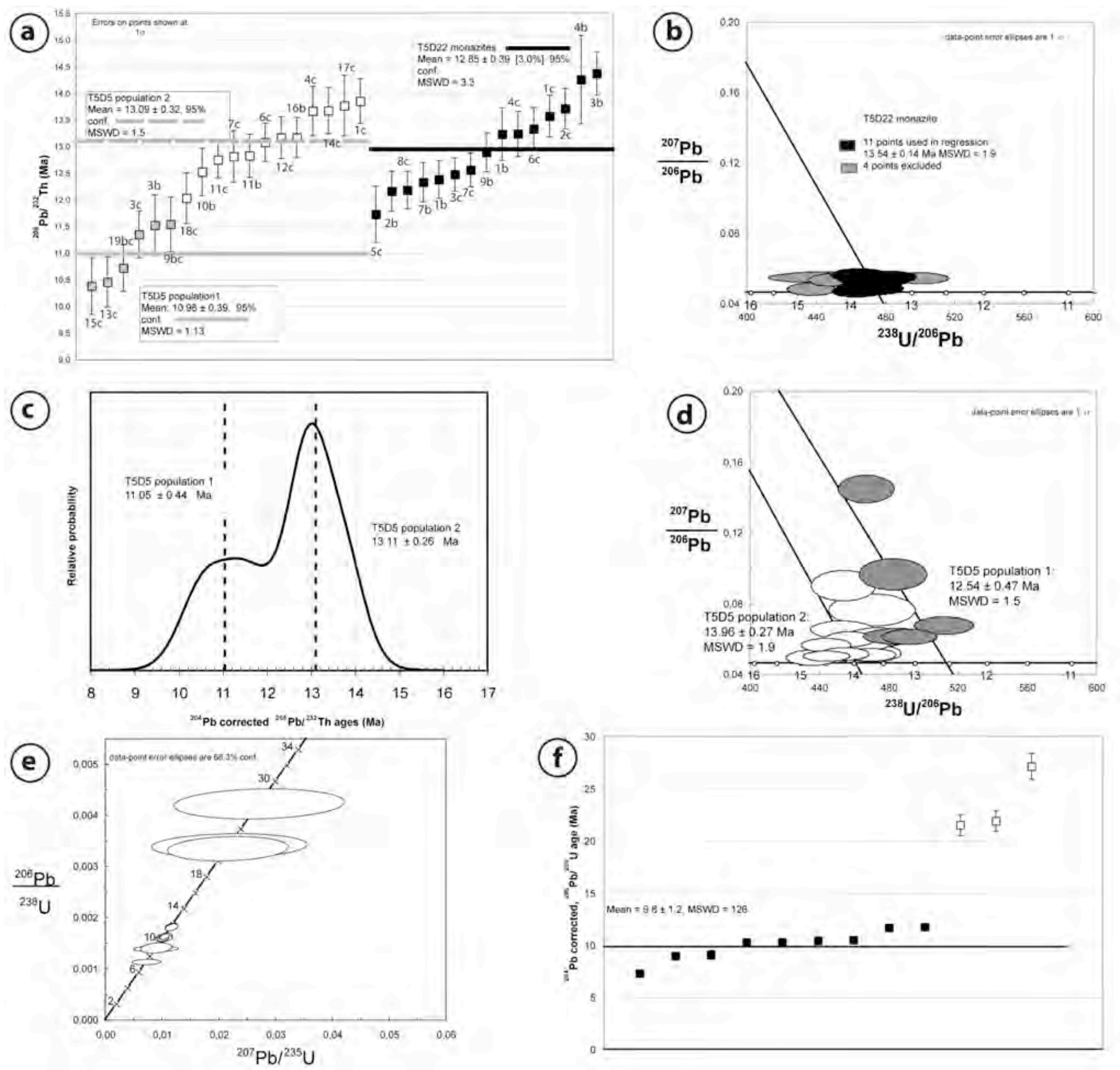

Fig. 7 : U-Th/Pb data.
Corresponding data are listed in table DR3 and DR4. ***a)*** *Averages of $^{208}Pb/^{232}Th$ monazite ages corrected for common lead via 204Pb for T5D5 (2 populations) and T5D22. Spot numbers are indicated* ***b)*** *T5D22 monazite Tera-Wasserburg diagram, with regressions forced through present day common lead.* ***c)*** *Cumulative probability plot of T5D5 monazite $^{208}Pb/^{232}Th$ ages from which isoplot software (Ludwig, 2003) extracts two subpopulations.* ***d)*** *T5D5 monazites Tera-Wasserburg diagram, with regressions forced through present day common lead (2 populations are distinguished).* ***e)*** *Concordia diagram for zircons from pegmatite dyke (T5D26). All points are concordant but show a wide age range.* ***f)*** *T5D26 zircon $^{206}Pb/^{238}U$ corrected for common lead via ^{204}Pb ages. A crude average (with a high MSWD) is calculated excluding the three oldest points.*

4.2.2 Argon results

Argon results are summarized in Table 3 and all data are listed in Table DR5.

• Dinggye shear zone.

New argon ages from the Ama Drime paragneissic unit in the footwall of the Dinggye normal fault were obtained from T5D33 and T5D39. Biotites from paragneiss T5D33 show a saddle shaped age spectra with minimum ages at ca 11.8 Ma (Fig. 8a), suggesting excess, which is correctly resolved by the inverse isochron approach yielding an age of 10.8±0.4 Ma (MSWD = 7.1) (Fig. 8b). Biotites from sample T5D39 also display a rugged age spectra, with a minimum age close to 11.5 Ma (Fig. DR8g). Excess argon is not completely resolved on the inverse isochron, which age of 13.1±0.8 Ma is probably a maximum (Fig. DR8h). That range of Biotite ages in the paragneisses compares well with that obtained by Zhang and Guo (2007) on similar facies, ranging from 10.2 to 13.2 Ma.

Within the Ama Drime orthogneissic unit, sample T5D6 corresponds to an orthogneiss showing down to the east ductile normal faulting and cross-cut by T5D5 leucogranite (Fig. 3cj). Biotites yield a saddle-age spectra with a pseudoplateau at 10.8±0.1 Ma and an inverse isochron age of 10.7 ± 0.3 Ma (Fig. 8a,b). Cooling of T5D6 below ~300°C thus happened immediately after the emplacement of T5D5. In the same unit, T5D10 biotites show a strong excess argon effect (Fig. DR8g). The inverse isochron is tied up close to the $^{36}Ar/^{40}Ar$ axis and points to an old age of 18.6±1.2 Ma, which must be regarded with great care (Fig. DR8h).

Six Muscovite and biotite $^{39}Ar/^{40}Ar$ ages from the footwall of the Dinggye fault were published by Zhang and Guo (2007) (samples T01-17, 24, 25, 26, 29, 33, Fig. DR7). All these ages are comprised between 13.34 and 10.2 Ma, which together with our data yield an overall age range between 18.5 and 10.2 Ma (Fig. 9). Excluding only one outlier (T5D10 biotite that appends to be the less reliable) out of the eleven available data restrains the age range to 13.7 –10.2 Ma and yield average ages of 10.72 ± 0.73 Ma for the biotites and 12.1 ± 2.4 Ma for the muscovites (Fig. 9). Muscovites and biotites have nearly the same age suggesting a very rapid cooling at medium temperatures. This event is ~2 Myr younger than the rapid cooling event observed in the STDsz (Leloup et al., 2009; Leloup et al., submitted) and corresponds to the final age of crystallisation of T5D5 (crosscutting dyke).

• Kharta shear zone (Kharta sz)

On the western side of the Ama Drime range micas $^{39}Ar/^{40}Ar$ ages in the Kharta shear zone appear even younger than on the eastern flank.

T7A19 biotites yield the oldest ages with a saddle age spectra, a pseudo plateau at 24.1±0.3 Ma and an isochron age of 23.5±0.5 (Fig. DR8a,b). T7A33 biotites show the same kind of age spectra with a 10.9±0.2 Ma plateau with a similar isochron age of 10.1±0.9 Ma (Fig. DR8a,b). The pseudo plateau age of T7A10 biotites is 8.5±0.2 Ma and the isochron age is 8.5±0.3 Ma (Fig. DR8c,d). T7A14 biotites show minimum ages around 10 Ma and an ill-defined isochrone age of 6.2±0.8 Ma (Fig. DR8c,d). All these biotites come from the ductile part of the Kharta normal fault, which deformation temperature encompasses the biotite closure temperature (300±40°C). This suggests that the Kharta sz was active in the time interval 10 – 6 Ma, while T7A19 was probably not reset from a previous thermal event (Fig. 9). Indeed, T7A19 is a meta-arenite in which biotite, plagioclase, garnet and quartz detrital grains have only been partly re-crystallized during shearing and chlorite-grade metasomatism within the Kharta sz. We thus suggest that T7A19 biotites cooled below ~300°C at ~25 Ma were eroded and deposited in a small basin later affected by the Kharta sz.

T7A20 sampled within the Kharta sz less than 200m away from T7A19 (Fig. 2a) contains two generations of muscovite: big (~0.2 mm) porphyroclasts and smaller minerals aligned within the foliation and shear zones. Two populations of muscovite have also been distinguished during the separation process on their clear or rusty appearance. The two populations have been dated separately. The clear one shows a pseudoplateau at 6.6±0.1 Ma and an inverse isochron at 6.2±0.2 Ma (Fig. 8c,d), while the rusty one is associated with a saddle age spectrum and an ill-defined isochron age of 3.4±0.6 Ma (Fig. 8c,d).

Section/site	Sample				Plateau Age			Inverse Isochron Age				Total Fusion Age
	Number	Rock type	Altitude	Mineral type		Age, Ma	Steps	Age, Ma	40Ar/36Ar$_i$	MSWD	Steps	Age, Ma
Dinggye shear zone	T5D6	orthogneiss	5069	biotite	SMA	10.8 ± .1	4 steps/14 (7-10) 56% of gas	**10.7 ± 0.3**	354 ± 12	6,3	9 steps/14 (4-12) 90% of gas	12.1 ± 0.1
	T5D10	garnet migmatitic gneiss	5237	biotite				18.6 ± 1.2	343 ± 2.5	2	11 steps/11 100% of gas	49.6 ± 0.6
	T5D33	garnet-sillimanite paragneiss	5124	biotite				**10.8 ± 0.4**	382 ± 9	8	9 steps/14 (5-13) 90% of gas	13.7 ± 0.1
	T5D39	garnet-sillimanite paragneiss	not in place	biotite				<13.1 ± 0.8	319 ± 13	15,4	8 steps/14 (5-9,11-13) 90% of gas	16.5 ± 0.3
Kharta shear zone	T7A19	mylonite	3670	biotite	WMP	24.1 ± 0.3	6 steps/14 (7-12) 81% of gas	**23.5 ± 0.5**	318 ± 5	5,3	10 steps/14 (4-13) 56% of gas	25.5 ± 0.3
	T7A33	gneiss	3658	biotite	WMP	**10.9 ± 0.2**	5 steps/14 (7-11) 68% of gas	10.1 ± 0.9	345 ± 33	14,4	5 steps/14 (7-11) 68% of gas	21.6 ±0.2
	T7A10	orthogneiss	4446	biotite	SMA	8.5 ± 0.2	2 steps/14 (7-8) 52% of gas	**8.5 ± 0.3**	339 ± 11	6,4	6 steps/14 (7-12) 79% of gas	10.9 ± 0.1
	T7A14	deformed microgranite	4445	biotite				6.2 ± 0.8	688 ± 114	4,4	6 steps/14 (6-11) 54% of gas	12.2 ± 0.1
	T7A20	cataclastic orthogneiss	3670	muscovite fresh	SMA	6.6 ± 0.1	5 steps/14 (8-12) 59% of gas	**6.2 ± 0.2**	402 ± 8	3,7	10 steps/14 (2-5, 8-13) 97% of gas	8.4 ± 0.1
				muscovite rusty				3.4 ± 0.6	455 ± 11	5,9	6 steps/14 (5-10) 61% of gas	34.9 ± 0.3
	T7A48	quartz cataclasite with chlorite and muscovite recrystalisation	3677	muscovite fresh	WMP	11.7 ± 0.2	5 steps/10 (2-7) 70% of gas	**12.2 ± 0.2**	293 ± 3	0,1	5 steps/10 (2-7) 70% of gas	17.6 ± 0.2
				muscovite rusty				**3.3 ± 0.8**	875 ± 37	3,8	8 steps/14 (6-13) 85% of gas	44.7 ± 0.5

Table 3 : Ar/Ar data summary

See Fig. 8 and Fig. DR8. For sample locations see Table 1 and Fig. 2a. Detailed data are given in Table DR5. Most reliable results are in bold

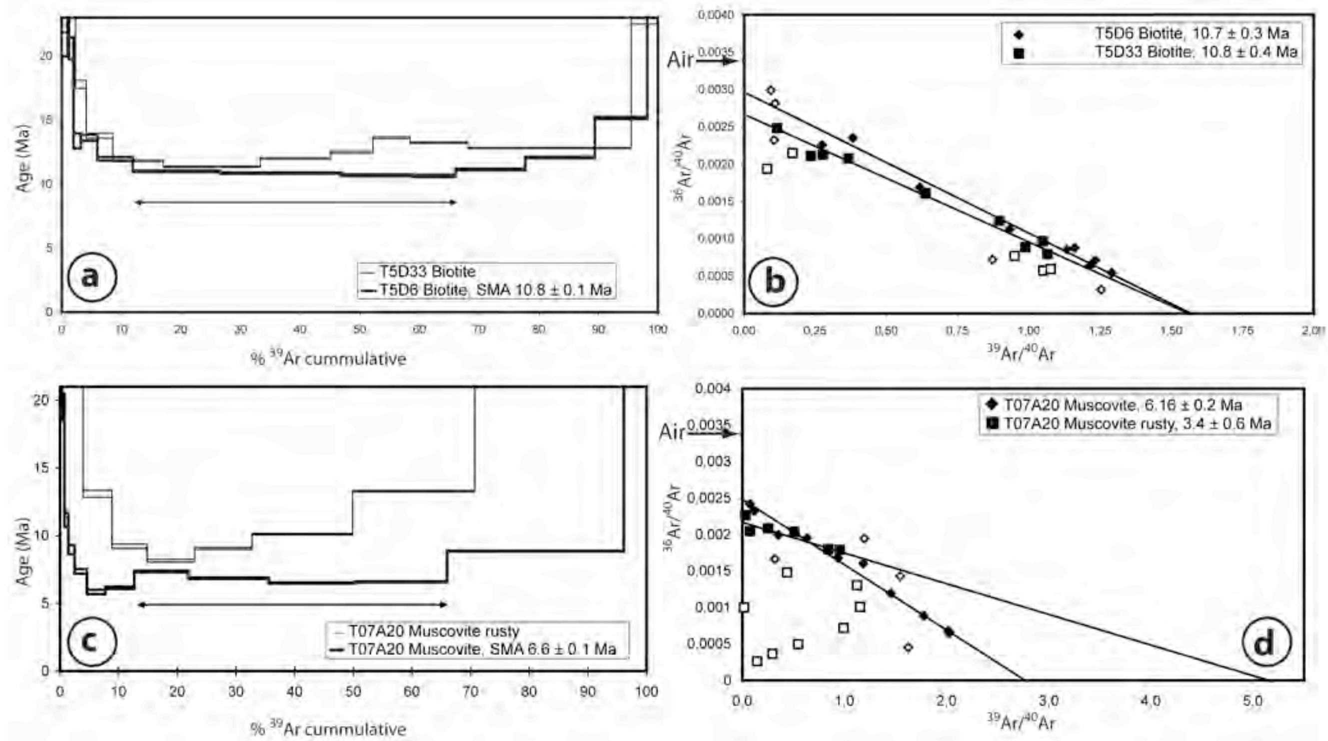

Fig. 8 : Examples of Argon Data from the Ama Drime range.

Other data are plotted in Data Repository DR8. All data are summarized in Table 3 and listed in Table DR5. For inverse isochron plots, empty symbols where not used in the regression calculation.

a) T5D33 and T5D6 biotites age spectra. **b)** T5D33 and T5D6 biotites inverse isochron plot. **c)** T7A20 muscovites age spectra. Note that two populations (normal and rusty) have been distinguished. **d)** T7A20 muscovites inverse isochron plot.

T7A48 comes from the north part of the Ama Drime range in the hanging wall of the fault linking the Kharta and Sangkar active faults (Fig. 2a). There, cataclastic quartzites outline NNW trending normal faults (see 3.2.3). The sample yielded two generations of muscovite: clear porphyroclasts within the foliation of the cataclasite, and rusty muscovites that, together with chlorobiotite, fill vertical late fractures. The porphyroclasts yield ages close to those of most muscovites from the Dinggye sz (Zhang and Guo, 2007; Fig. 9), with a saddle pseudoplateau at 11.7±0.2 Ma and an inverse isochrone at 12.2.±0.2 Ma (Fig. DR8e,f). The second muscovite generation gives a saddle age spectrum without any plateau and an ill-defined isochron age of 3.3±0.8 Ma (Fig. DR8e,f).

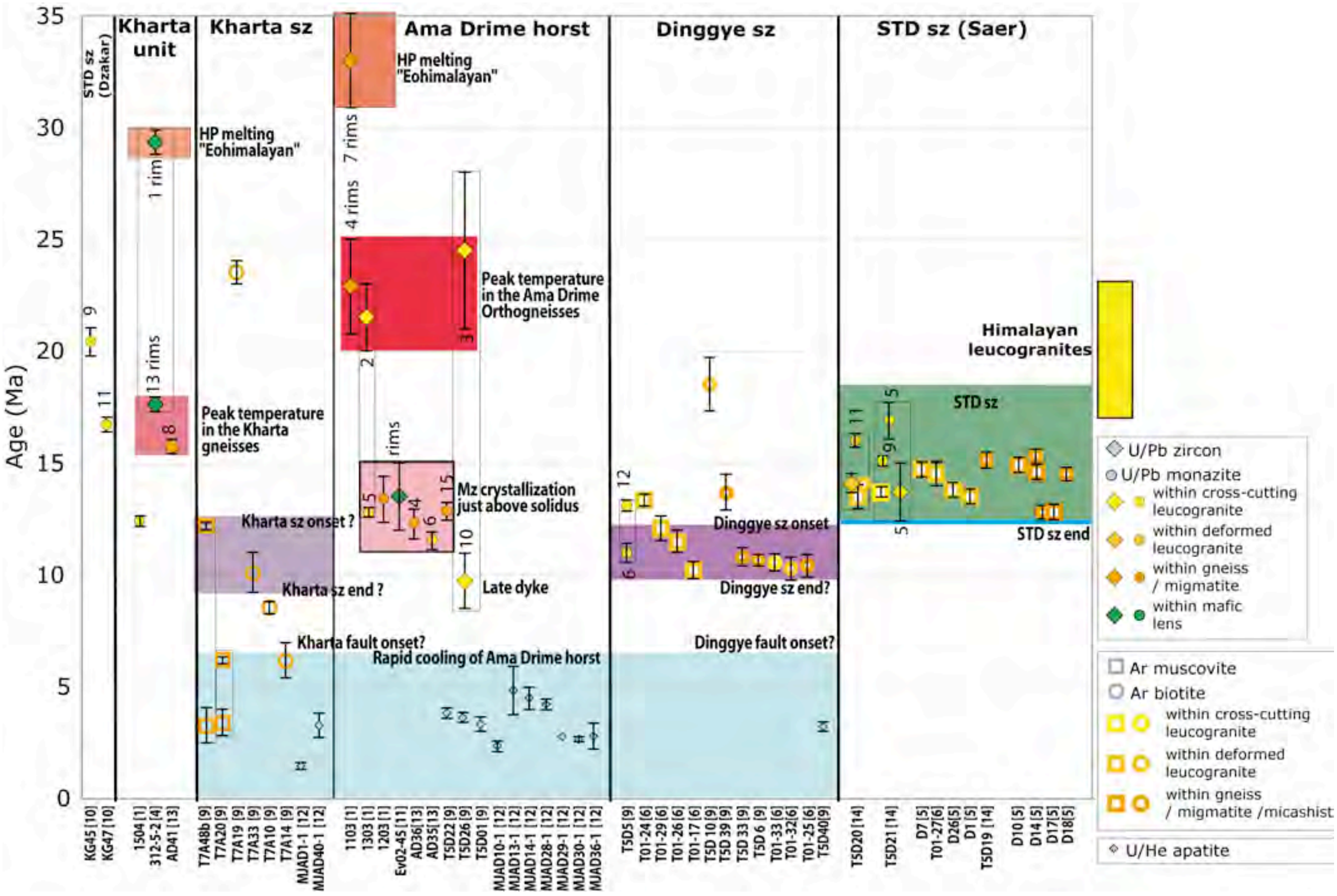

Fig. 9 : Geochronologic ages synthesis.

Geochronologic ages of Ama Drime area from bibliography and this study. Samples are labelled at the bottom of the graph and organized by tectono-metamorphic units presented from West to East. Symbols correspond to mineral and techniques while colours relate to rock types. References are: [1] Liu et al., 2007 ; [4] Li et al., 2003 ; [5] Hodges et al., 1994 ; [6] Zhang and Guo, 2007 ; [9] This study ; [10] Cottle et al., 2007; [11] Rolfo et al., 2005; [12] Jessup et al., 2008; [13] Cottle et al., 2009 and [14] Leloup et al., 2009; Leloup et al., submitted. The age range of Higher Himalayan leucogranites is plotted for comparison. (Harrison et al., 1998). Main tectono-metamorphic events are outlined by color boxes.

4.2.3 Apatite U-Th/He results.

In order to constrain the timing of the latest stages of exhumation of the Ama Drime massif in the footwall of the Dinggye normal fault, apatite (U-Th)/He dating was performed on 3 samples from the valley south of the Nyonno Ri (T5D01, 22 & 26) spanning in elevation between 5217 and 5419 m, and one sample collected east of the

Sangkar Ri at 4270 m (T5D40) (Fig. 2a). Samples are orthogneiss (T5D01), migmatite (T5D22) and granites (T5D26 and T5D40). Apatites have been analysed at the Caltech Noble Gas Laboratory following the procedure of House et al. (2000). As the samples were relatively poor in good quality apatite (i.e. inclusion free) we ran single grains and 1 (T5D01), 2 (T5D40) or 4 replicates (T5D22 & 26). The 1σ error on age is taken as the standard deviation of the replicate analyses divided by $(n-1)^{1/2}$ where n is the number of replicate analyses performed. Samples with multiple replicates gave good reproducibility, with a 1σ error lower than 10% of the mean age. For the sample with only one replicate (T5D01) we use a conservative 1σ error corresponding to 10% of the age.

All ages range between 3.2 and 3.8 Ma (average: 3.4 ± 0.4 Ma), (DR6; Fig. 9). Altogether ages appear to correlate with elevation giving an apparent exhumation rate of ~2.9 km/Ma (Fig. 10). However this correlation rests on only four points, and the single point at an altitude significantly lower than the 3 others is located ~35 km further to the North (T5D40, Fig. 2a). Other apatite (U-Th)/He ages have been obtained by Jessup et al. (2008) for samples (i) close to samples T5D01, 22 & 26, (ii) from the western side of the Ama Drime massif next to the Kharta normal fault and (iii) in the core of the massif. All these samples are located between 28°4'N and 28°15'N (Fig. DR7). Altogether most of Jessup et al. (2008) apatite (U-Th)/He ages and our data for samples T5D01, 22 & 26 correlate with elevation (Fig. 10) defining and apparent elevation rate of ~1 mm/yr for ages comprised between 1.4 and 4.2 Ma. The two samples (MJAD13 & MJAD14) from Jessup et al. (2008) with errors superior to 10% of the mean age, have been excluded from the age-elevation relationship as for these samples age replicates correlate negatively with grain size, which suggest He implantation, but that can also be related with zoning or presence of U-rich inclusions. Another sample (MJAD40) is significantly older than expected from the age – elevation relationship (Fig. 10). This sample is located in the Kharta shear zone and was then most probably less exhumed than the sample located in the range outside of the deformation zones explaining the relatively old measured age.

The age – elevation relationship obtained (Fig. 10) suggests that the part of the Ama Drime massif covered by Jessup et al. (2008) and our sampling (i.e. the central part between the Nyonno Ri and the Ama Drime peaks) was exhumed as a single block with no tilting between the Dinggye and the Kharta normal faults since at least 4.2 Ma. This implies that in this area, and since 4.2 Ma, the slip rate is the same on both normal faults. The relatively old age obtained for sample T5D40, located about 35 km north of the other samples could indicate a lower amount of exhumation towards the northern Ama Drime, where the normal faults terminate. This is coherent with the decrease of the crest elevation (~6000 m in the central part and ~5500 in the northernmost part), together with the decrease of the height of the triangular facets (700-800 m in the central part and 400-500 in the northernmost part), both suggesting a decrease of the throw / rate of the active faults toward the north.

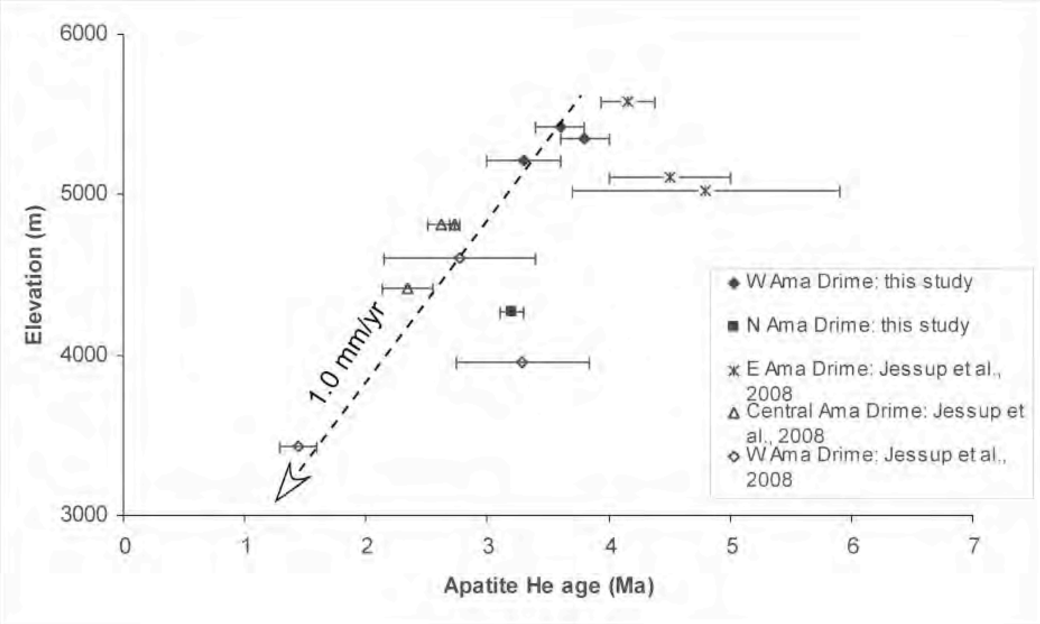

Fig. 10 : Plot of Ama Drime (U-Th)/He apatite ages versus elevation.
Data from this study (Table DR6) and Jessup et al. (2008) (Table DR10). This plot suggests that the Ama Drime range was vertically exhumed as a single block since at least 4 Ma with a rate of about 1 mm/yr. See text for details.

5 Discussion: structural evolution of the Ama Drime area.

In the central and eastern Himalayan range, amphibolitic and granulitic rocks recording peak pressure between 1.2 and 1.0 GPa have been observed close to the MCTl (Guillot, 1999; Kohn et al., 2001; Harris et al., 2004). Further North, in the HCS, between the MCTl and the STD shear zone peak pressure is usually comprised between 0.7 and 1.0 GPa (Vance & Mahar, 1998; Searle et al., 1999; Vannay et al., 1999; Goscombe & Hand, 2000; Borghi et al., 2003; Dasgupta et al., 2004; Kohn et al., 2004). So far pressures higher than 1.4 GPa are only found in the Ama Drime range.

PTt path reconstructions of the amphibolitic and granulitic events of the HCS evidence that two main tectonometamorphic events occurred all across the Himalaya. One Eo-himalayan event, between 50 and 30 Ma, probably associated to burial and subsequent thermal re-equilibration (see Hodges, 2000 and Kohn et al., 2005 for review) and one HT event at 25-20 Ma related to leucogranite formation (Simpson et al., 2000). PT path reconstruction, away from the STD shear zone, indicates that this HT event is generally coeval to a slight T increase (50-100°C) and a strong decompression (Guillot, 1999; Searle et al., 1999; Goscombe & Hand, 2000; Harris et al., 2004). This HT event is generally considered as contemporaneous with thrusting along the MCTl (Hodges et al., 1996; Catlos et al., 2004).

We discuss below if, and how, the Ama drime area rocks conform with, or depart from this general pattern, and what constraints their P-T-D-t path brings on orogenic models.

5.1 P-T-t path of Ama Drime rocks during the Himalayan orogeny

Comparison of the P-T paths of the various units and compilation of more than 60 radiochronologic data (Fig. 9, Table 2, Table 3), allow us to propose a coherent scenario for the timing and duration of the metamorphism and exhumation phases of the Ama Drime rocks during the Himalayan orogeny.

U-Th/Pb zircon and monazite dating of the Ama Drime orthogneissic unit, in orthogneisses, paragneisses, metabasites as well as undeformed leucocratic dykes and granites, yield Cambrian to Precambrian inherited ages as well as numerous Cenozoic ages between 33 and 10 Ma (Fig. 9). The Cambrian ages are characteristic of Himalayan Crystalline Series (Richards et al., 2005 and reference therein).

The Cenozoic ages indicate that the High-Temperature and High-Pressure, metamorphic event is Oligo-Miocene and relates to the Himalaya building, not to a previous metamorphic episode. However, the detailed interpretation of these ages is not always straightforward. The spread in age results from the variety of minerals and facies dated as well as from mechanisms inducing several age populations of a given mineral in a given sample.

Published U/Pb ages of the Ama Drime migmatitic paragneisses in the Ama Drime orthogneissic unit reveal two populations of metamorphic zircon at 33±2 Ma and 23±2 Ma (sample 1103, Liu et al., 2007) (Fig. 9). In such amphibolitic to granulitic facies rocks metamorphic zircon are only formed during anatexis (Schiotte et al., 1989; Vavra et al., 1999). In this environment overgrowth mostly occurs during two phases (1) subsolidus growth at the onset of partial melting and (2) at peak temperature and during subsequent cooling (Roberts et al., 1997; Schalteger et al., 1999; Vavra et al., 1999; Rubatto et al., 2001; Kelsey et al., 2008). In metapelitic system partial melting temperature is dependant of the bulk composition. Based on granite chemistry and our pseudosection, partial melting is related with vapor-absent melting by mica breakdown (Visona and Lombarado, 2002). Combining data from experimental petrology at ~1.4-1.8 GPa (Vielzeuf & Holloway, 1988; Vielzeuf & Clemens, 1992; Vielzeuf & Montel, 1994; Patiño Douce & Beard, 1996; Castro et al., 2000; Auzanneau et al., 2006) as well as pseudosection calculation (Harris et al., 2004; Indares et al., 2008), pelites, granites and greywakes partial melting initiate between 800 and 900°C. We propose that the 33±2 Ma age corresponds to the onset of partial melting most probably occurring during the isobaric temperature increase, and the 23±2Ma age to the peak T and start of the subsequent cooling (1.0 to 0.5 GPa and ~800 - 850°C (Fig. 5b). We note that zircons of similar ages have been found in undeformed granites and leucogranitic dykes of the Ama Drime (sample 1033 of Liu et al. (2007) and T5D26 of this study; Fig. 9) where they are probably inherited from this high temperature event.

Monazites ages obtained from similar migmatitic gneisses are all comprised between 13 and 12 Ma (this study; Liu et al., 2007; Cottle et al., 2009) (Fig. 9). As monazite is easily dissolved during partial melting, inherited or prograde grains are usually not preserved, and U-Th/Pb ages most likely correspond to cooling close to the solidus (Kelsey et al., 2008). Based on a detailed study on various bulk rock compositions in the NCKFMASH system, monazite crystalisation occurs between 650 and 850°C for pressure below 0.7 GPa (Kelsey et al., 2008).

We propose that the 12-13 Ma monazite ages correspond to PT conditions of 0.3-0.4 GPa and 650-750°C occurring during the cooling event following the adiabatic decompression (Fig. 5b).

Within metabasic rocks of the same Ama Drime orthogneissic unit, Rolfo et al. (2005) obtained 12-15 Ma U/Pb ages on metamorphic zircons. In such rocks zircon growth is rather related with garnet and /or hornblende breakdown than anatexis (Fraser et al., 1997). Thus Groppo et al., (2007) coupling these ages with their petrogenetic grid proposed that 12-15 Ma zircon growth most probably occurred at 0.7-0.4 GPa and 750-840°C near the end of the nearly adiabatic decompression event. Such timing matches well our interpretation of the monazites and zircons ages in the migmatitic orthogneiss (Fig. 5b).

5.2 P-T-t paths of the Kharta-Saer unit

East of the Ama Drime, the 15.09±0.11 Ma U-Th/Pb age of a crosscutting granite (T5D21) suggest that deformation stopped in the STDsz at ~15 Ma east of Saer (Leloup et al., 2009; Leloup et al., submitted) (Fig. 9). Muscovite and biotite argon ages further suggest rapid cooling between 15 and 13.5 Ma and that temperature dropped below ~300°C at ~13.5Ma (Fig. 5; Fig. 9). Brittle motion could have carry on along the STD after that date. However, the STD is offset by the Dinggye shear zone, which was active before ~11 Ma, because T5D5 dyke dated at 11±0.4 Ma (Fig. 7a,c; Table 2) crosscuts the foliation. Motion on the STDS thus stopped between ~13.5 and 11 Ma (Leloup et al., 2009; Leloup et al., submitted). Together with the P-T path, this indicates that rocks now outcropping in the STDsz near Saer were at less than 0.1 GPa pressure (~4 km depth) at the end of motion along the STDS (Fig. 5c).

West of the Ama Drime within the Kharta gneiss, U/Pb zircon ages from a granulitic metabasite are mostly around 17.6±0.3 Ma with two outliers at 29.5 ± 0.4 Ma and 1991 ± 26 Ma (sample 312-5-2; Li et al., 2003). If the last age is clearly inherited from the protolithe, the Cenozoic ages provide constraints on the timing of Himalayan metamorphism. As previously discussed in metabasic rocks zircon most likely form following garnet or / and amphibole breakdown (Fraser et al., 1997). Breakdown of garnet into orthopyroxene + plagioclase has been clearly identified in the sample dated by Li et al., (2003), but in the absence of chemical data the position of the garnet and amphibole reactions in the P-T space cannot be precicelly reconstructed. Bearing in mind that the rock bulk composition strongly influences the position of these reactions, first order estimates can be obtained by combining the petrogenetic grid of Groppo et al. (2007) with the PT path of the Kharta-Saer Unit proposed by Borghi et al. (2003). Zircon formation may have occurred (1) by amphibole breakdown during either isobaric heating or adiabatic decompression, and/or (2) by garnet breakdown during early decompression (Fig. 5a). We thus suggest that the 29.5 +/- 0.4 Ma zircon rim developed during the isobaric heating (Fig. 5a), while the 17.6±0.3 Ma zircon formed during the adiabatic decompression (Fig. 5a). Uranothorites within the melanosome of a migmatitic orthogneiss attributed to the Kartha gneisses and affected by deformation in the Kharta sz (AD41, Fig. DR7), yield a concordant U-Pb age of 15.8 +/- 0.2 Ma (Fig. 9) (Cottle et al., 2009). Cottle et al. (2009) interpret this age as the timing of partial melting. Based on partial melting curve for $P < 1$ GPa for metapelitic, metagranite and metagreywake (see Patiño-Douce & Harris, 1998 for a review), such event may above 700°C. Altogether, these data are compatible with high temperature conditions around 17-15 Ma. It is however not possible to determine precicelly to which pressure the obtained ages are associated.

5.3 From P-T-t to P-T-D-t: structures accommodating the exhumation.

Structural studies have identified several structures that could have accommodated the exhumation of the Ama Drime rocks and surrounding units since ~30 Ma. The first main structures are the MCT's (HHT/MCTu and MCT/MCTl) that do not outcrop in the Ama Drime area (Fig. 1b), but that most probably prolongate below (Fig. 1c). The STDS that lies immediately north of the investigated area may also have absorbed a significant part of the Ama Drime exhumation. Finally N-S normal faults and shear zones on both side of the Ama Drime horst have absorbed the final exhumation of the Ama Drime rocks. A detailed analysis of the P-T paths and available geochronologic data allows to decipher the timing and amount of exhumation linked with each structure.

5.3.1 differential exhumations

All P-T paths of the Kharta area share a nearly isobaric heating prior to decompression. When timing constraints are available, this isobaric heating appears to starts at ~30 Ma, corresponding to the Eo-himalayan stage of metamorphism described elsewhere in the Himalayas. This event can be used as a reference for the relative exhumation amounts between the structural units of the Ama Drime Area. For example the ~0.2 GPa pressure difference (~7.5 km) observed between Saer and Kharta gives a first order estimate of the differential exhumation absorbed within the Kharta-Saer unit below the STDsz. Tibetan sedimentary series are epimetamorphic and have probably been exhumed by a very small amount since 12 Ma. Vertical exhumation linked with the STDsz can thus be estimated from the STDsz P-T path to be ≤ 0.6 GPa (22 km) at Saer (Fig. 5c).

The differential exhumation between the Ama Drime orthogneissic and paragneissic units appears very small, less than the uncertainty on the peak pressure of the ADO (Fig. 5b, d). There is thus no apparent motion on the Nyonno Ri boundary since more than ~30 Ma.

5.3.2 exhumation amounts at the time of STDS activity.

As discussed previously (see 5.2) motion along the STDS ended between 13.5 and ~12 Ma near Saer (Leloup et al., 2009; Leloup et al., submitted). Such timing when compared with the P-T-t path of the Ama Drime orthogneissic unit implies that the adiabatic decompression, larger than 1.0 GPa (37km) and most probably ~1.3 GPa (48 km), occurred during normal motion on the STDS (Fig. 5b). This interpretation differs significantly from that of Cottle et al. (2009), which relates the adiabatic decompression since 0.7-0.8 GPa to normal motion on the Dinggye and Kharta shear zones. In our interpretation, the total exhumation linked to the Ama Drime horst is less than 0.4 Gpa (15km). (Fig. 5b).

The amount of exhumation linked with the STDS measured on the Ama Drime rocks P-T path is 0.2 to 0.7 GPa higher than the ≤ 0.8 GPa value obtained by summing the relative pressure differences from deformation below the STDsz (0.2 GPa) and the STDsz itself (≤0.6 GPa see 5.3.1 above). This discrepancy may have several causes: a) Vertical motion could have occurred at the base of the Kharta unit and above the Ama Drime Orthogneissic unit for example on the Nyonno Ri Boundary. However, as discussed above, such motion, if any, is probably small. b) Increase of the dip of the STDS (and MCT) towards the South, could induce rotation of the HCS pile and larger uplift in the South than in the North. However, this last hypothesis is unlikely, as the STDS dips shallowly from the top of the Chomolangma to Rongbuk and appears to steepen, not flatten, farther North (Dzakar Chu section) (Fig. 2a). c) The differential estimates are only first order as they are based on global P-T path from whole units. d) A combination of these causes.

The amount of adiabatic decrompression appears to decrease away for the STD: ~1.3 GPa in the Ama Drime orthogneissic unit, 0.6 in the Ama Drime Paragneisses, 0.5 GPa in the Kharta gneiss and no adiabatic decompression in the STDsz (Fig. 5). This could be interpreted as a progressive decrease of the exhumation linked with the STDS together with the structural height, implying a distribution of down to the north deformation within the whole HHC metamorphic pile. However, the end of the adiabatic decompression was reached at ~16 Ma in the Kharta unit (Fig. 5a), at least 2 Ma earlier than in the Ama Drime orthogneissc unit (Fig. 5b). This is probably due to the fact that close to the surface (≤ 0.4 GPa or depths ≤15 km) the thermal gradient is so steep, because temperature at the surface is low, that even fast exhumation cannot stay adiabatic but is necessarily accompanied by cooling. As a matter of fact, gneiss in the STDsz never experienced adiabatic exhumation (Fig. 5c) because they are located at the top of the metamorphic pile. It follows that most, of the exhumation (and cooling) of the Kharta unit occurred coevally with the STDS (Fig. 5a), and that in the Ama Drime paragneissic unit, the amount of exhumation syn and post STDS are probably on the same order of the Ama Drime orthogneissic unit (Fig. 5d).

We estimate that, between ~30 and 12 Ma, ≤0.6 GPa (≤22 km) of vertical exhumation occurred linked to brittle motion on the STD and ductile deformation in the STDsz. This corresponds to exhumation rates on the order of ≤1.2 mm/yr immediately below the STDS. This would correspond to ≤125 km of displacement and a shear rate of ≤7 mm/yr on the STDS, assuming a regular dip of 10° and simple shear in the STDsz. During the same time span, units within the Ama Drime horst experienced the largest exhumation (1.0 to 1.5 GPa, 37 to 56 km) corresponding to vertical rates of 2 to 3 mm/yr. Such exhumation occurred while HCS rocks, at the exclusion of amphibolite levels, were partially molten following a phase of isobaric heating.

5.3.3 Exhumation mechanisms at the time of STDS activity.

Thrust imbrications, wedge extrusion and post-thickening thermal re-equilibration have been proposed as the main mechanisms for burial, heating and exhumation of HCS rocks. For some, internal deformations within the Himalayan thrust system could explain the STDS geometry (Webb et al., 2007). Other consider a larger thrust wedge system whose shape may vary significantly from one author to the other, being a few tenth of kilometres (Burchfiel & Royden, 1985; Grujic et al., 1996) to more than 120 km long (Guillot & Allemand, 2002). Alternatively other authors consider that HCS rocks have been expulsed from further North, below the Tibetan plateau, through ductile channel flow following crustal melting (Beaumont et al., 2001; Grujic et al., 2002; Jamieson et al., 2004).

In all these models, exhumation of the HCS occurs coevally with normal motion along the STDS, but amount of motion on the STDS vary widely. In the thrust system hypothesis, motion on the STDS can be very small (≤30 km) and is localized in a narrow shear zone (Webb et al., 2007). At the opposite, STDS amount of motion is much larger in the channel flow hypothesis, on the same order of magnitude as motion on the MCT (some hundreds of km), but deformation could be distributed in all the upper half of the channel. Timing and throw estimates of the MCT's and STDS are thus crucial to decipher between the models.

Given its dip to the North, the MCT is probably located only ~20 km below Kharta (Fig. 1c). Age of motion along the MCTl/MCT and MCTu/HHT has been constrained through dating of the metamorphic evolution of the HCS gneisses and migmatites affected by top to the south high temperature thrusting (Hodges et al., 1996; Vance & Harris, 1999; Walker et al., 1999; Foster et al., 2000; Simpson et al., 2000; Johnson et al., 2001; Viskupic & Hodges, 2001; Catlos et al., 2001; 2002a,b; 2004; Kohn et al., 2005; Martin et al., 2007). Ages were obtained by U-(Th)-Pb method on zircon in leucosome and on monazite in leucosome, matrix or as inclusion within garnet (see Kohn et al., 2005 for a review). Ages interpretation has been widely discussed, especially for monazite, (see Catlos et al., 2004 and Kohn et al., 2005 for a review). Based on their Y and Th content and textural relationships, monazite age has been either associated with leucosome crystallisation or crystal formation during garnet growth, this latter mostly occurring during temperature increase (prograde evolution). Considering the various published ages it appears that temperature increase of the HCS gneisses occurred between ~40 and 16 Ma and that crystallisation of melt produced during this temperature increase occurred between 18 and 10 Ma (Hodges et al., 1996; Walker et al., 1999; Foster et al., 2000; Simpson et al., 2000; Johnson et al., 2001; Viskupic & Hodges, 2001; Catlos et al., 2001; 2002a,b; 2004; Kohn et al., 2005; Martin et al., 2007). Coupling these dating with the PT evolution of the HCS gneisses and migmatites places some constraints on the age of their exhumation and thus on the extrusion between the MCTl and or MCTu and the STDS. The PT evolution is characterized by a strong decompression starting at ~1 GPa (Vance & Mahar, 1998; Guillot et al., 1999; Searle et al., 1999, Vannay et al., 1999; Goscombe & Hand, 2000; Kohn et al., 2001; Borghi et al., 2003; Dasgupta et al., 2004; Harris et al., 2004). During this event the rocks keep heating as the thickened Indian continental crust has not yet reached thermal equilibrium and exhumation rate are slow enough (Thompson & Connolly, 1995). Consequently, monazite crystallization might still occur during exhumation, especially if the muscovite-dehydration melting reaction is reached which is the case during decompression and heating for the migmatitic samples (Guillot et al., 1999; Searle et al., 1999, Goscombe & Hand, 2000; Borghi et al., 2003; Dasgupta et al., 2004; Harris et al., 2004). Actually, petrogenetic modelling by Harris et al. (2004) evidences that significant garnet crystallization occurred when this reaction was reached. Thus, the ages of the prograde monazites are an upper bound for the exhumation of the HCS i.e. between 40 and 16 Ma. Coupling the age of the prograde evolution and of the melt crystallisation gives an interval for the age of melting. Detailed study by Kohn et al. (2005) in Central Nepal (Langtang area) suggests that this event took place at 20+/-2 Ma for the northern part of the HCS, between the STDS and the Langtang thrust, the possible westward prolongation of the Barun thrust (HHT/MCTu), and at 15+/-2 Ma for the southern part, between the MCTu and the MCTl. Similar age pattern was also evidenced by Catlos et al. (2004) in NE India (Sikkim). Altogether this suggests that the MCTu was active at and before 20+/-2 Ma and the MCTl at and before 15+/-2 Ma. Consequently, MCTl and MCTu are most probably active during the adiabadic decompression event recorded by the Ama Drime rocks (see 5.2) as well as during STDS activity.

Cessation of top to the south thrusting within the HCS gneisses and migmatites and of significant motion along MCTl and MCTu is indirectly constrained by the age of the top to the south thrusting in the Lesser Himalaya Unit, below the MCTl, associated with MBT activation. This shift is supposed to occur around 8-12 Ma (Harrison et al., 1997; Catlos et al., 2001, 2002a,b; Daniel et al., 2003; DeCelles et al., 2001; Kohn et al., 2004) coevally with MBT activation at ~11 Ma (Meigs et al., 1995). This southward migration of deformation localization is also supported by the detrital record in the Nepalese Siwalik, suggesting a change of sediment provenance indicating erosion of the Lesser Himalayan at ~10-12 Ma (Szulc et al., 2006). Thus, the cessation of thrusting along MCTl seems to be coeval with the end of most of the STDS deformation. Note that possible Pliocene reactivation of the MCTl in Central Nepal was proposed by Macfarlane (1993) and Catlos et al. (2001).

Throw on the MCTl in Nepal has been estimated to be between 140 and 210 km (Schelling and Arita, 1991; Schelling, 1992) or 200km (Hauck et al., 1998). More recently DeCelles et al. (2001) have raised this estimate to ~500 km. Our estimate of the offset on the STDS of only ≤125 km appears significantly lower than thrusting on the MCTl, even when neglecting possible thrusting on the MCTu. This implies that either the whole HCS does not exhumed as a single coherent bloc or as proposed by Webb et al. (2007) that both the HCS and the Tethyan Serie are transported southward over the MCT.

Numerical models of channel flow in the Himalayan orogeny show that rocks initially buried at depth less than 1.35 GPa can be brought to the surface above the MCTl (Jamieson et al., 2004). This depth, that corresponds to the base of the horizontal ductile channel below Tibet, is broadly compatible with the metamorphic grade of the HCS near the MCTl, and thus appear to confirm the model (Jamieson et al., 2004). However, because the channel flattens to the north and is horizontal below Tibet, there is no reason to expect exhumation of deeper rock anywhere within the channel. Late exhumation in the Ama Drime horst has brought to the surface rocks that were at 15 km depth at the end of motion on the STDS (see 5.3.3 below). This gives us access to the deep part of wedge / channel ~140 km north of the emergence of the MCTl (Fig. 1c). The Ama Drime orthogneissic unit has been buried to depth ≥52 km (≥ 1.4 GPa) and exhumed more than 1 GPa (37 km) below the STDS, while the overlying Ama Drime paragneissic unit has been buried to 1.6GPa (60km). Such depths would thus correspond to rocks from below the channel (i.e. below the MCTl). This would imply that most of the HCS rocks do not correspond to the channel and that the MCT1 and the whole channel would now be exposed above T5D33 locality, thus north of the Sangkar Ri. This corresponds to a maximum thickness of the channel of only 1.3 to 4km (15km distance for 10±5° dip) (Fig. 2a). Furthermore, as most of the exhumation (37 to 48 km) took place between the MCTl and STDS, that thus did not bound a horizontal channel at that time. It also appears that, even it has been largely migmatised, the Ama Drime orthogneissic unit represents a coherent unit as metabasite layers can be followed without interruption for distances of few kilometres (Fig. 3be). The large-scale folds affecting these layers are more compatible with vertical thinning and/or N-S simple shear rather than with a partially molten medium that would have flowed for some hundreds of kilometres.

It is logical that rocks sampled deeper in a given thrust slice have experienced higher pressure conditions. In that case the maximum possible pressure corresponds to the minimum rooting depth of the thrust system, or thrust wedge, and the horizontal pressure gradient in a given thrust sheet may be used to evaluate the dipping angle of the underlying thrust system. In the case of the Ama Drime, this would imply that the MCT / MHT system roots at more than 52 – 63 km depth and dips 6 – 9° to the north, which is in good accordance with the value proposed from geophysical evidences (e.g., Makovsky et al., 1996).

5.3.4 Final exhumation of the Ama Drime horst.

As previously discussed, deformation started prior to ~11 Ma in the Dinggye shear zone (age of T5D5 cross-cutting dyke, see 4.2.1 and 5.2). The ~0.4 GPa of exhumation (15 km) of the Ama Drime unit orthogneissic unit that occurred during the last ~12 Ma are thus related to ductile and brittle motion along the N-S Kharta and Dinggye shear zones and the formation of the Ama Drime horst (Fig. 5b). This estimate suggests an average exhumation rate of ~1.2 mm/yr. The vertical offset of the STD is of 4.4 to 9.4 km at the northern tip of the Ama Drime (see 3.2.1) (Fig. 2a). This is coherent with a progressive decrease of the finite motion towards the northern tip of the Dinggye fault. 15 km of exhumation could have been sufficient to bring the HHT/MCTu at the surface, confirming that the Nyonno Ri Boundary could be an equivalent of the Barun thrust that separates the LHCS and the GHCS.

(U-Th)/He apatite ages collected at various locations within the horst (this study; Jessup et al., 2008) appear to give a coherent picture corresponding to vertical exhumation at about 1 mm/yr since at least 4.2 Ma (see 4.2.4, Fig. 10). This corresponds to ~4 km of vertical exhumation. All (U-Th)/He data fit in the same trend suggesting that there is no differential exhumation across the horst. The straightforward interpretation is that the two active faults bounding the horst are active since at least 4.2 Ma with vertical slip rates of ~1 mm/yr.

Both active faults exhibit ductile shear zones in their footwall. The fact that the motion direction on the ductile mylonites and brittle faults are the same (Fig. 4) favours the interpretation of one continuous phase of deformation, as it is classically interpreted in metamorphic core complexes. In that case, initial exhumation related to ductile deformation would have started at a fast rate of at least 1.4 mm/yr and would have slowed down to ~1 mm/yr in the last 4 Ma in order to reach an average rate of ~1.2 mm/yr.

Total exhumation of ~15 km would correspond to ~21 km displacement on the Dinggye shear zone (dip ~45°), and ~30 km on the Kharta one (dip ~30°). This implies that 41 km (measured horizontally, parallel to the motion direction) of the hanging plates would have been eroded. Following the interpretation that part of the Ama Drime orthogneissic unit adiabatic decompression is contemporaneous with E-W extension, and not with the STDS, would increase the vertical exhumation to 24±2 km (Cottle et al., 2009). The amount of removed upper plate would thus rise to 60 to 71 km. Such estimates are problematic as the two faults are only 28 km away from each other, leaving place for a maximum 28 km of removed upper plate. In order to stay compatible with 15 km of exhumation both faults should dip by 47 to 52°, and join at the surface at the onset of deformation. Conversely, maximum possible exhumations for faults dipping 30° and 45° are respectively 14 km and 8 km. It thus appears that the structural history of the Ama Drime horst is more complicated, either that the fault have not been synchronous and / or that their dip was significantly larger than the present dip of the mylonites.

Ductile deformation in the Dinggye shear zone started prior to ~11 Ma and stopped at ~10 Ma, as temperature had dropped below ~300°C according to the biotite and muscovite argon ages (Fig. 9). The age of the Kharta shear zone is much less well constrained. The fact that all leucocratic dykes are deformed in the Kharta sz while many of them cross-cut the Dinggye sz (Fig. 2b) could suggest that ductile deformation initiate later, or lasted longer, on the western side than on the eastern one. Such dykes are dated between 12.8±0.2 and 9.8±1.2 Ma (Fig. 9), suggesting that the main ductile deformation event could have occurred prior to ~10 Ma in the Dinggye sz and after that date in the Kartha sz. On the other hand, ~12 Ma muscovite and ~10 Ma biotite $^{39}Ar/^{40}Ar$ ages could suggest that ductile deformation was active in the Kharta shear zone in the 12-10 Ma interval coevally with the Dinggye sz. However $^{39}Ar/^{40}Ar$ ages in the Kharta sz span between 24 and 3 Ma (Table 3, Fig. 9) and another interpretation can be proposed. T7A19 meta-arenite biotite $^{39}Ar/^{40}Ar$ age (23.5±0.5 Ma) is interpreted as inherited from the peak temperature metamorphism in the Ama Drime series (see 4.2.2). When plotted against elevation, the other $^{39}Ar/^{40}Ar$ biotite argon ages suggest a slow exhumation rate in the Kharta shear zone from ~10 to ~6 Ma (Fig. 11). The same plot for the Dinggye shear zone confirms fast exhumation at ~10.5 Ma. (Fig. 11). Together with the (U-Th)/He data, this could imply two pulses of rapid cooling / exhumation for the Ama Drime horst: one at ~10 Ma and another since ~4 Ma. In that case the biotite ages of the western flank would be interpreted as cooling ages and the muscovite ages as reflecting deformation phases at ~12 Ma and since ~6 Ma (Fig. 9). In the Dinggye sz the $^{39}Ar/^{40}Ar$ biotite and muscovite ages are the same (Fig. 9) suggesting a major cooling / deformation phase between 13.7 and 10.2 Ma.

We propose that two successive normal faulting events took place in the Ama Drime massif. At ~12 Ma, E-W extension immediately following the end of motion on the STDS induced the formation of the Dinggye shear zone and induced rapid cooling and exhumation (~4 mm/yr) on the eastern side of the range (Fig. 12b). Exhumation (and cooling) was probably slower on the western side resulting in a more complex thermochronologic signal. This could indicate that the master fault was on the eastern side, a fact that could explain the bulge of the STD observed to the NW of the Ama Drime. By

~10 Ma temperature was below 300°C in the Dinggye shear zone. That deformation phase ended ~9 Ma ago, and induced 11 to 13 km of exhumation. Prior to 4 Ma ago, probably at ~6 Ma, two conjugate N-S normal faults affected the Ama Drime range, inducing exhumation at a rate of ~1 mm/yr, for a total of at least 4 km (Fig. 12c). Hydrothermal circulation along brittle faults induced the crystallisation of a second generation of muscovites near the Kharta fault (Fig. 9). The late normal faults belong to the Xainza-Dinggye fault system and are contemporaneous with the major east-west extensional episode recognized in numerous localities in southern Tibet (e.g. Mahéo et al. [2007] for a review). This structural history, compatible with presently available data would need to be tested at the light of new data.

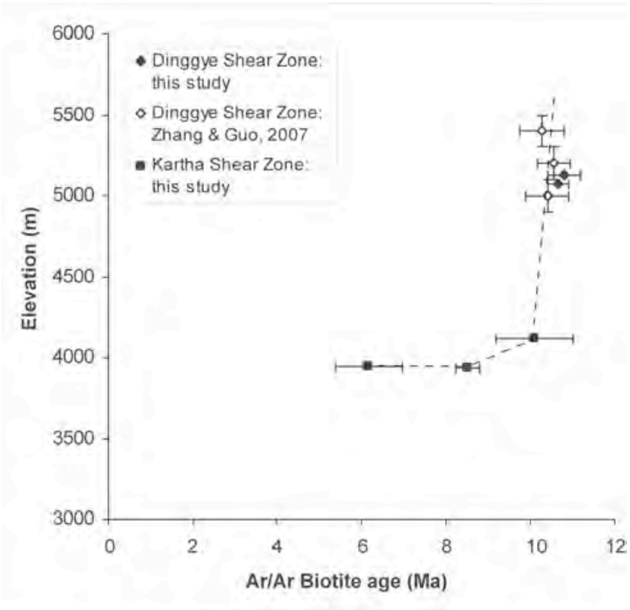

Fig. 11: Plot of Ama Drime Ar/Ar biotite age versus elevation.
Data from this study (Table 3), and Zhang & Guo (2007) (Table DR10). Elevation of Zhang & Guo (2007) samples has been inferred from SRTM digital elevation model and was attributed a conservative 1σ uncertainty of 100 m. This plot suggests that exhumation rate was very fast at ~ 10 Ma and then significantly slowed down at least until 6 Ma. See text for details

In any case the onset of E-W extension appears to closely follow or to be contemporaneous with the time of the end of motion along the STDS and MCTl between 12 and 10 Ma. This brutal transition from N-S to E-W extension in south Tibet while ~N-S convergence still takes place between India and Eurasia has to be explained.

In a context of ~N-S shortening, north south trending normal faults can be related (1) with east-west extension during orogen parallel mid-crustal flow (Cottle et al., 2009), (2) stress reorganization(s) related with kinematics and /or geometry change(s) of the underlying thrust system and (3) focussed erosion of the Arun River (Jessup et al., 2008).

Focussed erosion of the Arun River can be ruled out as the river is not centred on the massif, where the deepest rocks outcrop, but flows in the half graben located along the western flank of the massif. Possible recent migration of the river from the core of the horst to it present day location, is unlikely as (1) focused erosion implies deep incision incompatible with significant river migration, and (2) (U-Th)/He data indicates constant exhumation with no significant tilting since at leat 4 Ma.

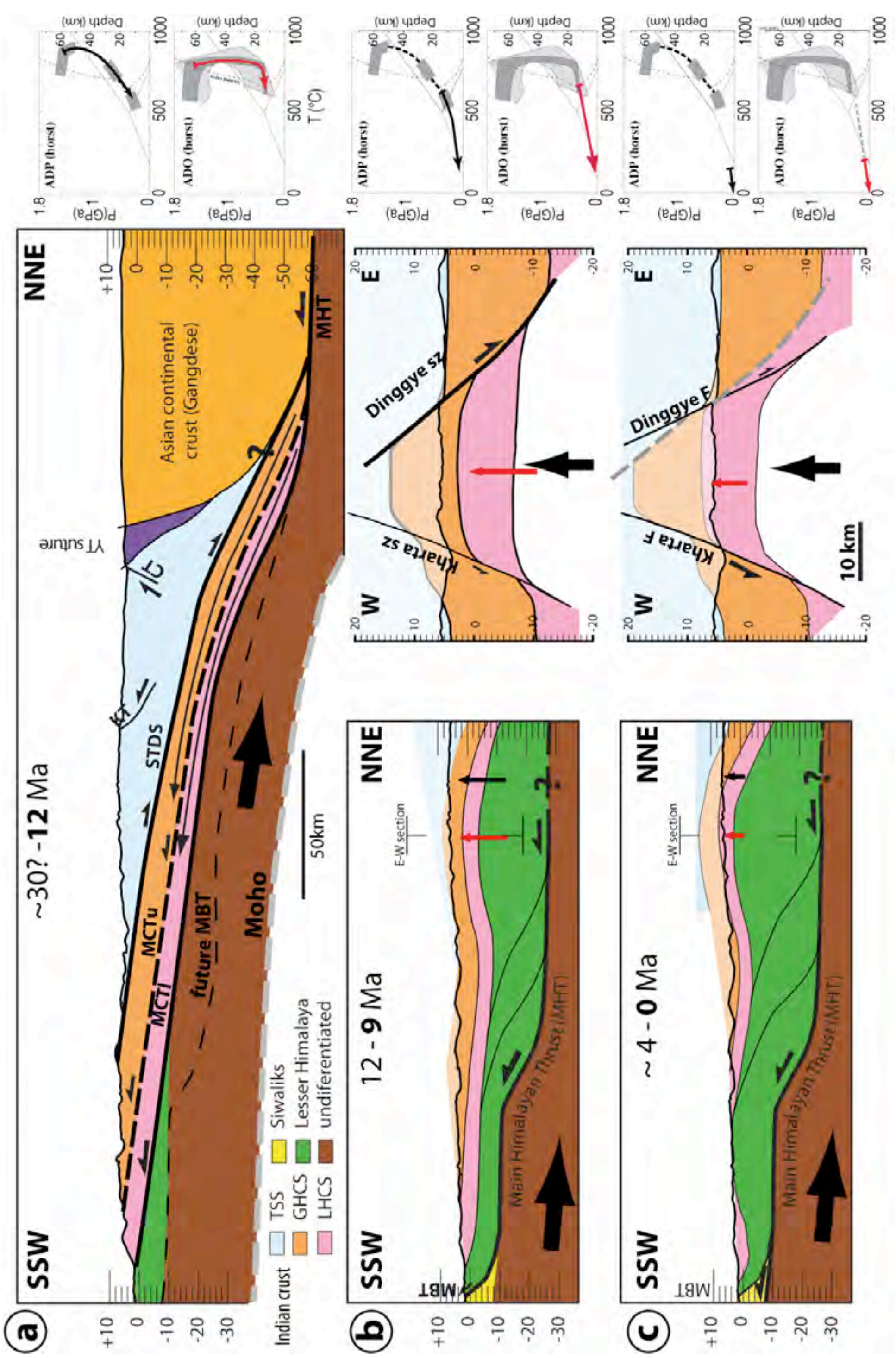

Fig. 12 : Speculative sketches of exhumation phases of the Ama Drime rocks.

Schematic drawings depicting the main exhumation phases of the Ama Drime rocks. The burial stage (prograde metamorphism) is not depicted. Drawings have been oversimplified in order to highlight structures related to the exhumation of the AmaDrime. The topographic profiles are arbitrary for sketches a and b and based on SRTM data for sketch c. Shaded color above topography. ADO, Ama Drime orthogneissic unit; ADP, Ama Drime paragneissic unit.

a) to c) *Main exhumation stages, with cross section(s) (left) and corresponding P-T path for the Ama Drime Pragneisses (upper right) and orthogneisses (lower right). For b) and c) two cross sections are presented: NNE-SSW parallel to Fig.2b but going through Ama Drime range (left) and East-West across the South Ama Drime (Center). In each case the arrow correspond to the path during the whole time interval.* ***a)*** *Exhumation in the hanging wall of the lower MCT/MCT and in the footwall of the STDS, between ~33 and 12 Ma. This is the main exhumation phase during which both units are partially melted. Timing of exhumation initiation is not precisely constrained. The upper MCT/HHT is probably active only during a limited time. KT: Kangmar thrust, CT: counterthrust* ***b)*** *Exhumation in the footwall of the Kharta and Dinggye shear zones. The Dinggye shear zone was probably the master fault and is figured in bold* ***c)*** *Exhumation in the footwall of the Kharta and Dinggye faults*

The exact distribution of the early (12-10 Ma) phases of E-W extension is not yet well recognized. It starts to be documented in few localities through Tibet: in the Thakkhola graben (Garzione et al., 2003), in Tangra Yum Co (Dewane et al., 2006), Lopu fault (Arnaud et al., 2008) as well as in the Xainza Rift (Hager et al., 2006) in the northern prolongation of the Dinggye fault. In all these localities the exhumation seems to last less than 2 Ma (ibid.). Some have proposed that, at the scale of Tibet, crustal-flow towards the South (Himalaya) was followed by crustal flow toward the East (LongmenShan and Yunnan) that would still be active today (e.g., Royden et al., 1997). In that context, the switch from N-S to E-W extension in the Ama Drime would correspond to the change in direction of the channel flow (Cottle et al., 2009). However, the reason(s) for such radical change, and for the occurrence of two distinct phases of extension rather than a continuous one, would stay mysterious as the main boundary conditions driving channel flow (thermal state of the crust beneath Tibet and topography) do not appear to have radically changed at that time. Furthermore the direction of extension in the Ama Drime area is neither perpendicular to the regional high topography nor directed towards the region where crustal flow is expected to leave Tibet north of the eastern syntaxis.

On the other hand the timing of the end of motion along the MCTl appears closely related to the activation of the Main Boundary Thrust (Fig. 12a, b). This corresponds to the propagation of surface expression of the deep main Himalayan thrust (MHT) towards the external part or the accretionary prism, as it is classically observed in many mountain belts. From plates kinematics recontruction based on magnetic anomalies, Lee and Lawyer (1995) infer a change in India-Eurasia convergence direction from ~N30 to ~N13 at 10-12 Ma together with a slight increase in rate. Using a different plate circuit Molnar and Stock (2009) infer a ≥ 40% rate decrease together with a direction change between 20 and ~10 Ma. From their data, the change may have occurred gradually or abruptly near 11Ma. The timing coincidence suggest that changes in the locus, direction and rate of thrusting at ~11Ma may have annihilate the conditions favourable for slip of a passive roof fault (The STDS) along the top of the prism, and locally promoted ~E-W extension. We also note that the Molnar and Stock (2009) plate reconstruction shows a constant convergence rate since ~10 Ma, but a marqued change in direction between ~5 and ~6Ma ago, at the time that we infer for the initiation of the still active E-W extension phase that has been interpreted as directly related to India punch (Armijo et al., 1986; McCaffrey & Nabelek, 1998; Kapp and Guynn, 2004). We thus propose that south Tibet Cenozoic extension phases kinematics are foundamentaly drived by the direction and rate of India underthrusting.

5.5 Conclusion / summary:

From the observations and interpretations presented above the structural and metamorphic evolution of the Ama Drime range can be summarized as follows. In the Ama Drime range, both the Ama Drime orthogneissic and Paragneissic unit where buried to depth of 52 to 63 km. Most of the exhumation corresponds to an adiabatic decompression of 37 to 48 km, initiate after 33 Ma, between the MCT's and the STDS until ~13.5 Ma (Fig. 12a). That phase ended when motion along the STDS switched to local E-W extension between 13.5 and 12 Ma. This timing is compatible with a contemporaneous end of the STDS and the MCTl motion at ~12 Ma. Vertical exhumation across the STDsz and the STD is smaller than 0.6 GPa (22 km), corresponding to ~125 km of displacement and a rate of ~7 mm/yr on the STDS between ~30 and ~12 Ma. During the same time span, further 0.3 to 0.7 GPa (11 to 26 km) of exhumation occurred below the STDsz probably above the MCTl. The coeval end of motion on the STDS and MCTl, and the fact that the HCS rocks were partially molten at the time of their exhumation appear compatible with the lower crustal flow hypothesis. However, the fact that motion on the STDS is much smaller than on the MCTl and that rocks have been exhumed from greater depths than those envisaged for the channel model are more compatible with a wedge extrusion or thrust system model. In that case, the change of direction of extension at the top of the belt was triggered by propagation of thrusting from the MCTl to the lower/more external MBT. Whilst exhumation may have been continuous since ~12 Ma, some clues suggest that it took place in two distinct phases. (1) The N-Dinggye normal shear zone was active until ~9 Ma, accounting for 9 to 12 km of exhumation (Fig. 12b). (2) final exhumation of the Ama Drime horst along the Dinggye and Kharta normal faults from ~6 to 4 Ma to present at a rate of ~1 mm/yr (Fig. 12c). The fact that the Arun River flows outside of the Ama Drime horst excludes that it may have played a major role in the exhumation of the range.

acknowledgments

We thank E. Deloule and the ion probe team of the CRPG, CNRS UPR 2300, Nancy, France for their help in dating the zircons. Claude Merlet and the electronic microprobe team of Géosciences Montpellier, Université de Montpellier 2, France. We thank Paul Capiez for the whole rock X-fluorence analysis at UMR 5570, Lyon, France. This paper benefited for constructive review by C. Groppo and one anonymous reviewer. The first field trip was financed by INSU DyETI grant to R. Lacassin and P.H.L. This project has benifited from the sino-french PRA program to D.L. and J.V.

References

Arita, K. (1983), Origin of the Inverted Metamorphism of the Lower Himalayas, Central Nepal, *Tectonophysics*, *95*, 43-60.

Armijo, R., P. Tapponnier, J. L. Mercier, and T. L. Han (1986), Quaternary Extension in Southern Tibet - Field Observations and Tectonic Implications, *J. Geophys. Res.*, *91*, 13803-13872.

Arnaud, N., J. C. Aitchison, P. H. Leloup, F. Valli, and S. Wilde (2008), Constraints on the initiation of normal faulting across the Yarlung Tsangpo suture zone, from the Lopu Gangri range, southern Tibet, *Geophys. Res. Abstracts*, *10*, EGU2008-A-00000.

Auzanneau, E., D. Vielzeuf, and M. W. Schmidt (2006), Experimental evidence of decompression melting during exhumation of subducted continental crust, *Contrib. Mineral. Petrol.*, *152*, 125-148.

Baur, J. R. (2007), Seismotectonics of the Himalayas and the Tibetan Plateau: moment tensor analysis of regional seismograms, phD thesis, 298 pp, Oregon State University, Corvallis.

Beaumont, C., R. A. Jamieson, M. H. Nguyen, and B. Lee (2001), Himalayan tectonics explained by extrusion of a low-viscosity crustal channel coupled to focused surface denudation, *Nature*, *414*, 738-742.

Bollinger, L., J. P. Avouac, O. Beyssac, E. J. Catlos, T. M. Harrison, M. Grove, B. Goffe, and S. Sapkota (2004), Thermal structure and exhumation history of the Lesser Himalaya in central Nepal, *Tectonics*, *23*, TC5015, doi:5010.1029/2003TC001564.

Bordet, P. (1961), *Recherches géologiques dans l'Himalaya du Népal, région du Makalu*, 275 pp., CNRS, Paris.

Borghi, A., D. Castelli, B. Lombardo, and D. Visona (2003), Thermal and baric evolution of garnet granulites from the Kharta region of S Tibet, E Himalaya, *Eur. J. Mineral.*, *15*, 401-418.

Brunel, M. (1983), Etude pétro-structurale des chevauchements ductiles en Himalaya (Népal oriental et Himalaya du Nord–Ouest), 395 pp, University of Paris VII, Paris.

Burchfiel, B. C., and L. H. Royden (1985), North-South Extension within the Convergent Himalayan Region, *Geology*, *13*, 679-682.

Burchfiel, B. C., C. Zhilang, K. V. Hodges, L. Yuping, L. H. Royden, D. Changrong, and X. Jiene (1992), *The South Tibetan detachment System, Himalayan Orogen: Extension Contemporaneous with and Parallel to Shortening in a Collisional Mountain Belt.*, 41 pp., Geological Society of America.

Burg, J. P., M. Brunel, D. Gapais, G. M. Chen, and G. H. Liu (1984), Deformation of Leucogranites of the Crystalline Main Central Sheet in Southern Tibet (China), *J. Struct. Geol.*, *6*, 535-&.

Carosi, R., B. Lombardo, G. Molli, G. Musumeci, and P. C. Pertusati (1998), The south Tibetan detachment system in the Rongbuk valley, Everest region. Deformation features and geological implications, *J. Asian. Earth Sci.*, *16*, 299-311.

Castro, A., L. G. Corretge, M. El-Biad, H. El-Hmidi, C. Fernandez, and A. E. P. Douce (2000), Experimental constraints on hercynian anatexis in the Iberian Massif, Spain, *J. Petrol.*, *41*, 1471-1488.

Catlos, E. J., C. S. Dubey, T. M. Harrison, and M. A. Edwards (2004), Late Miocene movement within the Himalayan Main Central Thrust shear zone, Sikkim, north-east India, *J. Metamorph. Geol.*, *22*, 207-226.

Catlos, E. J., L. D. Gilley, and T. M. Harrison (2002a), Interpretation of monazite ages obtained via in situ analysis, *Chem.Geol.*, *188*, 193-215.

Catlos, E. J., T. M. Harrison, M. J. Kohn, M. Grove, F. J. Ryerson, C. E. Manning, and B. N. Upreti (2001), Geochronologic and thermobarometric constraints on the evolution of the Main Central Thrust, central Nepal Himalaya, *J. Geophys. Res.*, *106*, 16177-16204.

Catlos, E. J., T. M. Harrison, C. E. Manning, M. Grove, S. M. Rai, M. S. Hubbard, and B. N. Upreti (2002b), Records of the evolution of the Himalayan orogen from in situ Th-Pb ion microprobe dating of monazite: Eastern Nepal and western Garhwal, *J. Asian. Earth Sci.*, *20*, 459-479.

Cattin, R., and J. P. Avouac (2000), Modeling mountain building and the seismic cycle in the Himalaya of Nepal, *J. Geophys. Res.*, *105*, 13389-13407.

Connolly, J. A. D. (1990), Multivariable Phase-Diagrams - an Algorithm Based on Generalized Thermodynamics, *Am. J. Sci.*, *290*, 666-718.

Cottle, J. M., M. J. Jessup, D. L. Newell, M. S. A. Horstwood, S. R. Noble, R. R. Parrish, D. J. Waters, and M. P. Searle (2009), Geochronology of granulitized eclogite from the Ama Drime Massif: Implications for the tectonic evolution of the South Tibetan Himalaya, *Tectonics*, *28*, DOI: 10.1029/2008TC002256.

Cottle, J. M., M. J. Jessup, D. L. Newell, M. P. Searle, R. D. Law, and M. S. A. Horstwood (2007), Structural insights into the early stages of exhumation along an orogen-scale detachment: The South Tibetan Detachment system, Dzakaa Chu section, eastern Himalaya, *J. Struct. Geol.*, *29*, 1781-1797.

Daniel, C. G., L. S. Hollister, R. R. Parrish, and D. Grujic (2003), Exhumation of the Main Central Thrust from lower crustal depths, Eastern Bhutan Himalaya, *J. Metamorph. Geol.*, *21*, 317-334.

Dasgupta, S., J. Ganguly, and S. Neogi (2004), Inverted metamorphic sequence in the Sikkim Himalayas: crystallization history, P-T gradient and implications, *J. Metamorph. Geol.*, *22*, 395-412.

DeCelles, P. G., D. M. Robinson, J. Quade, T. P. Ojha, C. N. Garzione, P. Copeland, and B. N. Upreti (2001), Stratigraphy, structure, and tectonic evolution of the Himalayan fold-thrust belt in western Nepal, *Tectonics*, *20*, 487-509.

Dewane, T. J., D. F. Stockli, C. Hager, M. Taylor, L. Ding, J. Lee, and S. Wallis (2006), Timing of Cenozoic E-W Extension in the Tangra Yum Co-Kung Co Rift, south-central Tibet, *AGU fall Metting*.

Dewey, J.F. (1988), extensional collapse of orogens, *Tectonics*, *7*, 683-692.

Edwards, M. A., W. S. F. Kidd, J. X. Li, Y. J. Yu, and M. Clark (1996), Multi-stage development of the southern Tibet detachment system near Khula Kangri. New data from Gonto La, *Tectonophysics*, *260*, 1-19.

England, P., and G. Houseman (1989), Extension during Continental Convergence, with Application to the Tibetan Plateau, *J. Geophys. Res.*, *94*, 17561-17579.

Foster, G., P. Kinny, D. Vance, C. Prince, and N. Harris (2000), The significance of monazite U-Th-Pb age data in metamorphic assemblages; a combined study of monazite and garnet chronometry, *Earth Planet. Sci. Lett.*, *181*, 327-340.

Fraser, G., D. Ellis, and S. Eggins (1997), Zirconium abundance in granulite-facies minerals, with implications for zircon geochronology in high-grade rocks, *Geology*, *25*, 607-610.

Garzione, C. N., P. G. DeCelles, D. G. Hodkinson, T. P. Ojha, and B. N. Upreti (2003), East-west extension and Miocene environmental change in the southern Tibetan plateau: Thakkhola graben, central Nepal, *Geol. Soc. Am. Bull.*, *115*, 3-20.

Goscombe, B., D. Gray, and M. Hand (2006), Crustal architecture of the Himalayan metamorphic front in eastern Nepal, *Gond. Res.*, *10*, 232-255.

Goscombe, B., and M. Hand (2000), Contrasting P-T paths in the Eastern Himalaya, Nepal: Inverted isograds in a paired metamorphic mountain belt, *J. Petrol.*, *41*, 1673-1719.

Groppo, C., B. Lombardo, F. Rolfo, and P. Pertusati (2007), Clockwise exhumation path of granulitized eclogites from the Ama Drime range (Eastern Himalayas), *J. Metamorph. Geol.*, *25*, 51-75.

Grujic, D., M. Casey, C. Davidson, L. S. Hollister, R. Kundig, T. Pavlis, and S. Schmid (1996), Ductile extrusion of the Higher Himalayan Crystalline in Bhutan: Evidence from quartz microfabrics, *Tectonophysics*, *260*, 21-43.

Grujic, D., L. S. Hollister, and R. R. Parrish (2002), Himalayan metamorphic sequence as an orogenic channel: insight from Bhutan, *Earth Planet. Sci. Lett.*, *198*, 177-191.

Guillot, S. (1999), An overview of the metamorphic evolution in Central Nepal, *J. Asian. Earth Sci.*, *17*, 713-725.

Guillot, S., and P. Allemand (2002), Two-dimensional thermal modelling of the early tectonometamorphic evolution in central Himalaya, *J. Geodyn.*, *34*, 77-98.

Hager, C., D. Stockli, T. Dewane, and L. Ding (2006), Episodic Mio-Pliocene rifting in south-central Tibet. Thermochronometric constraints from the Xainza rift, *AGU fall Metting*.

Harris, N. B. W., M. Caddick, J. Kosler, S. Goswami, D. Vance, and A. G. Tindle (2004), The pressure-temperature-time path of migmatites from the Sikkim Himalaya, *J. Metamorph. Geol.*, *22*, 249-264.

Harrison, T. M., P. Copeland, W. S. F. Kidd, and O. M. Lovera (1995), Activation of the Nyainqentanghla Shear Zone - Implications for Uplift of the Southern Tibetan Plateau, *Tectonics*, *14*, 658-676.

Harrison, T. M., M. Grove, O. M. Lovera, and E. J. Catlos (1998), A model for the origin of Himalayan anatexis and inverted metamorphism, *J. Geophys. Res.*, *103*, 27017-27032.

Harrison, T. M., F. J. Ryerson, P. LeFort, A. Yin, O. M. Lovera, and E. J. Catlos (1997), A Late Miocene-Pliocene origin for the Central Himalayan inverted metamorphism, *Earth Planet. Sci. Lett.*, *146*, E1-E7.

Hauck, M. L., K. D. Nelson, L. D. Brown, W. J. Zhao, and A. R. Ross (1998), Crustal structure of the Himalayan orogen at similar to 90 degrees east longitude from Project INDEPTH deep reflection profiles, *Tectonics*, *17*, 481-500.

Heim, A., and A. Gansser (1939), Central Himalaya: geological 999 obervations of the Swiss expedition 1936, *Mem. Soc. Helv. Sci. Nat.*, 1-245.

Hodges, K. V. (2000), Tectonics of the Himalaya and southern Tibet from two perspectives, *Geol. Soc. Am. Bull.*, *112*, 324-350.

Hodges, K. V., W. E. Hames, W. Olszewski, B. C. Burchfiel, L. H. Royden, and Z. Chen (1994), Thermobarometric and Ar-40 Ar-39 Geochronological Constraints on Eohimalayan Metamorphism in the Dinggye Area, Southern Tibet, *Contrib. Mineral. Petrol.*, *117*, 151-163.

Hodges, K. V., R. R. Parrish, and M. P. Searle (1996), Tectonic evolution of the central Annapurna Range, Nepalese Himalayas, *Tectonics*, *15*, 1264-1291.

Holland, T. J. B., and R. Powell (1998), An internally consistent thermodynamic data set for phases of petrological interest, *J. Metamorph. Geol.*, *16*, 309-343.

House, M. A., K. A. Farley, and D. Stockli (2000), Helium chronometry of apatite and titanite using Nd-YAG laser heating, *Earth Planet. Sci. Lett.*, *183*, 365-368.

Indares, A., R. W. White, and R. Powell (2008), Phase equilibria modelling of kyanite-bearing anatectic paragneisses from the central Grenville Province, *J. Metamorph. Geol.*, *26*, 815-836.

Jamieson, R. A., C. Beaumont, S. Medvedev, and M. H. Nguyen (2004), Crustal channel flows: 2. Numerical models with implications for metamorphism in the Himalayan-Tibetan orogen, *J. Geophys. Res.*, *109*, DOI: 10.1029/2003JB002811.

Jessup, M. J., D. L. Newell, J. M. Cottle, A. L. Berger, and J. A. Spotila (2008), Orogen-parallel extension and exhumation enhanced by denudation in the trans-Himalayan Arun River gorge, Ama Drime Massif, Tibet-Nepal, *Geology*, *36*, 587-590.

Johnson, M. R. W., G. J. H. Oliver, R. R. Parrish, and S. P. Johnson (2001), Synthrusting metamorphism, cooling, and erosion of the Himalayan Kathmandu Complex, Nepal, *Tectonics*, *20*, 394-415.

Kapp, P., and J. H. Guynn (2004), Indian punch rifts Tibet, *Geology*, *32*, 993-996.

Kapp, P., M. Taylor, D. Stockli, and L. Ding (2008), Development of active low-angle normal fault systems during orogenic collapse: Insight from Tibet, *Geology*, *36*, 7-10.

Kelsey, D. E., C. Clark, and M. Hand (2008), Thermobarometric modelling of zircon and monazite growth in melt-bearing systems: examples using model metapelitic and metapsammitic granulites, *J. Metamorph. Geol.*, *26*, 199-212.

Kohn, M. J., E. J. Catlos, F. J. Ryerson, and T. M. Harrison (2001), Pressure-temperature-time path discontinuity in the Main Central thrust zone, central Nepal, *Geology*, *29*, 571-574.

Kohn, M. J., M. S. Wieland, C. D. Parkinson, and B. N. Upreti (2004), Miocene faulting at plate tectonic velocity in the Himalaya of central Nepal, *Earth Planet. Sci. Lett.*, *228*, 299-310.

Kohn, M. J., M. S. Wieland, C. D. Parkinson, and B. N. Upreti (2005), Five generations of monazite in Langtang gneisses: implications for chronology of the Himalayan metamorphic core, *J. Metamorph. Geol.*, *23*, 399-406.

Le Fort, P. (1975), Himalayas - Collided Range - Present Knowledge of Continental Arc, *Am. J. Sci.*, *A275*, 1-44.

Lee, T. Y., and L. A. Lawver (1995), Cenozoic plate reconstruction of Southeast Asia, *Tectonophysics*, *251*, 85-138.

Leloup, P. H., T. M. Harrison, F. J. Ryerson, W. J. Chen, Q. Li, P. Tapponnier, and R. Lacassin (1993), Structural, Petrological and Thermal Evolution of a Tertiary Ductile Strike-Slip Shear Zone, Diancang Shan, Yunnan, *J. Geophys. Res.*, *98*, 6715-6743.

Leloup, P. H., E. Kali, N. Arnaud, G. Mahéo, E. Boutonnet, L. Xiahan, L. Dunyi, L. Haibing, and J. Liu-Zeng (2009), Miocene (~12 Ma) transition from E-W to N-S syn-convergence normal faulting in the central Himalayas (Ama Drime range), *Geophys. Res. Abstr.*, *11*, EGU2009-9690-2001.
Li, D., Q. Liao, Y. Yuan, Y. Wan, D. Liu, X. Zhang, S. Yi, S. Cao, and D. Xie (2003), SHRIMP U-Pb zircon geochronology of granulites at Rimana (Southern Tibet) in the central segment of Himalayan Orogen, *Chinese Sci. Bull.*, *48*, 2647-2650.
Liu, S. W., J. J. Zhang, G. M. Shu, and Q. G. Li (2005), Mineral chemistry, P-T-t paths and exhumation processes of mafic granulites in Dinggye, Southern Tibet, *Sci. Ch. Ser. D Earth Sci.*, *48*, 1870-1881.
Liu, Y., W. Siebel, H. J. Massonne, and X. C. Xiao (2007), Geochronological and petrological constraints for tectonic evolution of the central Greater Himalayan Sequence in the Kharta area, southern Tibet, *J. Geol.*, *115*, 215-230.
Lombardo, B., P. Pertusati, and A. Borghi (1993), Geology and tectono-magmatic evolution of the eastern Himalaya along the Chomolungma-Makalu transect., in *Himalayan Tectonics*,74, edited by P. J. Treloar and M. P. Searle, pp. 341-355, Geological Society of London, London.
Lombardo, B., and F. Rolfo (2000), Two contrasting eclogite types in the Himalayas: implications for the Himalayan orogeny, *J. Geodyn.*, *30*, 37-60.
Ludwig, K. R. (2003), Isoplot 3.00 a geochronological toolkit for Microsoft Excel, *Berkley Geochronology Center Spec. Pub.*, *4*.
Macfarlane, A. M. (1993), Chronology of Tectonic Events in the Crystalline Core of the Himalaya, Langtang-National-Park, Central Nepal, *Tectonics*, *12*, 1004-1025.
Maheo, G., P. H. Leloup, F. Valli, R. Lacassin, N. Arnaud, J. L. Paquette, A. Fernandez, L. Haibing, K. A. Farley, and P. Tapponnier (2007), Post 4 Ma initiation of normal faulting in southern Tibet. Constraints from the Kung Co half graben, *Earth Planet. Sci. Lett.*, *256*, 233-243.
Makovsky, Y., S. L. Klemperer, L. Y. Huang, and D. Y. Lu (1996), Structural elements of the southern Tethyan Himalaya crust from wide-angle seismic data, *Tectonics*, *15*, 997-1005.
Martin, A. J., G. E. Gehrels, and P. G. DeCelles (2007), The tectonic significance of (U,Th)/Pb ages of monazite inclusions in garnet from the Himalaya of central Nepal, *Chem.Geol.*, *244*, 1-24.
McCaffrey, R., and J. Nabelek (1998), Role of oblique convergence in the active deformation of the Himalayas and southern Tibet Plateau, *Geology*, *26*, 691-694.
Meier, K., and E. Hiltner (1993), Deformation and metamorphism within the Main Central Thrust zone, Arun tectonic Window, eastern Nepal, in *Himalayan Tectonics*,74, edited by P. J. Treloar and M. P. Searle, pp. 511-523, Geological Society of London, London.
Meigs, A. J., D. W. Burbank, and R. A. Beck (1995), Middle-Late Miocene (Greater-Than-10 Ma) Formation of the Main Boundary Thrust in the Western Himalaya, *Geology*, *23*, 423-426.
Molnar, P., and J. Stock (2009), Slowing of India's convergence with Eurasia since 20 Ma and its implications for Tibetan mantle dynamics, *Tectonics*, *28*, 10.1029/2008TC002271.
Molnar, P., and P. Tapponnier (1978), Active Tectonics of Tibet, *J. Geophys. Res.*, *83*, 5361-5373.
Monsalve, G., A. Sheehan, V. Schulte-Pelkum, S. Rajaure, M. R. Pandey, and F. Wu (2006), Seismicity and one-dimensional velocity structure of the Himalayan collision zone: Earthquakes in the crust and upper mantle, *J. Geophys. Res.*, *111*, DOI: 10.1029/2005JB004062.
Murphy, M. A., and T. M. Harrison (1999), Relationship between leucogranites and the Qomolangma detachment in the Rongbuk Valley, south Tibet, *Geology*, *27*, 831-834.
Murphy, M. A., A. Yin, P. Kapp, T. M. Harrison, C. E. Manning, F. J. Ryerson, L. Ding, and J. H. Guo (2002), Structural evolution of the Gurla Mandhata detachment system, southwest Tibet: Implications for the eastward extent of the Karakoram fault system, *Geol. Soc. Am. Bull.*, *114*, 428-447.
Nelson, K. D., W. J. Zhao, L. D. Brown, J. Kuo, J. K. Che, X. W. Liu, S. L. Klemperer, Y. Makovsky, R. Meissner, J. Mechie, R. Kind, F. Wenzel, J. Ni, J. Nabelek, L. S. Chen, H. D. Tan, W. B. Wei, A. G. Jones, J. Booker, M. Unsworth, W. S. F. Kidd, M. Hauck, D. Alsdorf, A. Ross, M. Cogan, C. D. Wu, E. Sandvol, and M. Edwards (1996), Partially molten middle crust beneath southern Tibet: Synthesis of project INDEPTH results, *Science*, *274*, 1684-1688.
Pan, Y., and W. S. F. Kidd (1992), Nyainqentanglha Shear Zone - a Late Miocene Extensional Detachment in the Southern Tibetan Plateau, *Geology*, *20*, 775-778.

Pandey, M. R., R. P. Tandukar, J. P. Avouac, J. Lave, and J. P. Massot (1995), Interseismic Strain Accumulation on the Himalayan Crustal Ramp (Nepal), *Geophys. Res. Lett.*, *22*, 751-754.

Pandey, M. R., R. P. Tandukar, J. P. Avouac, J. Vergne, and T. Heritier (1999), Seismotectonics of the Nepal Himalaya from a local seismic network, *J. Asian. Earth Sci.*, *17*, 703-712.

Patiño-Douce, A. E., and J. S. Beard (1996), Effects of P,f(O-2) and Mg/Fe ratio on dehydration melting of model metagreywackes, *J. Petrol.*, *37*, 999-1024.

Patiño-Douce, A. E., and N. Harris (1998), Experimental constraints on Himalayan anatexis, *J. Petrol.*, *39*, 689-710.

Powell, R., and J. A. Evans (1983), A New Geobarometer for the Assemblage Biotite-Muscovite-Chlorite-Quartz, *J. Metamorph. Geol.*, *1*, 331-336.

Reche, J., and F. J. Martinez (1996), GPT: An Excel spreadsheet for thermobarometric calculations in metapelitic rocks, *Comp. Geosci.*, *22*, 775-784.

Richards, A., T. Argles, N. Harris, R. Parrish, T. Ahmad, F. Darbyshire, and E. Draganits (2005), Himalayan architecture constrained by isotopic tracers from clastic sediments, *Earth Planet. Sci. Lett.*, *236*, 773-796.

Roberts, M. P., and F. Finger (1997), Do U-Pb zircon ages from granulites reflect peak metamorphic conditions? *Geology*, *25*, 319-322.

Robinson, D. M., P. G. DeCelles, P. J. Patchett, and C. N. Garzione (2001), The kinematic evolution of the Nepalese Himalaya interpreted from Nd isotopes, *Earth Planet. Sci. Lett.*, *192*, 507-521.

Rolfo, F., W. McClelland, and B. Lombardo (2005), Geochronological constraints on the age of the eclogite-facies metamorphism in the eastern Himalaya, *Geologie Alpine, memoire h.s. 20th Himalaya-Karakorum-Tibet workshop*, *44*, 170.

Royden, L. H., B. C. Burchfiel, R. W. King, E. Wang, Z. L. Chen, F. Shen, and Y. P. Liu (1997), Surface deformation and lower crustal flow in eastern Tibet, *Science*, *276*, 788-790.

Rubatto, D., I. S. Williams, and I. S. Buick (2001), Zircon and monazite response to prograde metamorphism in the Reynolds Range, central Australia, *Contrib. Mineral. Petrol.*, *140*, 458-468.

Schaltegger, U., C. M. Fanning, D. Gunther, J. C. Maurin, K. Schulmann, and D. Gebauer (1999), Growth, annealing and recrystallization of zircon and preservation of monazite in high-grade metamorphism: conventional and in-situ U-Pb isotope, cathodoluminescence and microchemical evidence, *Contrib. Mineral. Petrol.*, *134*, 186-201.

Schelling, D. (1992), The Tectonostratigraphy and Structure of the Eastern Nepal Himalaya, *Tectonics*, *11*, 925-943.

Schelling, D., and K. Arita (1991), Thrust Tectonics, Crustal Shortening, and the Structure of the Far-Eastern Nepal Himalaya, *Tectonics*, *10*, 851-862.

Schiotte, L., W. Compston, and D. Bridgwater (1989), Ion Probe U-Th-Pb Zircon Dating of Polymetamorphic Orthogneisses from Northern Labrador, Canada, *Can. J. Earth Sci.*, *26*, 1533-1556.

Schulte-Pelkum, V., G. Monsalve, A. Sheehan, M. R. Pandey, S. Sapkota, R. Bilham, and F. Wu (2005), Imaging the Indian subcontinent beneath the Himalaya, *Nature*, *435*, 1222-1225.

Searle, M. P. (2007), Geological map of the Mount Everest – Makalu region Nepal – South Tibet Himalaya scale 1:100 000., Oxford University, Dept. of Earth Sciences.

Searle, M. P., S. R. Noble, A. J. Hurford, and D. C. Rex (1999), Age of crustal melting, emplacement and exhumation history of the Shivling leucogranite, Garhwal Himalaya, *Geol. Mag.*, *136*, 513-525.

Simpson, R. L., R. R. Parrish, M. P. Searle, and D. J. Waters (2000), Two episodes of monazite crystallization during metamorphism and crustal melting in the Everest region of the Nepalese Himalaya, *Geology*, *28*, 403-406.

Szulc, A. G., Y. Najman, H. D. Sinclair, M. Pringle, M. Bickle, H. Chapman, E. Garzanti, S. Ando, P. Huyghe, J. L. Mugnier, T. Ojha, and P. DeCelles (2006), Tectonic evolution of the Himalaya constrained by detrital Ar-40-Ar-39, Sm-Nd and petrographic data from the Siwalik foreland basin succession, SW Nepal, *Basin Res.*, *18*, 375-391.

Tapponnier, P., J. L. Mercier, R. Armijo, T. L. Han, and J. Zhou (1981), Field Evidence for Active Normal Faulting in Tibet, *Nature*, *294*, 410-414.

Tapponnier, P., Z. Q. Xu, F. Roger, B. Meyer, N. Arnaud, G. Wittlinger, and J. S. Yang (2001), Geology - Oblique stepwise rise and growth of the Tibet plateau, *Science*, *294*, 1671-1677.

Thompson, A. B., and J. A. D. Connolly (1995), Melting of the Continental-Crust - Some Thermal and Petrological Constraints on Anatexis in Continental Collision Zones and Other Tectonic Settings, *J. Geophys. Res.*, *100*, 15565-15579.

Vance, D., and N. Harris (1999), Timing of prograde metamorphism in the Zanskar Himalaya, *Geology*, *27*, 395-398.

Vance, D., and E. Mahar (1998), Pressure-temperature paths from P-T pseudosections and zoned garnets: Potential, limitations and examples from the Zanskar Himalaya, NW India, *Contrib. Mineral. Petrol.*, *132*, 225-245.

Vannay, J. C., Z. D. Sharp, and B. Grasemann (1999), Himalayan inverted metamorphism constrained by oxygen isotope thermometry, *Contrib. Mineral. Petrol.*, *137*, 90-101.

Vavra, G., R. Schmid, and D. Gebauer (1999), Internal morphology, habit and U-Th-Pb microanalysis of amphibolite-to-granulite facies zircons: geochronology of the Ivrea Zone (Southern Alps), *Contrib. Mineral. Petrol.*, *134*, 380-404.

Vielzeuf, D., and J. D. Clemens (1992), The Fluid-Absent Melting of Phlogopite Plus Quartz - Experiments and Models, *Am. Min.*, *77*, 1206-1222.

Vielzeuf, D., and J. R. Holloway (1988), Experimental-Determination of the Fluid-Absent Melting Relations in the Pelitic System - Consequences for Crustal Differentiation, *Contrib. Mineral. Petrol.*, *98*, 257-276.

Vielzeuf, D., and J. M. Montel (1994), Partial Melting of Metagreywackes.1. Fluid-Absent Experiments and Phase-Relationships, *Contrib. Mineral. Petrol.*, *117*, 375-393.

Viskupic, K., and K. V. Hodges (2001), Monazite-xenotime thermochronometry: methodology and an example from the Nepalese Himalaya, *Contrib. Mineral. Petrol.*, *141*, 233-247.

Visona, D., and B. Lombardo (2002), Two-mica and tourmaline leucogranites from the Everest-Makalu region (Nepal-Tibet). Himalayan leucogranite genesis by isobaric heating? *Lithos*, *62*, 125-150.

Wager, L. R. (1937), The Arun River Drainage Pattern and the Rise of the Himalaya., *Geol. J.*, *89*, 239-250.

Walker, J. D., M. W. Martin, S. A. Bowring, M. P. Searle, D. J. Waters, and K. V. Hodges (1999), Metamorphism, melting, and extension: Age constraints from the High Himalayan Slab of southeast Zanskar and northwest Lahaul, *J. Geol.*, *107*, 473-495.

Webb, A. A. G., A. Yin, T. M. Harrison, J. Celerier, and W. P. Burgess (2007), The leading edge of the Greater Himalayan Crystalline complex revealed in the NW Indian Himalaya: Implications for the evolution of the Himalayan orogen, *Geology*, *35*, 955-958.

Yin, A. (2000), Mode of Cenozoic east-west extension in Tibet suggesting a common origin of rifts in Asia during the Indo-Asian collision, *J. Geophys. Res.*, *105*, 21745-21759.

Zhang, J. J., and L. Guo (2007), Structure and geochronology of the southern Xainza-Dinggye rift and its relationship to the south Tibetan detachment system, *J. Asian. Earth Sci*., *29*, 722-736

Appendix I: Presure – Temperature path methodology

Whole rock composition of sample T5D39b was obtained from X-fluorescence at the Earth sciences laboratory in Lyon, France (CNRS UMR 5570,University Lyon1 and ENS of Lyon). In weight %, T5D33: SiO_2=73.9; TiO_2=0.8; AL_2O_3=11.7; Fe_2O_3=5.6; MnO=0.05; MgO=1.6; CaO=0.9; Na_2O=0.8; K_2O=3.6, P_2O_5=0.1; LOI (Loss On Ignition)=0.8 / T5D39b: SiO_2=72.3; TiO_2=0.6; AL_2O_3=14.3; Fe_2O_3=4.5; MnO=0.1; MgO=1.2; CaO=1.0; Na_2O=1.7; K_2O=3.2, P_2O_5=0.1; LOI =1.2).

Minerals were analysed with the Cameca SX100 microprobe at the department of Geosciences of Montpellier, France (CNRS UMR 5243). Analyses are reported in Table DR2.

The studied metapelites is described in the NCKFMASMnTi system (Spear, 1993). Perple_X'07 has been used for the calculation of pseudosections using the 2004 revised version of the internally consistent thermodynamic dataset of Holland & Powell (1998). The phases considered in the calculation were: Kyanite, Sillimanite, Andalusite, K-feldspar, Plagioclase, Clinopyroxene, Orthopyroxene, Garnet (Alm, Pyr, Spes, Gros), Ti-Biotite, Phengite, Chlorine, Cloritoid, Cordierite, Amphibole, staurolite and Quartz. Phases and end-members used in the solid-solution models involved in these pseudosections are from Newton et al. (1980) for plagioclase, White et al. (2007) for Ti-biotite, White et al. (2000) for garnet and cloritoid, Holland et al. (1998) for chlorine, Holland & Powell (1998) for phengite and staurolite, Holland & Powell (1996) for clinopyroxen and orthopyroxen, Dale et al. (2000) for amphibole and an ideal solution model for cordierite. Because of the high SiO_2 content, pseudosections were computed considering SiO_2 saturation. The calculation was performed with H_2O saturation.

Appendix II: geochronology

II-1 U-Th/Pb in situ SIMS dating

Zircon and monazite grains were separated using heavy liquids, a Frantz magnetic separator and finally by hand picking under a binocular microscope avoiding the most obvious metamicts or dirty grains. The selected grains were mounted together with standard in epoxy resin. The mounts were then abraded and polished to expose at the surface the middle part of the crystals. G91500 zircon standard (Wiedenbeck et al., 1995) and WB.T.329 (Williams, 1996). monazite standards were used. Zircon and monazite grains were imaged using optical and cathodoluminescence (CL) microscopy. Monazites were analysed with the sensitive high resolution ion microprobes (SHRIMP II) at the Institute of Geology of Beijing, China, while zircons were measured using the Cameca IMS 1270 at CRPG in Nancy, France. Calibration parameters, data acquisition and age correction are described in Compston et al. (1984) for the SHRIMP II, and in Deloule et al. (2001) for the Cameca IMS 1270. The error on the calibration curve is taken into account for the age uncertainty calculation. The spot size was between 30 and 60 μm.

Ion probe U-Th-Pb dating of young minerals is an analytical challenge because of the very small amounts of radiogenic daughter isotopes (^{206}Pb, ^{207}Pb, ^{208}Pb). In case of recent minerals, it is now usual for most geochronologists to consider the $^{238}U/^{206}Pb$ ages as the most reliable for zircons (e.g., [Stern and Amelin, 2003]), and the $^{232}Th/^{208}Pb$ ages for monazites (e.g., [Catlos et al., 2004]). The isotopic systems of zircons and, to a lesser extent, monazites keep the memory of several distinct magmatic, metamorphic and hydrothermal events. This provides the opportunity to reconstruct complex geological histories but requires cautious interpretation of the analytical results to individualize the different populations.

Within a given population of ion probe data, it is important to distinguish meaningful ages from outliers, which can always occur in spite of careful selection of rocks and minerals, and of rigorous analytical conditions. Age disparity around a mean value may results either from (1) an overlap of the probe beam on zones of distinct ages, (2) large SIMS analytical errors related to low radiogenic Pb content in young zircon overgrowths (Stern, 1997), (3) the occurrence of common Pb, (4) ^{230}Th radioactive disequilibrium in monazites (Schärer, 1984), (5) a partial lead loss due to (a) subsequent high temperature event(s), (6) a combination of these points. Consequently, we consider that the best age estimate of a given population of ion probe data is its mathematical mean with a two standard deviation uncertainty, which will lower the influence of outlier(s).

The Tertiary SIMS data are plotted in the Tera-Wasserburg diagram (Tera and Wasserburg, 1972) (1σ error errors for readability) while others data are plotted in concordia diagrams (1σ ellipse errors or larger symbols when ellipses are too small). Errors mentioned in the text are at the 1σ level, the weighted averages, and the associate 95% confidence errors, were calculated with Isoplot 3.23 of Ludwig (2003).

II-2 $^{40}Ar/^{39}Ar$ dating

Minerals were separated using heavy liquids, a Frantz magnetic separator and finally by hand picking under a binocular microscope. The samples were irradiated in two batches during April and December 2007 at the McMaster Nuclear Reactor in the 5C position for 26 h with an approximate 10^{18} neutrons $cm^{-2}s^{-1}$ flux. Irradiation interference on K, Ca and Cl were corrected by irradiating and analyzing KCl and CaF_2 pure salts. J factors were estimated by the use of duplicates of the Fish Canyon sanidine standard with an age of 28.02 Ma (Renne et al., 1998).

The samples were analyzed in Montpellier using the same apparatus and the same protocol, as described in (Arnaud et al., 2003). Samples were loaded in aluminum packets into a double vacuum Staudacher type furnace and step heated; temperature is calibrated by means of a thermocouple. The gas was purified using cold traps with liquid air and Al-Zr getters. Once cleaned, the gas was introduced into a VG3600 mass spectrometer and allowed to equilibrate for 2 min prior to analysis was done statically. Signals were measured by the mean of a Faraday cup with a 10^{11} ohm resistor for ^{40}Ar and ^{39}Ar while ^{39}Ar, ^{38}Ar, ^{37}Ar and ^{36}Ar were analyzed with a photomultiplier after interaction on a Daly plate. Gain between both collectors was estimated by duplicate analysis of ^{39}Ar on both collectors during each analysis, and also by statistical analysis over a period of several years. This gain is 50 and is known at better than 1.5%. This error is included in the age calculation, along with analytical errors on each signal and errors on the blank values. Detailed analytical results are available as electronic supplements. Age plateau given are weighted mean plateaus; the error takes the error on the J factor into account. With the historical decrease of analytical errors, strict plateau criteria (Berger and York, 1981; Dalrymple and Lanphere, 1974) are less frequently met. Thus, pseudoplateaus are used when a significant number of steps overlap globally at 2σ even if contiguous steps do not. For K-feldspars, plateau ages cannot be defined, but since we wish to compare and discuss series of steps with similar ages we used simple mean, thus unweighted, ages. Isochron ages are obtained on an inverse isochron diagram of ^{36}Ar /^{40}Ar versus ^{39}Ar/^{40}Ar (Roddick, 1978; Roddick et al., 1980), which often allows homogeneous excess components to be identified. Errors on age and intercept age include individual errors on each point and linear regression by York's method (1969). The goodness of fit relative to individual errors is measured by Mean Square Weighted Deviation (MSWD).

Classical furnace step heating was conducted and usually yielded an almost perfectly flat age spectra, from which plateau and isochron ages were calculated and are shown side by side to assess potential excess argon problems. If the inverse isochron age is close to the plateau age and ^{40}Ar/^{36}Ar is not significantly different from present day ^{40}Ar/^{36}Ar atmospheric ratio (295.5), we consider that the plateau age is reliable. When this is not the case, we suspect a non-atmospheric initial ^{40}Ar/^{36}Ar ratio and we thus prefer to rely on the inverse isochron age if this one is well determined.

All errors are quoted at 2 sigmas.

References

Arnaud, N., P. Tapponnier, F. Roger, M. Brunel, U. Scharer, C. Wen, and Z. Q. Xu (2003), Evidence for Mesozoic shear along the western Kunlun and Altyn-Tagh fault, northern Tibet (China), *J. Geophys. Res.*, *108*, DOI: 10.1029/2001JB000904.

Berger, G. W., and D. York (1981), Geothermometry from Ar-40-Ar-39 Dating Experiments, *Geochim. Cosmochim. Acta*, *45*, 795-811.

Borghi, A., D. Castelli, B. Lombardo, and D. Visona (2003), Thermal and baric evolution of garnet granulites from the Kharta region of S Tibet, E Himalaya, *Eur. J. Mineral.*, *15*, 401-418.

Catlos, E. J., C. S. Dubey, T. M. Harrison, and M. A. Edwards (2004), Late Miocene movement within the Himalayan Main Central Thrust shear zone, Sikkim, north-east India, *J. Metamorph. Geol.*, *22*, 207-226.

Compston, W., I. S. Williams, and C. E. Meyer (1984), U-Pb geochronology of zircons from lunar breccia 73217 using a sensitive high mass-resolution ion microprobe., *J. Geophys. Res.*, *89*, 525-534.

Cottle, J. M., M. J. Jessup, D. L. Newell, M. S. A. Horstwood, S. R. Noble, R. R. Parrish, D. J. Waters, and M. P. Searle (2009), Geochronology of granulitized eclogite from the Ama Drime Massif: Implications for the tectonic evolution of the South Tibetan Himalaya, *Tectonics*, *28*, DOI: 10.1029/2008TC002256.

Dale, J., T. Holland, and R. Powell (2000), Hornblende-garnet-plagioclase thermobarometry: a natural assemblage calibration of the thermodynamics of hornblende, *Contrib. Mineral. Petrol.*, *140*, 353-362.

Dalrymple, G. B., and M. A. Lanphere (1974), Ar-40/Ar-39 Age Spectra of Some Undisturbed Terrestrial Samples, *Geochim. Cosmochim. Acta*, *38*, 715-738.

Deloule, E., M. Chaussidon, B. P. Glass, and C. Koeberl (2001), U-Pb isotopic study of relict zircon inclusions recovered from Muong Nong-type tektites, *Geochim. Cosmochim. Acta*, *65*, 1833-1838.

Farley, K. A., R. A. Wolf, and L. T. Silver (1996), The effects of long alpha-stopping distances on (U-Th)/He ages, *Geochim. Cosmochim. Acta*, *60*, 4223-4229.

Groppo, C., B. Lombardo, F. Rolfo, and P. Pertusati (2007), Clockwise exhumation path of granulitized eclogites from the Ama Drime range (Eastern Himalayas), *J. Metamorph. Geol.*, *25*, 51-75.

Hodges, K. V., W. E. Hames, W. Olszewski, B. C. Burchfiel, L. H. Royden, and Z. Chen (1994), Thermobarometric and Ar-40 Ar-39 Geochronological Constraints on Eohimalayan Metamorphism in the Dinggye Area, Southern Tibet, *Contrib. Mineral. Petrol.*, *117*, 151-163.

Holland, T., J. Baker, and R. Powell (1998), Mixing properties and activity-composition relationships of chlorites in the system MgO-FeO-Al2O3-SiO2-H2O, *Eur. J. Mineral.*, *10*, 395-406.

Holland, T., and R. Powell (1996), Thermodynamics of order-disorder in minerals.2. Symmetric formalism applied to solid solutions, *Am. Mineral.*, *81*, 1425-1437.

Holland, T. J. B., and R. Powell (1998), An internally consistent thermodynamic data set for phases of petrological interest, *J. Metamorph. Geol.*, *16*, 309-343.

Jessup, M. J., D. L. Newell, J. M. Cottle, A. L. Berger, and J. A. Spotila (2008), Orogen-parallel extension and exhumation enhanced by denudation in the trans-Himalayan Arun River gorge, Ama Drime Massif, Tibet-Nepal, *Geology*, *36*, 587-590.

Li, D., Q. Liao, Y. Yuan, Y. Wan, D. Liu, X. Zhang, S. Yi, S. Cao, and D. Xie (2003), SHRIMP U-Pb zircon geochronology of granulites at Rimana (Southern Tibet) in the central segment of Himalayan Orogen, *Chinese Sci. Bull.*, *48*, 2647-2650.

Liu, Y., W. Siebel, H. J. Massonne, and X. C. Xiao (2007), Geochronological and petrological constraints for tectonic evolution of the central Greater Himalayan Sequence in the Kharta area, southern Tibet, *J. Geol.*, *115*, 215-230.

Lombardo, B., and F. Rolfo (2000), Two contrasting eclogite types in the Himalayas: implications for the Himalayan orogeny, *J. Geodyn.*, *30*, 37-60.

Ludwig, K. R. (2003), Isoplot 3.00 a geochronological toolkit for Microsoft Excel, *Berkley Geochronology Center Spec. Pub.*, *4*.

Newton, R. C., T. V. Charlu, and O. J. Kleppa (1980), Thermochemistry of the High Structural State Plagioclases, *Geochim. Cosmochim. Acta*, *44*, 933-941.

Renne, P. R., C. C. Swisher, A. L. Deino, D. B. Karner, T. L. Owens, and D. J. DePaolo (1998), Intercalibration of standards, absolute ages and uncertainties in Ar-40/Ar-39 dating, *Chem. Geol.*, *145*, 117-152.

Roddick, J. C. (1978), Application of Isochron Diagrams in Ar-40-Dating Ar-39-Dating - Discussion, *Earth Planet. Sci. Lett.*, *41*, 233-244.

Roddick, J. C., R. A. Cliff, and D. C. Rex (1980), The Evolution of Excess Argon in Alpine Biotites - a Ar-40-Ar-39 Analysis, *Earth Planet. Sci. Lett.*, *48*, 185-208.

Scharer, U. (1984), The Effect of Initial Th-230 Disequilibrium on Young U-Pb Ages - the Makalu Case, Himalaya, *Earth Planet. Sci. Lett.*, *67*, 191-204.

Spear, F. S. (1993), *Metamorphic Phase Equilibria and Pressure Temperature Time Paths. 2nd Eds.*, Mineralogical Society of America, Washington, DC.

Stern, R. A. (1997), The GSC Sensitive High Resolution Ion Microprobe (SHRIMP); analytical techniques of zircon U-Th-Pb age determinations and performance evaluation., *Current Research - Geol. Surv. Can.*

Stern, R. A., and Y. Amelin (2003), Assessment of errors in SIMS zircon U-Pb geochronology using a natural zircon standard and NIST SRM 610 glass, *Chem. Geol.*, *197*, 111-142.

Tera, F., and G. J. Wasserburg (1972), U-Th-Pb Systematics in 3 Apollo 14 Basalts and Problem of Initial Pb in Lunar Rocks, *Earth Planet. Sci. Lett.*, *14*, 281-&.

White, R. W., R. Powell, and T. J. B. Holland (2007), Progress relating to calculation of partial melting equilibria for metapelites, *J. Metamorph. Geol.*, *25*, 511-527.

White, R. W., R. Powell, T. J. B. Holland, and B. A. Worley (2000), The effect of TiO2 and Fe2O3 on metapelitic assemblages at greenschist and amphibolite facies conditions: mineral equilibria calculations in the system K2O-FeO-MgO-Al2O3-SiO2-H2O-TiO2-Fe2O3, *J. Metamorph. Geol.*, *18*, 497-511.

Wiedenbeck, M., P. Alle, F. Corfu, W. L. Griffin, M. Meier, F. Oberli, A. Vonquadt, J. C. Roddick, and W. Speigel (1995), 3 Natural Zircon Standards for U-Th-Pb, Lu-Hf, Trace-Element and Ree Analyses, *Geostand. Mewslett.*, *19*, 1-23.

Williams, C. T. (1996), Analysis of rare earth minerals, in *Rare earth minerals. Chemistry, origin and ore deposits*,7, edited by A. P. Jones, et al., pp. 327-348, Chapman and Hall, London.

York, D. (1969), Least Squares Fitting of a Straight Line with Correlated Errors, *Earth Planet. Sci. Lett.*, *5*, 320-&.

Zhang, J. J., and L. Guo (2007), Structure and geochronology of the southern Xainza-Dinggye rift and its relationship to the south Tibetan detachment system, *J. Asian Earth Sci.*, *29*, 722-736.

Table DR1 : micro-structural data

general location	zone (Fig. 3a)	GPS outcrop	GPS handset UTM coordinates (zone 45R) easting	nording	altitude (m)	facies	structure	plane strike & dip	direction Azimuth or pitch	sense
STDsz Dzakar Chu	a	7-74	536333	3127952	3755	micaschists and gneiss	foliation	N090 12N	/	
		7-22	527382	3134169	3883	micaschists and defomed leucogranites	foliation / lineation	N080 45N	P 45E	
		7-75	525128	3134736	3910	defomed leucogranite	foliation / lineation	N070 50N	P 10E	
						defomed leucogranite	foliation / lineation	N080 45N	P 22E	
						micaschists	foliation	N083 50N	/	
						micaschists	foliation	N075 53N	/	
		7-21	522482	3135439	3976	micaschists and defomed leucogranites	foliation / lineation	N055 10N	Az 30	top to theN
North-Kharta basin	b	7-72	533691	3122621	3758	deformed granite	foliation / lineation	N000 45W	P20N	
						deformed granite		N000 40W	P20N	
						plan plus tardif	foliation / lineation	N005 63W	/	
						deformed granite	foliation / lineation	N170 30W	P20N	
						deformed granite	foliation / lineation	N155 45W	P0	
North-Kharta	c	7-30	533268	3112113	3680	migmatitic gt paragneiss	foliation	N150 30W	/	
						migmatitic gt paragneiss	foliation	N000 25W	/	
						migmatitic gt paragneiss	foliation / lineation	N154 40W	Az 30	
						migmatitic gt paragneiss	foliation	N156 45W	/	
						migmatitic gt paragneiss	foliation / lineation	N150 30W	Az 40	
		7-69	534388	3112074	3611	Chlorite bearing fault	fault plane	N160 54W	/	
						Chlorite bearing fault	fault plane / striation	N022 50E	p82N	
						migmatitic gt paragneiss	foliation / lineation	N135 50W	P50S	top to the S?
						migmatitic gt paragneiss	foliation	N160 50W	/	
						migmatitic gt paragneiss	foliation	N145 68W	/	
						migmatitic gt paragneiss	foliation / lineation	N162 53W	P62S	
						gneiss	foliation / lineation	N150 54W	P54S	
						migmatitic gt paragneiss	foliation / lineation	N155 62W	p35S	
						migmatitic gt paragneiss	foliation / lineation	N142 62W	P40S	
						migmatitic gt paragneiss	foliation / lineation	N155 60W	P52S	
		7-70	533710	3115063	3638	migmatitic paragneiss		N150 45W	/	
						migmatitic paragneiss		N150 42W	P70S	
		7-71	533358	3116258	3684	migmatitic paragneiss		N150 40W	/	
South-Kharta	d	7-26	530582	3106039	3761	migmatitic gt paragneiss	foliation	N050 70N	/	
						migmatitic gt paragneiss	foliation	N045 80N	/	
						migmatitic gt paragneiss	foliation	N050 80N	/	
						migmatitic gt paragneiss	foliation	N050 70N	/	
		7-27	531028	3106176	3737	migmatitic gt paragneiss	foliation	N045 30N	/	
						migmatitic gt paragneiss	foliation	N050 40N	/	
						migmatitic gt paragneiss	foliation	N040 50N	/	
		7-28	533390	3107737	3650	deformed gt-bt leucogranite	foliation	N045 30N	/	
Arun South gorges	e	7-58	535328	3108180	3575	green schist foliation	foliation	N000 55W	/	
		7-64	535382	3107980	3586	mylonitic ortogneiss	foliation / lineation	N170 60W	P60S	top to the W
		7-57	535400	3107973	3595	phlogopite rich level	foliation / lineation	N150 60W	P67S	
		7-63	535429	3107977	3588	Mylonitic orthogneiss	foliation	N015 75W	/	
						Mylonitic orthogneiss	foliation	N005 60W	/	
		7-56	535459	3107968	3583	Chlorite cataclasite	foliation	N170 47W	/	
		7-40	535890	3107836	3596	folded quartz cataclasite	foliation	N165 13W	/	
		7-41	535996	3107755	3609	cataclasite	foliation / lineation	N020 37W	Az 100	
		7-62	535994	3107747	3628	cataclastic orthogneiss	foliation / lineation	N000 40W	Az90	
		7-61	536095	3107586	3670	mylonite	foliation / lineation	N000 55W	/	
		7-55	536161	3107508	3665	garnet micaschist	foliation / lineation	N000 25W	Az 25	
		7-54	536207	3107381	3648	mylonite	foliation / lineation	N176 58W	P82N	
		7-53	536408	3106929	3702	mylonitic orthogneiss	foliation	N010 40W	/	
		7-42	536644	3106653	3749	Leucocratic gneiss	foliation / lineation	N130 35S	Az 130	
		7-51	536694	3106562	3761	garnet micaschist	foliation / lineation	N165 34W	P 48N	
		7-50	536731	3106479	3735	gneiss	foliation	N014 44W	/	
						gneiss	foliation / lineation	N173 62W	P82N	
		7-49	536752	3106372	3707	gneiss	foliation / lineation	N000 50W	Az 115	top to the W
						gneiss	foliation	N160 45W	/	
						gneiss	foliation	N172 50W	/	
		7-48	536834	3106266	3710	leucocratic gneiss	foliation	N170 28W	/	
		7-47	537011	3106030	3686	gneiss	foliation / lineation	N000 42W	P 42N	top to the W
		7-46	537084	3105891	3665	gneiss	foliation	N020 55W	/	
						gneiss	foliation	N030 20W	/	
		7-45	537157	3105723	3647	orthogneiss	foliation	N025 55 W	/	
West Tanghyu valley	f	7-65	537487	3123305	4078	Mylonitic quartzite	foliation	N050 35W	/	
						Mylonitic quartzite	foliation	N045 23W	/	
						brittle fault	fault plane	N020 65W	/	
		7-66	537600	3123282	4119	Mylonitic gneiss	foliation / lineation	N020 40W	Az 110	
						Mylonitic gneiss	foliation / lineation	N015 35W	AZ 115	
						Mylonitic gneiss	foliation / lineation	N015 30W	AZ 112	Top to the W
						Mylonitic gneiss	foliation / lineation	N175 45W	AZ 110	
						Mylonitic gneiss	foliation / lineation	N010 35W	AZ 95	Top to the W
		7-67	537688	3123260	4117	Biotite rich gneiss with deformed leucocratic veins	foliation / lineation	N155 30W	Az 110	Top to the W
						Biotite rich gneiss with deformed leucocratic veins	foliation / lineation	N030 22W	/	
						Biotite rich gneiss with deformed leucocratic veins	foliation / lineation	N020 26W	Az 100	
		7-68	537931	3123217	4099	deformed granitic dyke		N025 55W	Az 111	
						"a" fold		N000 20W	/	
								N05 32W	Az 85	Top to the W
								N05 42W	Az 95	

Data plotted on Fig. 4. For zone locations see Fig. 2a.

Table DR1 (continued)

general location	zone (Fig. 3a)	GPS outcrop	UTM coordinates (zone 45R) easting	nording	altitude (m)	facies	structure	plane strike & dip	direction Azimuth or pitch	sense
Upper Arun gorges	g	7-39	538901	3127273	3944	brittle fault plane with hematite cristalisations in quartzitic cataclasite	fault plane	N020 54 W	/	
						brittle fault plane with hematite cristalisations in quartzitic cataclasite	fault plane / striation	N015 57W	P65N	
						overall fault plane at the top of the quarztic cataclasite	fault plane	N020 40W	/	
		7-38	538896	3127186	3950	Mylonitic Quartzite	foliation / lineation	N000 27W	Az 107	
						Mylonitic Quartzite	foliation / lineation	N000 43W	/	
						Mylonitic Quartzite	foliation / lineation	N005 40W	Az 120	
						Mylonitic Quartzite	foliation / lineation	N000 27W	Az 107	
						brittle fault	fault plane	N015 60W	/	
		7-37	538926	3127119	3944	gneiss	foliation / lineation	N060 20W	Az 105	Top to the W
						deformed tourmaline leucogranite	foliation / lineation	N035 32W	Az 108	
						biotite level in gneiss	foliation / lineation	N045 28W	Az 110	
						deformed microgranite	foliation / lineation	N025 36W	Az 111	
		7-35	539039	3127112	3931	biotitite	shear plane	N025 55W	/	Top to the W
		7-34	539065	3127102	3902	orthogneiss	foliation / lineation	N015 30W	Az 115	Top to the W
		between 7-33 and 7-34				migmatitic gneiss	foliation / lineation	N110 20E	Az 100	
		between 7-33 and 7-34				migmatitic gneiss	foliation / lineation	N060 22W	Az 125	
		between 7-33 and 7-34				migmatitic gneiss	foliation / lineation	N042 20W	Az 98	
		between 7-33 and 7-34				migmatitic gneiss	foliation / lineation	N170 29W	Az 65	
		7-33	539159	3127192	3938	orthogneiss	foliation / lineation	N060 35W	Az 115	Top to the W
						deformed tourmaline leucogranite	foliation / lineation	N015 32W	Az 110	
						orthogneiss	foliation / lineation	N055 42W	/	
						deformed tourmaline leucogranite	foliation / lineation	N040 35W	Az 120	
						deformed tourmaline leucogranite	foliation / lineation	N030 30W	Az 115	
North flanck	h	7-88	550322	3135144	4408	quartz cataclasite with chlorite and muscovite recristalisation	foliation	N032 45W	/	
						quartzitic cataclasite	foliation	N022 60W	/	
						quartzitic cataclasite	foliation	N022 42W	/	
						quartzitic cataclasite	foliation	N020 60W	/	
		7-89	550271	3135292	4394	micaschists	foliation	N164 20E	/	
		7-90	550348	3135499	4420	gneiss	foliation	N170 18E	/	
						gneiss	foliation / lineation	N175 30E	Az 10	
		7-91	550312	3136633	4253	orthogneiss	foliation / lineation	N040 33W	P50N	
		7-92	550638	3136941	4167	orthogneiss	foliation / lineation	N030 35 W	Az 10	
						orthogneiss	foliation / lineation	N10 30 W	Az 12	
NW Sankar	i	7-93	560047	3137875	4476	marble	S0/S1	N128 38N	/	
		7-128	563336	3137809	4681	paragneiss	folded schitosity (Sn)	N148 30NE	/	
						paragneiss	folded schitosity (Sn)	N142 20NE	/	
						paragneiss	folded schitosity (Sn)	N130 30NE	/	
						paragneiss	Axial schistosity (Sn+1)	N105 20N	/	
						paragneiss	Axial schistosity (Sn+1)	N120 05N	/	
						paragneiss	Axial schistosity (Sn+1)	N120 13N	/	
		7-127	562945	3137634	4670	migmatitic gneiss	foliation	N135 45N	/	
		7-130	563649	3138762	4574	migmatitic gneiss	foliation	N080 23S	/	
		7-125	565551	3144938	4210	marble	S0/S1	N080 10N	/	
North Dinggye	j	237	573786	3142785	4266	deformed leucogranite	foliation / lineation	N060 20N	Az 160	top to theN
						quartz cataclasite with large Gt	foliation / lineation	N045 25N	Az 125	
						deformed leucogranite	foliation / lineation	N100 14N	Az 155	
						micaschist	foliation	N80 20N		
						micaschist in granite	foliation	N120 30N		
						micaschist in granite	foliation	N060 42N		
						micaschist in granite	foliation	N85 30N		
		238	572884	3143786	4367	deformed leucogranite	foliation / lineation	N046 26N	Az 093	top to the E
						gneiss	foliation / lineation	N040 40N	Az 105	
East Sangkar Ri	k	227	570685	3132356	4944	Chlorite fault plane	fault plane / striation	N020 355	Az 110	
						Chlorite fault plane	fault plane / striation	N030 60E	P 80S	
		229	570367	3132460	5059	deformed leucogranite	foliation / lineation	N067 16S	Az 110	
						othogneiss	foliation / lineation	N035 42S	P 78N	
						othogneiss	foliation / lineation	N030 20S	Az 100	
		233	570332	3132491	5077	gneiss cataclasite	brittle plane	N02 57 E		
		232	570277	3132518	5087	orthogneiss	foliation / lineation	N025 42E	P 89N	
		231	570260	3132540	5098	paragneiss	foliation / lineation	N030 30S	Az 103	
		230	570192	3132561	5124	deformed leucogranite	foliation /lineation	N020 17E	Az 092	
						Garnet micaschist	foliation /lineation	N014 42E	P 82S	
						paragneiss	foliation /lineation	N005 40E	P 73S	top to the E
SouthNyonno Ri	l	225	559995	3115086	5419	amphibolite	foliation / lineation	N020 34E	Az 000	
						orthogneiss	foliation / lineation	N000 22E	Az 172	
						orthogneiss	foliation / lineation	N010 45E	Az 175	
						amphibolite	foliation / lineation	N040 12E	Az 015	
South East Nyonno Ri	m	192	563680	3114300	5272	quartz cataclasite	fault plane	N006 49E		
		177	563611	3113336	5086	chlorite mylonite	foliation / lineation	N155 40E	P 77S	top to the E
						chlorite mylonite	foliation / lineation	N158 37E	P 62S	
		178	563487	3113287	5069	orthogneiss	C plane / lineation	N025 50E	p 80S	
		184	563427	3114679	5237	micaschist	foliation / lineation	N005 50E	P 90	
						Gt migmatitic gneiss	foliation / lineation	N000 35E	P 82N	
		181	563422	3113304	5082	orthogneiss	Chlorite foliation / lineatior	N160 60E	P 82S	top to the E
		180	563187	3113231	5084	orthogneiss	foliation / lineation	N020 37E	Az 090	top to the E
		179	562748	3113774	5217	orthogneiss	foliation / lineation	N000 65E	P 03N	dextral?
STDsz Saer	o	219	569208	3116088	4569	deformed leucogranite	foliation / lineation	N020 48W	Az 018	
						deformed leucogranite	foliation / lineation	N035 30W	Az 030	
						micaschist and leucogranite	brittle fault plane	N000 55E		
		218	570346	3115866	4451	micaschist	foliation / lineation	N030 45W	Az 27	
						orthogneiss	foliation / lineation	N010 43W	P 20S	top to theN
						deformed leucogranite	foliation / lineation	N010 45W	P 23S	top to theN
						deformed leucogranite	foliation / lineation	N002 65W	P 22S	
		182	572937	3118477	4284	deformed leucogranite	foliation / lineation	N036 40W	Az 044	
		222	576656	3117898	4263	Garnet micaschist	foliation / lineation	N020 08W	Az 020	top to theN
						Garnet micaschist	foliation / lineation	N000 14W	Az 015	top to theN
						Garnet micaschist	foliation / lineation	N100 12S	Az 020	top to theN
		220	580542	3116399	4399	Ordovician sandstones	S0/S1 - lineation	N110 14N	Az 030	top to theN

Data plotted on Fig. 4. For zone locations see Fig. 2a.

Table DR2: Mineral data (1) representative composition of biotite

Sample	T5D39b	T5D39b	T5D39b*	T5D39b*	T5D33	T5D33	T5D33	T5D33	T5D33	T5D33	T5D33	T5D33	T5D33*
SiO2	35.20	35.08	34.74	34.22	35.07	34.99	34.04	34.96	35.63	35.30	35.24	34.38	35.73
Al2O3	18.26	19.24	18.67	18.50	19.47	19.86	18.25	19.31	18.70	18.95	18.81	19.89	22.18
FeO	22.04	20.15	22.59	21.36	20.59	21.27	19.79	21.34	21.45	20.79	21.48	21.01	21.27
MnO	0.19	0.14	0.17	0.16	0.17	0.14	0.17	0.22	0.20	0.15	0.17	0.20	0.23
MgO	6.97	8.17	6.88	7.46	7.98	7.37	7.47	7.50	6.98	7.44	7.36	7.99	6.64
CaO	0.00	0.00	0.05	0.02	0.00	0.00	0.00	0.00	0.00	0.00	0.00	0.06	0.04
Na2O	0.14	0.10	0.13	0.13	0.12	0.14	0.13	0.11	0.14	0.10	0.12	0.19	0.18
K2O	10.12	10.15	10.10	10.07	10.26	10.11	10.13	10.18	10.18	10.17	10.20	9.77	10.25
TiO2	3.61	3.22	3.35	3.14	2.21	2.19	3.56	2.58	3.13	3.78	3.43	1.04	1.23
Total	96.64	96.25	96.68	95.06	95.91	96.07	93.56	96.22	96.41	96.80	96.83	94.55	97.75
Si	5.46	5.39	5.40	5.38	5.43	5.42	5.41	5.42	5.50	5.42	5.43	5.41	5.41
Al tet	2.54	2.61	2.60	2.62	2.57	2.58	2.59	2.58	2.50	2.58	2.57	2.59	2.59
Al octa	0.80	0.88	0.82	0.81	0.98	1.04	0.83	0.95	0.90	0.85	0.84	1.10	1.36
Fe^{2+}	2.54	2.30	2.61	2.50	2.37	2.45	2.34	2.46	2.46	2.37	2.46	2.46	2.39
Fe^{3+}	0.03	0.03	0.03	0.03	0.03	0.03	0.03	0.03	0.03	0.03	0.03	0.03	0.03
Mg	1.61	1.87	1.59	1.75	1.84	1.70	1.77	1.73	1.61	1.70	1.69	1.87	1.50
Ti	0.42	0.37	0.39	0.37	0.26	0.25	0.43	0.30	0.36	0.44	0.40	0.12	0.14
Mn	0.02	0.02	0.02	0.02	0.02	0.02	0.02	0.03	0.03	0.02	0.02	0.03	0.03
Li	0.00	0.00	0.00	0.00	0.00	0.00	0.00	0.00	0.00	0.00	0.00	0.00	0.00
K	2.00	1.99	2.00	2.02	2.02	2.00	2.05	2.01	2.01	1.99	2.00	1.96	1.98
Na	0.04	0.03	0.04	0.04	0.04	0.04	0.04	0.03	0.04	0.03	0.03	0.06	0.05
X_{Fe}	0.61	0.55	0.62	0.59	0.57	0.59	0.57	0.59	0.61	0.59	0.60	0.57	0.62

Weight oxide (%), cations p.f.u. and X_{Fe} [(Fe/Mg+Fe)] as calculated for each electronic microprobe measurement. Fe^{3+} has been calculated by stoichiometry.* data used for classical thermobarometry.

Table DR2: Mineral data (2) representative composition of muscovite

Sample	T5D39b	T5D39b	T5D39b	T5D39b	T5D39b	T5D39b	T5D39b	T5D39b	T5D33	T5D33	T5D33	T5D33	T5D33	T5D33
Location	Gt incl	Gt incl	Gt incl	Gt incl	Fol	Fol	Fol	Fol	Fol	Fol	Fol	Fol	Fol	Fol
SiO2	49.03	49.97	49.56	49.39	46.05	46.13	47.33	45.53	45.89	46.64	46.26	47.14	47.02	47.20
Al2O3	32.02	33.22	34.85	33.97	35.45	34.70	34.24	35.96	34.87	35.58	35.67	34.74	36.71	35.64
FeO	1.62	2.09	1.10	1.66	1.04	1.73	1.15	1.19	1.31	1.12	0.49	1.50	0.55	1.15
MnO	0.03	0.00	0.02	0.03	0.01	0.01	0.02	0.00	-0.01	0.00	0.01	-0.01	0.00	0.00
MgO	0.90	0.65	0.44	0.44	0.58	0.87	0.61	0.47	0.65	0.53	0.47	0.76	0.49	0.50
CaO	0.06	0.05	0.06	0.07	0.00	0.00	0.02	0.00	0.00	0.01	0.00	-0.01	0.01	0.00
Na2O	0.03	0.04	0.05	0.08	0.28	0.43	0.33	0.40	0.37	0.37	0.45	0.30	0.33	0.32
K2O	10.74	11.22	10.66	10.72	11.55	11.02	11.07	11.53	11.39	11.21	11.40	11.52	11.15	11.58
TiO2	0.00	0.01	0.01	0.03	0.21	0.02	0.20	0.28	0.43	0.38	0.38	0.11	0.03	0.02
Total	94.42	97.25	96.75	96.40	95.18	94.91	94.98	95.35	94.92	95.87	95.16	96.07	96.28	96.40
Si	6.55	6.50	6.43	6.46	6.15	6.18	6.31	6.08	6.15	6.17	6.16	6.24	6.17	6.21
Al tet	1.45	1.50	1.57	1.54	1.85	1.82	1.69	1.92	1.85	1.83	1.84	1.76	1.83	1.79
Al octa	3.59	3.59	3.76	3.69	3.73	3.66	3.69	3.74	3.66	3.72	3.76	3.66	3.84	3.74
Fe^{2+}	0.02	0.03	0.01	0.02	0.01	0.02	0.01	0.01	0.02	0.01	0.01	0.02	0.01	0.01
Fe^{3+}	0.14	0.18	0.09	0.15	0.09	0.15	0.10	0.11	0.12	0.10	0.04	0.13	0.05	0.10
Mg	0.18	0.13	0.09	0.09	0.12	0.17	0.12	0.09	0.13	0.11	0.09	0.15	0.10	0.10
Ti	0.00	0.00	0.00	0.00	0.02	0.00	0.02	0.03	0.04	0.04	0.04	0.01	0.00	0.00
Mn	0.00	0.00	0.00	0.00	0.00	0.00	0.00	0.00	0.00	0.00	0.00	0.00	0.00	0.00
Li	0.00	0.00	0.00	0.00	0.00	0.00	0.00	0.00	0.00	0.00	0.00	0.00	0.00	0.00
K	1.83	1.86	1.77	1.79	1.97	1.88	1.88	1.96	1.95	1.89	1.94	1.95	1.86	1.95
Na	0.01	0.01	0.01	0.02	0.07	0.11	0.09	0.10	0.10	0.09	0.12	0.08	0.08	0.08
Xfe	0.47	0.62	0.53	0.65	0.45	0.50	0.48	0.57	0.52	0.50	0.36	0.50	0.38	0.52
ALVI	3.59	3.59	3.76	3.69	3.73	3.66	3.69	3.74	3.66	3.72	3.76	3.66	3.84	3.74

Weight oxide (%), cations p.f.u. and X_{Fe} [(Fe/Mg+Fe)] as calculated for each electronic microprobe measurement. Fe^{3+} has been calculated by stoichiometry.
Inclusion within garnet (Inc) and in foliation (Fol)

Table DR2: Mineral data (3) representative composition of garnet

	Garnet T5D39b, Fig. 7 profile																
	A																
Zone	IIb	IIb	IIb	IIb	IIb	IIb	IIb	IIb	IIb	IIb	IIb/IIa	IIa	IIa	IIa	IIa	IIa	IIa/Ib
SiO2	37.78	37.63	37.96	38.17	37.81	37.78	38.06	38.21	38.23	37.89	38.21	38.14	38.14	38.10	38.11	38.21	38.35
Al2O3	21.35	21.43	21.52	21.54	21.44	21.27	21.52	21.59	21.69	21.46	21.78	21.65	21.61	21.45	21.52	21.65	21.76
MgO	4.16	4.27	4.25	4.33	4.29	4.31	4.48	4.58	4.67	4.96	4.98	5.02	5.01	4.86	4.88	4.99	5.03
FeO	34.53	34.21	33.79	33.96	33.95	33.75	34.09	33.68	33.54	33.56	33.00	33.08	32.54	32.17	32.27	32.15	31.82
MnO	1.81	1.74	1.63	1.61	1.61	1.55	1.53	1.49	1.41	1.37	1.34	1.35	1.36	1.36	1.37	1.34	1.35
Cr2O3	0.02	0.03	0.02	0.03	0.01	0.02	0.02	0.01	0.00	0.03	0.01	0.01	0.00	0.01	0.00	0.00	0.01
TiO2	0.00	0.00	0.01	0.02	0.01	0.01	0.01	0.01	0.00	0.02	0.02	0.01	0.00	0.00	0.00	0.00	0.00
NiO	0.01	0.00	0.01	0.01	0.02	0.01	0.01	0.01	0.01	0.01	0.00	0.01	0.00	0.00	0.01	0.01	0.01
CaO	0.96	1.48	1.76	1.77	1.68	1.65	1.61	1.72	1.77	1.75	1.81	1.92	2.30	2.80	2.67	2.63	2.77
Na2O	0.00	0.00	0.01	0.00	0.02	0.01	0.02	0.00	0.00	0.01	0.01	0.01	0.02	0.01	0.01	0.01	0.01
K2O	0.01	0.02	0.02	0.01	0.00	0.01	0.01	0.02	0.00	0.01	0.01	0.01	0.01	0.01	0.01	0.01	0.00
∑ oxydes	100.63	100.81	100.99	101.45	100.85	100.39	101.37	101.30	101.31	101.07	101.18	101.21	100.98	100.77	100.85	100.98	101.10
Site T																	
Si	6.01	5.96	6.00	6.00	5.98	6.01	5.99	6.01	6.00	5.96	5.99	5.98	5.99	5.99	5.99	5.99	6.00
Al IV	-0.01	0.04	0.00	0.00	0.02	-0.01	0.01	-0.01	0.00	0.04	0.01	0.02	0.01	0.01	0.01	0.01	0.00
Site O																	
Al VI	4.01	3.97	4.01	4.00	3.98	3.99	3.98	4.01	4.02	3.94	4.02	3.98	3.98	3.97	3.98	3.99	4.01
Cr	0.00	0.00	0.00	0.00	0.00	0.00	0.00	0.00	0.00	0.00	0.00	0.00	0.00	0.00	0.00	0.00	0.00
Ti	0.00	0.00	0.00	0.00	0.00	0.00	0.00	0.00	0.00	0.00	0.00	0.00	0.00	0.00	0.00	0.00	0.00
∑	4.01	3.97	4.01	4.00	3.99	3.99	3.98	4.01	4.02	3.94	4.02	3.98	3.98	3.97	3.98	3.99	4.02
Site A																	
Mg	0.98	1.01	1.00	1.02	1.01	1.02	1.05	1.07	1.09	1.16	1.16	1.17	1.17	1.14	1.14	1.17	1.17
Fe	4.59	4.53	4.46	4.47	4.49	4.49	4.48	4.43	4.40	4.41	4.33	4.34	4.27	4.23	4.24	4.22	4.16
Mn	0.24	0.23	0.22	0.22	0.22	0.21	0.20	0.20	0.19	0.18	0.18	0.18	0.18	0.18	0.18	0.18	0.18
Ni	0.00	0.00	0.00	0.00	0.00	0.00	0.00	0.00	0.00	0.00	0.00	0.00	0.00	0.00	0.00	0.00	0.00
Ca	0.16	0.25	0.30	0.30	0.29	0.28	0.27	0.29	0.30	0.29	0.30	0.32	0.39	0.47	0.45	0.44	0.46
Na	0.00	0.00	0.00	0.00	0.00	0.00	0.01	0.00	0.00	0.00	0.00	0.00	0.01	0.00	0.00	0.00	0.00
K	0.00	0.00	0.00	0.00	0.00	0.00	0.00	0.00	0.00	0.00	0.00	0.00	0.00	0.00	0.00	0.00	0.00
∑	5.99	6.03	5.99	6.00	6.01	6.01	6.02	5.99	5.98	6.06	5.98	6.02	6.02	6.03	6.02	6.01	5.98
% Alm	0.77	0.75	0.75	0.75	0.75	0.75	0.75	0.74	0.74	0.73	0.72	0.72	0.71	0.70	0.70	0.70	0.70
% Gros	0.03	0.04	0.05	0.05	0.05	0.05	0.05	0.05	0.05	0.05	0.05	0.05	0.06	0.08	0.07	0.07	0.08
% Pyr	0.16	0.17	0.17	0.17	0.17	0.17	0.17	0.18	0.18	0.19	0.19	0.20	0.19	0.19	0.19	0.19	0.20
% Spess	0.04	0.04	0.04	0.04	0.04	0.03	0.03	0.03	0.03	0.03	0.03	0.03	0.03	0.03	0.03	0.03	0.03

Zone	Ib	Ib	Ib	Ib	Ib/Ia	Ia	Ia	Ia	Ia	Ia	Ia	Ia	Ia	Ia	Ia	Ia	Ia
SiO2	38.13	38.25	38.68	38.32	38.29	38.56	38.32	38.56	38.20	38.42	38.54	38.24	37.28	38.42	39.40	38.62	40.73
Al2O3	21.44	21.69	21.76	21.79	21.65	21.75	21.72	21.71	21.63	21.68	21.70	21.77	21.09	21.64	21.99	21.62	23.18
MgO	2.62	4.78	4.81	4.61	4.60	4.69	4.80	5.09	4.73	4.64	4.85	4.81	4.53	4.92	4.77	4.85	3.91
FeO	33.12	31.45	30.89	30.43	30.21	30.55	30.94	31.69	30.61	30.39	30.69	31.10	32.71	31.35	29.55	30.43	29.73
MnO	2.40	1.39	1.37	1.44	1.40	1.44	1.46	1.43	1.44	1.46	1.48	1.51	1.65	1.53	1.42	1.48	1.32
Cr2O3	0.00	0.02	0.00	0.01	0.00	0.00	0.01	0.00	0.02	0.01	0.02	0.01	0.10	0.01	0.00	0.02	0.01
TiO2	0.01	0.00	0.02	0.00	0.00	0.01	0.00	0.00	0.01	0.00	0.01	0.00	0.00	0.00	0.01	0.03	0.02
NiO	0.01	0.02	0.01	0.00	0.01	0.02	0.01	0.00	0.02	0.00	0.00	0.00	0.01	0.00	0.00	0.02	0.02
CaO	2.81	3.35	3.63	4.42	4.52	4.25	3.88	2.74	4.17	4.45	4.03	3.75	2.01	3.09	4.04	3.86	4.15
Na2O	0.00	0.01	0.00	0.01	0.02	0.03	0.00	0.02	0.00	0.03	0.02	0.00	0.03	0.02	0.13	0.01	0.00
K2O	0.12	0.00	0.00	0.00	0.00	0.00	0.00	0.00	0.01	0.01	0.06	0.00	0.02	0.01	0.09	0.01	0.01
∑ oxydes	100.67	100.96	101.18	101.04	100.71	101.30	101.15	101.23	100.83	101.10	101.40	101.19	99.43	100.97	101.42	100.94	103.07
Site T																	
Si	6.09	6.00	6.04	5.99	6.01	6.01	5.99	6.02	5.99	6.00	6.00	5.97	5.97	6.02	6.12	6.04	6.24
Al IV	-0.09	0.00	-0.04	0.01	-0.01	-0.01	0.01	-0.02	0.01	0.00	0.00	0.03	0.03	-0.02	-0.12	-0.04	-0.24
Site O																	
Al VI	4.12	4.00	4.05	4.01	4.01	4.01	3.99	4.02	3.98	4.00	3.99	3.99	3.95	4.02	4.14	4.03	4.43
Cr	0.00	0.00	0.00	0.00	0.00	0.00	0.00	0.00	0.00	0.00	0.00	0.00	0.01	0.00	0.00	0.00	0.00
Ti	0.00	0.00	0.00	0.00	0.00	0.00	0.00	0.00	0.00	0.00	0.00	0.00	0.00	0.00	0.00	0.00	0.00
∑	4.12	4.01	4.05	4.01	4.01	4.01	3.99	4.02	3.99	4.00	3.99	3.99	3.96	4.02	4.14	4.04	4.44
Site A																	
Mg	0.62	1.12	1.12	1.07	1.07	1.09	1.12	1.18	1.11	1.08	1.13	1.12	1.08	1.15	1.10	1.13	0.89
Fe	4.42	4.12	4.04	3.98	3.96	3.98	4.04	4.14	4.01	3.97	4.00	4.06	4.38	4.11	3.84	3.98	3.81
Mn	0.32	0.18	0.18	0.19	0.19	0.19	0.19	0.19	0.19	0.19	0.20	0.20	0.22	0.20	0.19	0.20	0.17
Ni	0.00	0.00	0.00	0.00	0.00	0.00	0.00	0.00	0.00	0.00	0.00	0.00	0.00	0.00	0.00	0.00	0.00
Ca	0.48	0.56	0.61	0.74	0.76	0.71	0.65	0.46	0.70	0.75	0.67	0.63	0.34	0.52	0.67	0.65	0.68
Na	0.00	0.00	0.00	0.00	0.01	0.01	0.00	0.01	0.00	0.01	0.01	0.00	0.01	0.00	0.04	0.00	0.00
K	0.02	0.00	0.00	0.00	0.00	0.00	0.00	0.00	0.00	0.00	0.01	0.00	0.00	0.00	0.02	0.00	0.00
∑	5.88	5.99	5.95	5.99	5.99	5.99	6.01	5.98	6.01	6.00	6.01	6.01	6.04	5.98	5.86	5.96	5.56
% Alm	0.76	0.69	0.68	0.66	0.66	0.67	0.67	0.69	0.67	0.66	0.67	0.68	0.73	0.69	0.66	0.67	0.69
% Gros	0.08	0.09	0.10	0.12	0.13	0.12	0.11	0.08	0.12	0.12	0.11	0.10	0.06	0.09	0.12	0.11	0.12
% Pyr	0.11	0.19	0.19	0.18	0.18	0.18	0.19	0.20	0.18	0.18	0.19	0.19	0.18	0.19	0.19	0.19	0.16
% Spess	0.06	0.03	0.03	0.03	0.03	0.03	0.03	0.03	0.03	0.03	0.03	0.03	0.04	0.03	0.03	0.03	0.03

																B
Zone	Ia	Ia	Ia	Ia	Ib	Ib	Ib	Ib	Ib	Ib/IIa	IIa	IIa	IIb	IIb	IIb	IIb
SiO2	38.50	38.46	38.34	38.55	38.31	38.43	38.43	38.39	38.25	38.30	38.21	43.33	38.17	38.16	38.19	37.83
Al2O3	21.68	20.56	21.79	21.70	21.60	21.70	21.65	21.68	21.57	21.49	21.67	23.07	21.63	21.68	21.47	21.46
MgO	4.81	1.54	4.80	4.64	4.73	4.76	4.81	4.97	4.98	5.03	4.95	4.38	4.92	4.76	4.51	3.94
FeO	30.69	27.45	30.68	30.31	30.27	30.68	31.20	31.47	31.75	32.29	32.65	28.28	33.69	33.60	33.98	34.60
MnO	1.42	1.25	1.37	1.32	1.23	1.21	1.23	1.21	1.18	1.22	1.27	1.10	1.36	1.45	1.56	1.93
Cr2O3	0.01	0.09	0.00	0.00	0.00	0.01	0.00	0.02	0.02	0.01	0.02	0.00	0.01	0.00	0.02	0.00
TiO2	0.02	0.02	0.02	0.02	0.02	0.02	0.02	0.02	0.02	0.02	0.00	0.00	0.02	0.02	0.00	0.01
NiO	0.00	0.00	0.00	0.02	0.01	0.00	0.00	0.01	0.00	0.00	0.02	0.00	0.01	0.00	0.01	0.00
CaO	3.96	2.14	4.16	4.73	4.58	4.28	3.70	3.46	3.02	2.58	2.27	2.72	1.51	1.37	1.36	1.01
Na2O	0.00	0.15	0.00	0.02	0.02	0.03	0.04	0.01	0.01	0.01	0.01	0.40	0.00	0.00	0.00	0.00
K2O	0.00	0.12	0.01	0.00	0.00	0.01	0.07	0.01	0.00	0.01	0.01	0.16	0.00	0.01	0.01	0.01
∑ oxydes	101.09	91.79	101.16	101.32	100.79	101.12	101.15	101.27	100.80	100.96	101.09	103.46	101.32	101.05	101.10	100.79
Site T																
Si	6.02	6.70	5.99	6.01	6.00	6.00	6.00	5.99	6.00	6.01	5.99	6.57	5.99	6.01	6.02	6.01
Al IV	-0.02	-0.70	0.01	-0.01	0.00	0.00	0.00	0.01	0.00	-0.01	0.01	-0.57	0.01	-0.01	-0.02	-0.01
Site O																
Al VI	4.01	4.92	4.00	4.00	3.99	4.00	3.99	3.98	3.99	3.98	4.00	4.69	3.99	4.03	4.01	4.03
Cr	0.00	0.01	0.00	0.00	0.00	0.00	0.00	0.00	0.00	0.00	0.00	0.00	0.00	0.00	0.00	0.00
Ti	0.00	0.00	0.00	0.00	0.00	0.00	0.00	0.00	0.00	0.00	0.00	0.00	0.00	0.00	0.00	0.00
∑	4.02	4.94	4.00	4.00	3.99	4.00	4.00	3.99	4.00	3.99	4.00	4.69	3.99	4.03	4.02	4.03
Site A																
Mg	1.12	0.40	1.12	1.08	1.10	1.11	1.12	1.16	1.17	1.18	1.16	0.99	1.15	1.12	1.06	0.93
Fe	4.01	4.00	4.01	3.95	3.97	4.01	4.08	4.11	4.17	4.24	4.28	3.59	4.42	4.42	4.48	4.60
Mn	0.19	0.18	0.18	0.17	0.16	0.16	0.16	0.16	0.16	0.16	0.17	0.14	0.18	0.19	0.21	0.26
Ni	0.00	0.00	0.00	0.00	0.00	0.00	0.00	0.00	0.00	0.00	0.00	0.00	0.00	0.00	0.00	0.00
Ca	0.66	0.40	0.70	0.79	0.77	0.72	0.62	0.58	0.51	0.43	0.38	0.44	0.25	0.23	0.23	0.17
Na	0.00	0.05	0.00	0.01	0.01	0.01	0.01	0.00	0.00	0.00	0.00	0.12	0.00	0.00	0.00	0.00
K	0.00	0.03	0.00	0.00	0.00	0.00	0.01	0.00	0.00	0.00	0.00	0.03	0.00	0.00	0.00	0.00
∑	5.98	5.06	6.00	6.00	6.01	6.00	6.00	6.01	6.00	6.01	6.00	5.31	6.01	5.97	5.98	5.97
% Alm	0.67	0.80	0.67	0.66	0.66	0.67	0.68	0.68	0.69	0.71	0.71	0.70	0.74	0.74	0.75	0.77
% Gros	0.11	0.08	0.12	0.13	0.13	0.12	0.10	0.10	0.08	0.07	0.06	0.09	0.04	0.04	0.04	0.03
% Pyr	0.19	0.08	0.19	0.18	0.18	0.18	0.19	0.19	0.19	0.20	0.19	0.19	0.19	0.19	0.18	0.16
% Spess	0.03	0.04	0.03	0.03	0.03	0.03	0.03	0.03	0.03	0.03	0.03	0.03	0.03	0.03	0.03	0.04

	T5D39b	T5D39b*	T5D39b*	T5D33	T5D33	T5D33	T5D33	T5D33	T5D33	T5D33*
Zone	Ia	IIb	IIb	rim	rim	core	core	core	core	rim
SiO2	38.67	37.67	37.53	37.37	37.77	38.60	38.61	38.18	38.17	37.72
Al2O3	21.62	21.63	21.74	21.35	21.39	21.49	21.56	21.50	21.55	21.53
MgO	4.54	4.43	4.24	2.86	3.28	5.43	5.68	4.27	3.54	3.93
FeO	29.84	33.75	33.97	34.64	34.70	32.61	32.33	34.10	34.92	34.03
MnO	1.14	2.24	2.52	2.86	2.01	0.70	0.64	0.83	1.25	1.43
Cr2O3	0.02	0.01	0.02	0.01	0.02	0.01	0.02	0.01	0.02	0.03
TiO2	0.06	0.02	0.02	0.02	0.03	0.02	0.03	0.00	0.01	0.06
NiO	0.00	0.02	0.02	0.00	0.00	0.00	0.00	0.00	0.00	0.03
CaO	5.24	1.26	1.36	1.69	1.77	2.18	2.32	2.23	2.02	2.30
Na2O	0.00	0.17	0.03	0.05	0.03	0.01	0.02	0.01	0.00	0.03
K2O	0.00	0.04	0.03	0.01	0.00	0.00	0.00	0.00	0.01	0.01
∑ oxydes	101.12	101.23	101.50	100.84	100.99	101.06	101.20	101.14	101.48	101.10
Site T										
Si	6.04	5.93	5.91	5.97	6.01	6.04	6.02	6.02	6.03	5.96
Al IV	-0.04	0.07	0.09	0.03	-0.01	-0.04	-0.02	-0.02	-0.03	0.04
Site O										
Al VI	4.01	3.94	3.94	3.99	4.02	4.00	3.98	4.01	4.04	3.97
Cr	0.00	0.00	0.00	0.00	0.00	0.00	0.00	0.00	0.00	0.00
Ti	0.01	0.00	0.00	0.00	0.00	0.00	0.00	0.00	0.00	0.01
∑	4.02	3.95	3.95	4.00	4.02	4.01	3.99	4.01	4.04	3.98
Site A										
Mg	1.06	1.04	1.00	0.68	0.78	1.27	1.32	1.00	0.83	0.93
Fe	3.89	4.44	4.47	4.63	4.62	4.27	4.22	4.49	4.61	4.50
Mn	0.15	0.30	0.34	0.39	0.27	0.09	0.08	0.11	0.17	0.19
Ni	0.00	0.00	0.00	0.00	0.00	0.00	0.00	0.00	0.00	0.00
Ca	0.88	0.21	0.23	0.29	0.30	0.37	0.39	0.38	0.34	0.39
Na	0.00	0.05	0.01	0.01	0.01	0.00	0.00	0.00	0.00	0.01
K	0.00	0.01	0.01	0.00	0.00	0.00	0.00	0.00	0.00	0.00
∑	5.98	6.05	6.05	6.00	5.98	5.99	6.01	5.99	5.96	6.02
% Alm	0.65	0.74	0.74	0.77	0.77	0.71	0.70	0.75	0.77	0.75
% Gros	0.15	0.04	0.04	0.05	0.05	0.06	0.06	0.06	0.06	0.06
% Pyr	0.18	0.17	0.16	0.11	0.13	0.21	0.22	0.17	0.14	0.15
% Spess	0.03	0.05	0.06	0.06	0.05	0.02	0.01	0.02	0.03	0.03

Weight oxide (%), cations p.f.u. and mineralogic end-members %, as calculated for each electronic microprobe measurement. * data used for classical thermobarometry.

Table DR2: Mineral data (4) representative composition of feldspar

Sample-loc	T5D33	T5D33	T5D33*	T5D39b	T5D39b	T5D39b	T5D39b	T5D39b	T5D39b	T5D39b	T5D39b	T5D39b	T5D39b	T5D39b	T5D39b*	T5D39b*	T5D33	T5D33	T5D39b	T5D39b
Feldspar type	Plag	Plag	Plag	Plag	Plag	Plag	Plag	Plag	Plag	Plag	Plag	Plag	Plag	Plag	Plag	Plag	Kfs	Kfs	Kfs	Kfs
Location	Fol	Fol	Fol	Gt incl	Gt incl	Gt incl	Gt incl - core	Gt incl - core	Gt incl - rim	Fol - core	Fol - rim	Fol	Fol	Fol	Fol	Fol	Fol	Fol	Fol	Fol
SiO2	57.30	58.17	57.75	57.40	59.70	60.30	59.01	60.02	61.37	63.19	62.26	62.59	61.96	63.75	61.90	61.58	64.24	63.99	64.33	64.46
Al2O3	27.25	26.75	26.71	27.74	25.33	25.12	25.87	25.28	24.00	23.28	23.69	23.57	24.14	22.82	24.23	24.42	18.62	18.63	18.70	18.70
MgO	0.01	0.00	0.00	0.00	0.00	0.00	0.00	0.01	0.00	0.00	0.00	0.00	0.00	0.00	0.00	0.00	0.00	0.01	0.00	0.01
FeO	0.03	0.02	0.09	0.31	0.07	0.20	0.05	0.02	0.18	0.00	0.02	0.01	0.00	0.02	0.13	0.22	0.01	0.00	0.00	0.00
MnO	0.01	0.01	0.01	0.00	0.00	0.02	0.01	0.00	0.00	0.00	0.03	0.01	0.00	0.00	0.00	0.00	0.01	0.00	0.00	0.01
Cr2O3	0.00	0.00	0.00	0.00	0.01	0.00	0.01	0.00	0.01	0.00	0.00	0.00	0.06	0.03	0.01	0.01	0.00	0.00	0.00	-0.01
TiO2	0.00	0.00	0.00	0.02	0.02	0.02	0.02	0.03	0.00	0.03	0.00	0.00	0.02	0.00	0.02	0.02	0.02	0.01	0.00	0.01
NiO	0.00	0.00	0.00	0.00	0.00	0.00	0.00	0.00	0.01	0.02	0.00	0.00	0.00	0.00	0.02	0.00	0.00	0.00	0.00	0.00
CaO	9.00	8.40	8.45	9.70	7.00	6.43	7.16	7.02	5.11	4.45	4.94	4.61	5.14	3.98	4.99	5.34	0.06	0.03	0.05	0.05
Na2O	6.37	6.99	6.85	6.19	7.45	8.06	7.26	7.43	8.40	8.71	8.67	8.86	8.75	9.26	8.87	7.89	1.24	1.22	1.40	1.46
K2O	0.22	0.11	0.18	0.08	0.37	0.13	0.37	0.35	0.36	0.44	0.27	0.52	0.25	0.45	0.26	0.17	15.67	15.78	15.41	15.44
Total	100.19	100.44	100.04	101.44	99.95	100.28	99.74	100.15	99.44	100.12	99.88	100.17	100.31	100.32	100.42	99.65	99.89	99.66	99.89	100.13
Site T																				
Si	2.56	2.59	2.59	2.55	2.67	2.68	2.64	2.67	2.74	2.79	2.76	2.77	2.74	2.81	2.74	2.73	2.98	2.98	2.98	2.98
Al	1.44	1.41	1.41	1.45	1.33	1.32	1.36	1.33	1.26	1.21	1.24	1.23	1.26	1.19	1.26	1.27	1.02	1.02	1.02	1.02
Site A																				
Mg	0.00	0.00	0.00	0.00	0.00	0.00	0.00	0.00	0.00	0.00	0.00	0.00	0.00	0.00	0.00	0.00	0.00	0.00	0.00	0.00
Fe	0.00	0.00	0.00	0.01	0.00	0.01	0.00	0.00	0.01	0.00	0.00	0.00	0.00	0.00	0.00	0.01	0.00	0.00	0.00	0.00
Mn	0.00	0.00	0.00	0.00	0.00	0.00	0.00	0.00	0.00	0.00	0.00	0.00	0.00	0.00	0.00	0.00	0.00	0.00	0.00	0.00
Cr	0.00	0.00	0.00	0.00	0.00	0.00	0.00	0.00	0.00	0.00	0.00	0.00	0.00	0.00	0.00	0.00	0.00	0.00	0.00	0.00
Ti	0.00	0.00	0.00	0.00	0.00	0.00	0.00	0.00	0.00	0.00	0.00	0.00	0.00	0.00	0.00	0.00	0.00	0.00	0.00	0.00
Ni	0.00	0.00	0.00	0.00	0.00	0.00	0.00	0.00	0.00	0.00	0.00	0.00	0.00	0.00	0.00	0.00	0.00	0.00	0.00	0.00
Ca	0.43	0.40	0.41	0.46	0.33	0.31	0.34	0.33	0.24	0.21	0.23	0.22	0.24	0.19	0.24	0.25	0.00	0.00	0.00	0.00
Na	0.55	0.60	0.60	0.53	0.65	0.70	0.63	0.64	0.73	0.75	0.75	0.76	0.75	0.79	0.76	0.68	0.11	0.11	0.13	0.13
K	0.01	0.01	0.01	0.00	0.02	0.01	0.02	0.02	0.02	0.02	0.02	0.03	0.01	0.03	0.01	0.01	0.93	0.94	0.91	0.91
∑	1.00	1.01	1.01	1.01	1.01	1.02	1.00	1.00	1.00	0.98	1.00	1.01	1.01	1.01	1.02	0.95	1.04	1.05	1.04	1.05
% Ab	0.55	0.60	0.59	0.53	0.64	0.69	0.63	0.64	0.73	0.76	0.75	0.75	0.74	0.79	0.75	0.72	0.11	0.11	0.12	0.13
% An	0.43	0.40	0.40	0.46	0.33	0.30	0.35	0.34	0.25	0.21	0.24	0.22	0.24	0.19	0.23	0.27	0.00	0.00	0.00	0.00
% Or	0.01	0.01	0.01	0.00	0.02	0.01	0.02	0.02	0.02	0.03	0.02	0.03	0.01	0.03	0.01	0.01	0.89	0.89	0.88	0.87

Weight oxide (%), cations p.f.u. and mineralogic end-members %, as calculated for each electronic microprobe measurement. * data used for classical thermobarometry.
Inclusion within garnet (Inc) and in foliation (Fol)

Table DR3: U/Pb zircons detailed data

Sample name	spot name	cristal	spot location b: border c: core	Age (Ma) 206/238	± (1σ)	Age (Ma) 207/235	± (1σ)	Age (Ma) 207/206	± (1σ)	206/238	± (%)	207/235	± (%)	207/206	± (%)	Used in average	U (ppm)	Th (ppm)	Th/U	Pb (ppm)	com m Pb (%)
T5D26	t5d20ter19	6	b2	7.3	0.2	7.3	1.7	14.3	471.8	0.00113	2.9	0.0072	22.9	0.0584	2.8	X	5953	104	0.02	5.8	0.04
T5D26	t5d20ter4	4	b	9.0	0.3	9.0	2.6	25.3	579.2	0.00139	2.8	0.0089	29.1	0.0497	1.6	X	8708	229	0.03	10.4	0.09
T5D26	4	1	c	9.1	0.4	9.1	1.8	7.5	414.2	0.00141	4.8	0.0090	20.2	0.0460	2.7	X	2889	21	0.01	3.5	0.41
T5D26	t5d20ter20	7	c	10.3	0.2	10.3	0.7	14.0	139.2	0.00159	2.2	0.0102	6.4	0.0495	1.2	X	7930	157	0.02	10.9	1.25
T5D26	t5d20ter7	5	b2	10.3	0.3	10.4	1.0	37.8	203.9	0.00160	3.0	0.0103	9.5	0.0570	2.8	X	8437	206	0.02	11.6	0.82
T5D26	t5d20ter18	6	b1	10.4	0.4	10.4	1.0	15.2	196.7	0.00162	3.5	0.0103	9.4	0.0529	2.9	X	15964	513	0.03	22.2	1.46
T5D26	t5d20ter21	8	c	10.5	0.2	10.5	0.6	15.0	117.2	0.00163	2.4	0.0104	5.6	0.0500	2.0	X	8519	157	0.02	11.9	0.41
T5D26	t5d20ter3	3	b	11.7	0.3	11.8	0.7	35.6	134.3	0.00181	2.5	0.0117	6.4	0.0474	1.1	X	8218	152	0.02	12.8	0.46
T5D26	t5d20ter2	3	c	11.7	0.3	11.7	0.7	6.4	137.2	0.00182	2.5	0.0116	6.4	0.0464	1.4	X	4743	81	0.02	7.4	0.00
T5D26	5	1	b1	21.5	1.0	21.7	6.9	37.9	628.6	0.00334	4.7	0.0216	32.4	0.0467	1.6		11006	113	0.01	31.6	0.00
T5D26	7	2	b	21.9	1.0	21.9	8.9	23.4	769.6	0.00340	4.5	0.0218	41.3	0.0631	3.9		8594	270	0.03	25.1	1.98
T5D26	6	2	c	27.1	1.2	27.1	9.7	24.9	695.2	0.00422	4.6	0.0271	36.5	0.0550	4.7		7847	256	0.03	28.4	1.05

See Fig. 7d and e.

Table DR4: U-Th/Pb monazite detailed data, (1) T5D5

Sample name	crystal	Spot Name	spot location b: border c: core	Age (Ma) 208/232	± (1σ)	208/232	± (%)	238/206	± (%)	207/206	± (%)	Used in 208/232average	Used in TW	U (ppm)	Th (ppm)	206* (ppm)	comm 206 (%)
T5D5	15	15.1	c	10.44	0.5	.00055	7.3	491.89	2.1	.0618	4.5	Pop1	Pop1	8382	45227	14.6	4.5
T5D5	13	13.1	c	10.51	0.5	.00055	4.1	482.17	2.7	.0968	5.9	Pop1	Pop1	2605	54338	4.6	14.5
T5D5	19	19.1	b c	10.81	0.4	.00058	3.0	512.02	2.2	.0681	4.8	Pop1	Pop1	6510	57747	10.9	11.7
T5D5	3	3.1	c	11.39	0.4	.00058	3.9	473.28	2.4	.0613	6.0	Pop1	Pop1	3811	50193	6.9	6.9
T5D5	3	3.2	b	11.56	0.6	.00059	6.0	453.66	2.7	.0905	6.1	Pop1	Pop1	2684	59805	5.1	9.5
T5D5	9	9.1	b c	11.57	0.5	.00059	4.4	470.30	3.5	.0770	7.8	Pop1	Pop2	2956	56918	5.4	6.4
T5D5	18	18.1	c	12.16	0.5	.00067	3.3	466.95	2.3	.1449	3.7	Pop2	Pop2	8083	37393	14.9	7.9
T5D5	10	10.1	b	12.58	0.4	.00065	3.2	470.71	2.3	.0524	6.0	Pop2	Pop2	5357	52357	9.8	7.7
T5D5	11	11.2	c	12.78	0.3	.00065	2.7	443.80	2.0	.0507	3.9	Pop2	Pop2	10720	57278	20.8	2.4
T5D5	7	7.1	c	12.85	0.5	.00066	3.5	485.23	2.8	.0619	4.7	Pop2	Pop2	8512	53337	15.1	3.3
T5D5	11	11.1	b	12.88	0.4	.00066	2.7	469.37	2.1	.0516	4.6	Pop2	Pop2	7069	45384	12.9	4.4
T5D5	6	6.1	c	13.12	0.4	.00067	2.7	443.66	2.1	.0569	4.5	Pop2	Pop2	6066	60744	11.7	4.3
T5D5	12	12.1	c	13.19	0.4	.00066	2.8	457.23	2.2	.0603	4.6	Pop2	Pop2	5819	56305	10.9	2.7
T5D5	16	16.1	b	13.2	0.4	.00067	2.7	464.95	2.1	.0578	4.6	Pop2	Pop2	6374	60274	11.8	3.6
T5D5	4	4.1	c	13.69	0.5	.00069	3.3	452.95	2.6	.0655	5.0	Pop2	Pop2	5826	55476	11.1	3.1
T5D5	14	14.1	c	13.7	0.4	.00069	3.0	435.87	2.3	.0501	5.7	Pop2	Pop2	5083	53145	10.0	3.7
T5D5	17	17.1	c	13.77	0.6	.00068	4.2	444.79	2.4	.0515	5.8	Pop2	Pop2	11749	84046	22.7	0.0
T5D5	1	1.1	c	13.88	0.4	.00070	2.8	454.36	2.0	.0518	4.3	Pop2	Pop2	11568	91474	21.9	2.5

206*: radiogenic Pb, comm206: common Pb. TW: Tera-Wasserburg. See Fig. 7a, b and c.

Table DR4: U-Th/Pb monazite detailed data, (2) T5D22

Sample name	crystal	Spot Name	spot location b: border c: core	Age (Ma) 208/232	± (1σ)	208/232	± (%)	238/206	± (%)	207/206	± (%)	Used in TW	U (ppm)	Th (ppm)	206* (ppm)	comm 206 (%)
T5D22	5	5.1	c	11.7	0.5	.00059	4.8	469.04	2.1	.0559	3.7	X	10262	106669	18.8	1.9
T5D22	2	2.2	b	12.2	0.4	.00061	3.1	500.76	2.1	.0551	3.9		8964	75560	15.4	2.2
T5D22	8	8.1	c	12.2	0.4	.00063	2.6	476.21	2.0	.0496	4.7	X	9744	56213	17.6	3.8
T5D22	7	7.2	b	12.3	0.4	.00063	2.8	463.68	2.0	.0477	4.5	X	12987	64225	24.1	1.9
T5D22	1	1.3	b	12.4	0.4	.00062	2.8	474.36	2.1	.0499	5.0	X	8075	56189	14.6	0.5
T5D22	3	3.1	c	12.5	0.3	.00062	2.6	482.40	2.1	.0558	3.8	X	11456	101725	20.4	0.0
T5D22	7	7.1	c	12.6	0.3	.00064	2.4	479.82	1.9	.0538	3.2	X	14567	112920	26.1	2.5
T5D22	9	9.1	b	12.9	0.4	.00065	3.0	484.74	2.1	.0629	4.4	X	9483	69708	16.8	2.9
T5D22	1	1.2	b	13.2	0.5	.00067	3.7	464.80	2.4	.0570	4.4	X	7697	56529	14.2	2.3
T5D22	4	4.1	c	13.2	0.4	.00067	3.2	470.39	2.0	.0546	4.0	X	9514	65533	17.4	2.3
T5D22	6	6.1	c	13.3	0.4	.00069	2.8	469.80	2.2	.0537	4.5	X	6826	49713	12.5	5.2
T5D22	1	1.1	c	13.6	0.4	.00068	2.8	467.58	2.2	.0497	5.0	X	7166	50416	13.2	1.8
T5D22	2	2.1	c	13.7	0.4	.00069	2.8	449.58	2.0	.0541	4.2		11338	93410	21.7	1.8
T5D22	4	4.2	b	14.3	0.8	.00073	5.8	446.77	5.1	.0555	3.7		12662	79368	24.3	3.8
T5D22	3	3.2	b	14.4	0.4	.00072	2.7	436.99	2.1	.0488	5.0		8481	61808	16.7	1.2

206*: radiogenic Pb, comm206: common Pb. TW: Tera-Wasserburg. See Fig. 7a, b and c.

Table DR5: Argon detailed data: (1) Dinggye sz biotites

Temperature °C	$^{40}Ar/^{39}Ar$	$^{38}Ar/^{39}Ar$	$^{37}Ar/^{39}Ar$	$^{36}Ar/^{39}Ar$ (10^{-3})	^{39}Ar (10^{--1}moles)	$F^{39}Ar$ released	$\%^{40}Ar^*$	$^{40}Ar^*/^{39}Ar$	Age Ma	± 1σ Ma
T5D6		Biotite		J= 0.009545						
700	10.613	0.117	0.071	31.736	0.37	1.08	11.49	1.22	20.87	0.93
750	9.469	0.077	0.033	21.975	0.07	1.30	31.23	2.96	50.22	3.12
800	3.657	0.059	0.029	8.246	0.27	2.09	32.86	1.20	20.57	0.86
833	2.614	0.057	0.028	6.153	0.41	3.30	29.74	0.78	13.34	0.59
866	1.620	0.058	0.016	2.735	0.94	6.07	48.93	0.79	13.60	0.25
900	1.072	0.059	0.011	1.206	2.01	11.99	64.95	0.70	11.95	0.14
933	0.882	0.059	0.009	0.756	5.00	26.73	72.48	0.64	10.98	0.06
966	0.775	0.057	0.010	0.422	6.87	46.98	81.41	0.63	10.83	0.05
1000	0.811	0.053	0.037	0.582	3.98	58.72	76.58	0.62	10.66	0.06
1033	0.862	0.046	0.062	0.768	2.50	66.10	71.77	0.62	10.62	0.09
1066	0.822	0.055	0.026	0.528	3.97	77.80	78.76	0.65	11.11	0.06
1100	0.797	0.058	0.013	0.257	3.96	89.47	88.09	0.70	12.06	0.05
1200	1.146	0.055	0.076	0.841	2.98	98.27	76.98	0.88	15.13	0.08
1400	9.163	0.058	0.151	25.794	0.59	100.00	16.70	1.53	26.17	0.70

Temperature °C	$^{40}Ar/^{39}Ar$	$^{38}Ar/^{39}Ar$	$^{37}Ar/^{39}Ar$	$^{36}Ar/^{39}Ar$ (10^{-3})	^{39}Ar (10^{-14}moles)	$F^{39}Ar$ released	$\%^{40}Ar^*$	$^{40}Ar^*/^{39}Ar$	Age Ma	± 1σ Ma
T5D10		Biotite		J= 0.009075						
700	89.484	0.298	0.062	255.904	0.02	0.28	15.48	13.85	213.58	29.52
750	121.297	0.198	0.177	349.873	0.02	0.51	14.76	17.90	271.58	44.71
800	137.679	0.119	0.102	410.268	0.05	1.20	11.93	16.43	250.77	9.93
850	66.842	0.094	0.048	192.334	0.15	3.27	14.95	9.99	156.57	3.17
900	15.712	0.066	0.025	43.236	0.76	13.57	18.57	2.92	47.15	0.51
950	8.854	0.064	0.021	22.438	1.39	32.40	24.90	2.20	35.74	0.66
1000	11.823	0.062	0.048	30.991	0.81	43.47	22.40	2.65	42.84	0.50
1050	5.060	0.059	0.015	11.535	2.71	80.26	32.25	1.63	26.52	0.14
1100	9.592	0.062	0.030	24.212	1.10	95.25	25.22	2.42	39.18	0.28
1200	91.639	0.104	0.227	258.173	0.18	97.72	16.74	15.34	235.21	7.06
1400	86.586	0.061	0.074	245.933	0.17	100.00	16.05	13.90	214.29	3.56

Temperature °C	$^{40}Ar/^{39}Ar$	$^{38}Ar/^{39}Ar$	$^{37}Ar/^{39}Ar$	$^{36}Ar/^{39}Ar$ (10^{-3})	^{39}Ar (10^{-14}moles)	$F^{39}Ar$ released	$\%^{40}Ar^*$	$^{40}Ar^*/^{39}Ar$	Age Ma	± 1σ Ma
T5D33		Biotite		J= 0.009545						
700	8.658	0.043	0.025	21.518	0.53	1.11	26.34	2.28	38.85	0.72
750	12.419	0.037	0.024	24.095	0.06	1.24	42.52	5.28	88.71	3.00
800	5.884	0.030	0.018	12.654	0.18	1.62	36.13	2.13	36.25	1.14
833	4.283	0.027	0.006	9.042	0.36	2.37	37.16	1.59	27.20	0.68
866	2.738	0.027	0.010	5.691	0.85	4.17	37.88	1.04	17.78	0.32
900	1.571	0.027	0.005	2.533	2.11	8.62	51.10	0.80	13.77	0.19
933	1.117	0.026	0.004	1.388	4.02	17.10	61.50	0.69	11.79	0.07
966	0.954	0.025	0.003	0.924	7.70	33.33	69.30	0.66	11.35	0.05
1000	0.939	0.025	0.007	0.749	5.57	45.08	74.35	0.70	11.98	0.06
1033	1.013	0.023	0.016	0.903	3.40	52.25	71.79	0.73	12.48	0.08
1066	1.054	0.024	0.011	0.816	2.94	58.44	75.29	0.79	13.61	0.07
1100	0.952	0.025	0.006	0.547	4.60	68.14	80.97	0.77	13.23	0.05
1200	0.929	0.025	0.006	0.553	12.98	95.51	80.30	0.75	12.80	0.03
1400	3.631	0.026	0.029	7.735	2.13	100.00	36.55	1.33	22.71	0.21

Temperature °C	$^{40}Ar/^{39}Ar$	$^{38}Ar/^{39}Ar$	$^{37}Ar/^{39}Ar$	$^{36}Ar/^{39}Ar$ (10^{-3})	^{39}Ar (10^{-14}moles)	$F^{39}Ar$ released	$\%^{40}Ar^*$	$^{40}Ar^*/^{39}Ar$	Age Ma	± 1σ Ma
T539b		Biotite		J= 0.009545						
700	24.060	0.226	0.003	51.331	0.02	0.41	36.87	8.87	146.65	12.33
750	36.924	0.111	0.006	71.221	0.01	0.55	42.95	15.86	254.29	30.47
800	15.588	0.042	0.003	42.496	0.03	1.20	19.31	3.01	51.11	7.67
833	5.862	0.032	0.002	14.103	0.09	3.35	28.57	1.68	28.62	2.76
866	2.877	0.027	0.002	6.727	0.21	8.14	30.23	0.87	14.91	1.12
900	1.608	0.025	0.001	2.424	0.44	18.31	54.21	0.87	14.95	0.51
933	1.416	0.024	0.002	2.445	0.80	36.62	47.54	0.67	11.55	0.29
966	1.211	0.022	0.002	1.608	0.53	48.69	59.13	0.72	12.29	0.40
1000	1.614	0.022	0.005	2.146	0.35	56.77	59.49	0.96	16.45	0.60
1033	1.833	0.024	0.003	2.283	0.32	64.15	62.11	1.14	19.50	0.59
1066	1.445	0.023	0.003	1.908	0.43	74.02	59.62	0.86	14.78	0.44
1100	1.205	0.020	0.001	1.209	0.40	83.31	68.70	0.83	14.20	0.35
1200	1.303	0.020	0.019	1.441	0.58	96.58	65.89	0.86	14.73	0.30
1400	18.335	0.030	0.038	55.020	0.15	100.00	11.23	2.06	35.12	2.11

$^{40}Ar^*$: radiogenic ^{40}Ar. See Fig. 8 and Fig. DR9

Table DR5: Argon detailed data: (2) Kartha sz biotites

Temperature °C	$^{40}Ar/^{39}Ar$	$^{38}Ar/^{39}Ar$	$^{37}Ar/^{39}Ar$	$^{36}Ar/^{39}Ar$ (10^{-3})	^{39}Ar (10^{-14}moles)	$F^{39}Ar$ released	$\%^{40}Ar^*$	$^{40}Ar^*/^{39}Ar$	Age Ma	± 1σ Ma
T07A10		Biotite		J= 0.009545						
700	14.191	0.134	0.043	42.768	0.24	2.15	10.82	1.54	26.26	1.32
750	18.578	0.104	0.105	50.921	0.02	2.37	18.93	3.52	59.58	10.01
800	8.115	0.085	0.025	15.843	0.06	2.90	42.09	3.42	57.88	3.63
833	4.558	0.083	0.019	11.254	0.16	4.30	26.62	1.21	20.78	1.73
866	2.427	0.081	0.029	5.745	0.52	9.03	29.31	0.71	12.21	0.46
900	1.208	0.082	0.023	2.132	1.29	20.73	46.33	0.56	9.61	0.22
933	0.764	0.083	0.008	0.872	3.30	50.60	63.72	0.49	8.37	0.09
966	0.626	0.082	0.005	0.326	2.44	72.66	81.45	0.51	8.76	0.09
1000	1.010	0.078	0.022	1.026	0.60	78.08	68.10	0.69	11.80	0.35
1033	1.076	0.077	0.017	1.224	0.49	82.54	64.64	0.70	11.94	0.38
1066	0.897	0.081	0.008	0.674	0.73	89.16	75.64	0.68	11.65	0.23
1100	0.779	0.083	0.004	0.560	0.75	95.96	76.20	0.59	10.19	0.19
1200	1.223	0.082	0.018	0.956	0.38	99.41	75.36	0.92	15.80	0.32
1400	26.812	0.085	0.029	81.607	0.07	100.00	9.99	2.68	45.56	3.84

Temperature °C	$^{40}Ar/^{39}Ar$	$^{38}Ar/^{39}Ar$	$^{37}Ar/^{39}Ar$	$^{36}Ar/^{39}Ar$ (10^{-3})	^{39}Ar (10^{-14}moles)	$F^{39}Ar$ released	$\%^{40}Ar^*$	$^{40}Ar^*/^{39}Ar$	Age Ma	± 1σ Ma
T07A14		Biotite		J= 0.009545						
700	1.562	0.062	0.027	2.864	2.14	15.58	44.64	0.70	11.97	0.14
750	2.196	0.061	0.017	2.980	0.22	17.16	59.04	1.30	22.19	0.94
800	2.520	0.065	0.017	1.900	0.13	18.08	76.97	1.94	33.10	1.24
833	1.822	0.064	0.012	3.081	0.18	19.40	48.98	0.89	15.31	1.19
866	0.994	0.062	0.006	1.148	0.55	23.41	63.89	0.63	10.90	0.36
900	0.639	0.063	0.006	0.401	2.33	40.36	78.38	0.50	8.60	0.10
933	0.613	0.063	0.006	0.396	3.93	68.89	77.72	0.48	8.19	0.07
966	0.644	0.060	0.018	0.381	1.54	80.10	79.56	0.51	8.80	0.14
1000	0.970	0.050	0.072	0.860	0.59	84.37	72.19	0.70	12.02	0.34
1033	0.938	0.053	0.040	0.740	0.66	89.19	74.80	0.70	12.04	0.28
1066	0.928	0.059	0.020	0.246	0.74	94.55	90.16	0.84	14.36	0.14
1100	1.170	0.061	0.017	0.234	0.45	97.78	92.48	1.08	18.53	0.15
1200	4.141	0.051	0.144	1.097	0.23	99.44	91.90	3.81	64.37	0.39
1400	27.245	0.063	0.183	68.253	0.08	100.00	25.94	7.07	117.78	2.80

Temperature °C	$^{40}Ar/^{39}Ar$	$^{38}Ar/^{39}Ar$	$^{37}Ar/^{39}Ar$	$^{36}Ar/^{39}Ar$ (10^{-3})	^{39}Ar (10^{-14}moles)	$F^{39}Ar$ released	$\%^{40}Ar^*$	$^{40}Ar^*/^{39}Ar$	Age Ma	± 1σ Ma
T07A19		Biotite		J= 0.009545						
700	45.415	0.165	0.079	145.736	0.09	0.49	5.14	2.33	39.76	4.15
750	25.326	0.083	0.099	74.153	0.05	0.74	13.42	3.40	57.62	5.13
800	15.626	0.038	0.089	44.213	0.06	1.05	16.30	2.55	43.34	3.91
833	11.319	0.033	0.105	27.821	0.09	1.53	27.25	3.08	52.35	2.62
866	8.893	0.036	0.147	22.267	0.16	2.41	25.89	2.30	39.22	1.59
900	6.765	0.029	0.048	17.676	0.37	4.43	22.54	1.53	26.07	0.83
933	3.394	0.023	0.013	6.768	1.94	15.05	40.51	1.37	23.52	0.20
966	2.119	0.021	0.007	2.301	3.33	33.27	66.98	1.42	24.27	0.12
1000	2.211	0.021	0.010	2.519	2.09	44.72	65.45	1.45	24.74	0.15
1033	2.762	0.021	0.018	4.476	1.26	51.62	51.44	1.42	24.30	0.19
1066	2.376	0.022	0.018	3.103	1.35	59.03	60.61	1.44	24.63	0.20
1100	1.842	0.020	0.011	1.421	4.89	85.78	76.15	1.40	23.99	0.07
1200	1.854	0.020	0.043	1.032	2.33	98.54	82.61	1.53	26.18	0.11
1400	21.353	0.032	0.129	60.811	0.27	100.00	15.79	3.37	57.13	1.17

Temperature °C	$^{40}Ar/^{39}Ar$	$^{38}Ar/^{39}Ar$	$^{37}Ar/^{39}Ar$	$^{36}Ar/^{39}Ar$ (10^{-3})	^{39}Ar (10^{-14}moles)	$F^{39}Ar$ released	$\%^{40}Ar^*$	$^{40}Ar^*/^{39}Ar$	Age Ma	± 1σ Ma
T07A33		Biotite		J= 0.009545						
700	18.721	0.100	0.079	45.646	0.21	1.32	27.87	5.22	87.68	1.39
750	11.356	0.057	0.057	29.542	0.10	1.97	22.98	2.61	44.39	2.39
800	6.117	0.046	0.054	13.402	0.24	3.44	34.98	2.14	36.48	1.38
833	6.655	0.049	0.044	15.243	0.42	6.02	32.06	2.13	36.37	0.72
866	3.609	0.052	0.032	7.315	0.57	9.57	39.60	1.43	24.44	0.45
900	1.811	0.059	0.020	3.463	1.35	17.93	42.47	0.77	13.20	0.19
933	1.287	0.065	0.017	2.255	2.40	32.86	46.74	0.60	10.33	0.13
966	0.963	0.063	0.021	1.155	2.51	48.48	62.59	0.60	10.35	0.10
1000	1.107	0.047	0.042	1.497	1.91	60.31	58.45	0.65	11.10	0.14
1033	1.113	0.046	0.032	1.492	2.13	73.52	58.77	0.65	11.23	0.12
1066	1.068	0.060	0.022	1.248	1.97	85.76	63.70	0.68	11.67	0.12
1100	1.262	0.066	0.022	1.079	0.99	91.93	73.26	0.92	15.85	0.18
1200	5.480	0.049	0.143	2.566	0.88	97.40	85.96	4.71	79.35	0.25
1400	14.665	0.045	0.131	20.064	0.42	100.00	59.49	8.72	144.31	0.60

$^{40}Ar^*$: radiogenic ^{40}Ar. See Fig. 8 and Fig. DR9

Table DR5: Argon detailed data: (3) Kharta sz Muscovites

Temperature °C	$^{40}Ar/^{39}Ar$	$^{38}Ar/^{39}Ar$	$^{37}Ar/^{39}Ar$	$^{36}Ar/^{39}Ar$ (10^{-3})	^{39}Ar (10^{-14}moles)	$F^{39}Ar$ released	$\%^{40}Ar^*$	$^{40}Ar^*/^{39}Ar$	Age Ma	± 1σ Ma
T07A20		Muscovite		J= 0.009545						
700	12.813	0.075	0.000	30.953	0.23	0.35	28.46	3.65	61.72	1.90
750	8.544	0.041	0.007	19.803	0.10	0.50	31.28	2.67	45.45	2.23
800	2.812	0.015	0.012	5.603	0.26	0.89	40.44	1.14	19.48	0.97
833	1.570	0.014	0.014	3.061	0.43	1.54	41.19	0.65	11.10	0.50
866	1.066	0.013	0.010	1.786	0.70	2.59	48.68	0.52	8.91	0.34
900	0.844	0.014	0.006	1.350	1.42	4.71	50.40	0.43	7.31	0.17
933	0.836	0.014	0.006	1.623	2.11	7.86	40.27	0.34	5.79	0.16
966	0.646	0.013	0.004	0.920	3.29	12.78	54.87	0.35	6.10	0.08
1000	0.686	0.013	0.003	0.818	6.18	22.03	61.88	0.42	7.30	0.05
1033	0.562	0.013	0.002	0.496	9.11	35.66	70.38	0.40	6.80	0.04
1066	0.494	0.013	0.002	0.336	9.83	50.36	75.91	0.38	6.45	0.03
1100	0.494	0.013	0.002	0.318	10.54	66.13	76.94	0.38	6.53	0.03
1200	0.614	0.013	0.003	0.276	20.11	96.22	83.51	0.51	8.81	0.02
1400	3.114	0.014	0.043	5.177	2.53	100.00	50.31	1.57	26.78	0.15

Temperature °C	$^{40}Ar/^{39}Ar$	$^{38}Ar/^{39}Ar$	$^{37}Ar/^{39}Ar$	$^{36}Ar/^{39}Ar$ (10^{-3})	^{39}Ar (10^{-14}moles)	$F^{39}Ar$ released	$\%^{40}Ar^*$	$^{40}Ar^*/^{39}Ar$	Age Ma	± 1σ Ma
T07A20		Muscovite rusty		J= 0.009545						
700	32.504	0.071	0.003	73.580	0.09	0.45	33.05	10.74	176.09	2.35
750	13.168	0.020	0.019	26.957	0.07	0.80	39.36	5.18	87.12	2.19
800	3.934	0.014	0.027	8.204	0.23	1.91	37.90	1.49	25.50	0.57
833	2.277	0.012	0.039	3.377	0.42	3.94	55.41	1.26	21.60	0.29
866	1.968	0.013	0.027	4.017	1.00	8.85	38.76	0.76	13.09	0.26
900	1.190	0.013	0.011	2.143	1.22	14.84	45.14	0.54	9.22	0.15
933	1.047	0.014	0.095	1.893	1.65	22.92	45.25	0.47	8.14	0.10
966	0.890	0.013	0.108	1.182	2.00	32.72	59.25	0.53	9.06	0.07
1000	0.868	0.013	0.112	0.898	3.50	49.87	67.91	0.59	10.12	0.05
1033	1.009	0.013	0.099	0.745	4.25	70.71	76.79	0.77	13.29	0.05
1066	1.832	0.013	0.096	0.927	2.81	84.45	84.27	1.54	26.40	0.06
1100	3.395	0.013	0.159	1.265	1.21	90.40	88.68	3.01	51.12	0.14
1200	6.872	0.014	0.567	1.920	1.64	98.44	91.95	6.32	105.69	0.19
1400	55.813	0.025	4.014	56.509	0.32	100.00	70.48	39.44	576.43	2.01

Temperature °C	$^{40}Ar/^{39}Ar$	$^{38}Ar/^{39}Ar$	$^{37}Ar/^{39}Ar$	$^{36}Ar/^{39}Ar$ (10^{-3})	^{39}Ar (10^{-14}moles)	$F^{39}Ar$ released	$\%^{40}Ar^*$	$^{40}Ar^*/^{39}Ar$	Age Ma	± 1σ Ma
T7A48b		Muscovite		J= 0.009545						
700	39.014	0.116	0.045	42.389	0.15	1.78	67.85	26.47	406.42	2.04
750	10.995	0.045	0.022	12.226	0.07	2.65	66.97	7.36	122.55	2.63
800	4.610	0.017	0.042	6.052	0.16	4.58	60.83	2.80	47.66	1.65
833	3.619	0.015	0.029	3.980	0.18	6.76	67.00	2.42	41.28	1.09
866	5.044	0.015	0.029	4.287	0.28	10.24	74.52	3.76	63.59	1.00
900	1.972	0.014	0.019	2.395	0.32	14.14	63.15	1.25	21.31	0.57
933	2.459	0.016	0.014	4.677	0.37	18.72	43.01	1.06	18.12	0.65
966	1.689	0.013	0.008	1.671	0.45	24.24	69.60	1.18	20.12	0.43
1000	1.213	0.013	0.002	1.142	1.48	42.45	70.56	0.86	14.68	0.18
1033	1.020	0.013	0.001	0.940	1.43	60.03	70.83	0.72	12.41	0.15
1066	1.226	0.013	0.004	0.893	0.79	69.80	76.86	0.94	16.16	0.21
1100	1.441	0.014	0.001	1.000	0.37	74.28	78.12	1.13	19.28	0.33
1200	1.816	0.013	0.002	1.234	1.69	95.12	78.83	1.43	24.48	0.14
1400	29.216	0.022	0.006	31.557	0.40	100.00	68.02	19.87	313.33	0.90

Temperature °C	$^{40}Ar/^{39}Ar$	$^{38}Ar/^{39}Ar$	$^{37}Ar/^{39}Ar$	$^{36}Ar/^{39}Ar$ (10^{-3})	^{39}Ar (10^{-14}moles)	$F^{39}Ar$ released	$\%^{40}Ar^*$	$^{40}Ar^*/^{39}Ar$	Age Ma	± 1σ Ma
T07A48b		Muscovite rusty		J= 0.009545						
700	37.083	0.064	0.113	108.854	0.44	4.28	13.22	4.90	82.53	1.74
800	9.114	0.034	0.100	25.748	0.48	8.93	16.37	1.49	25.51	0.84
850	4.214	0.019	0.092	12.013	0.74	16.10	15.41	0.65	11.15	0.39
900	4.253	0.016	0.064	12.046	1.24	28.10	15.92	0.68	11.62	0.35
950	2.552	0.015	0.054	6.329	1.38	41.37	26.05	0.66	11.41	0.30
1000	2.140	0.015	0.021	4.889	1.61	56.91	31.60	0.68	11.61	0.19
1050	1.394	0.014	0.009	2.337	2.88	84.68	49.09	0.68	11.75	0.12
1100	1.660	0.015	0.013	2.274	0.64	90.84	58.35	0.97	16.60	0.32
1200	1.544	0.016	0.015	1.964	0.75	98.03	61.17	0.94	16.19	0.28
1400	17.267	0.022	0.007	39.414	0.20	100.00	32.44	5.60	93.95	1.49

$^{40}Ar^*$: radiogenic ^{40}Ar. See Fig. 8 and Fig. DR9

Table DR6: (U-Th)/He data

Sample	Elevation (m)	Replicate	nb grains	U (ppm)	Th (ppm)	He (nmol/g)	Radius (μm)	Lengh (μm)	Ft	Raw age (Ma)	Corr Age (Ma)	Mean age (Ma)	1σ error (Ma)
T5D01	5217											3.3	0.3[(2)]
		T5D01-1	1	134.8	2.9	2.16	126.0	288	0.89	2.9	3.3		
T5D22	5348											3.8	0.2[(1)]
		TSD22-1	1	36.0	6.8	0.67	63.0	216	0.78	3.2	4.2		
		TSD22-2	1	40.8	8.4	0.68	54.0	297	0.76	2.9	3.8		
		TSD22-3	*1*	*37.7*	*4.7*	*2.85*	*85.5*	*378*	*0.84*	*13.4*	*16.0*		
		T5D22-4	1	27.2	6.7	0.41	58.5	162	0.77	2.6	3.4		
		T5D22-5	1	54.7	5.6	0.91	58.5	144	0.76	3.0	3.9		
T5D26	5419											3.4	0.2[(1)]
		TSD26-1	1	108.9	29.1	1.67	49.5	216	0.73	2.6	3.6		
		TSD26-2	1	88.0	47.8	1.23	45.0	243	0.71	2.3	3.2		
		TSD26-3	1	35.3	4.0	0.59	63.0	297	0.79	3.0	3.8		
		TSD26-4	1	77.5	21.4	1.05	72.0	351	0.81	2.3	2.9		
T5D40	4270											3.2	0.1[(1)]
		TSD40-1	1	51.5	11.6	0.69	45.0	243	0.71	2.3	3.2		
		TSD40-2	1	45.7	19.6	0.61	45.0	162	0.70	2.2	3.2		

nb grains: number of grains used for each replicate
Age in italics is considered as an outlier and was not used for mean age calculation.
Ft: alpha ejection correction after Farley et al. (1996)
The 1σ error is taken either as (1) the standard deviation of the replicate analyses divided by $(n-1)^{1/2}$ where n is the number of replicate analyses performed, or (2) as 10% of the mean age (sample with only one replicate).

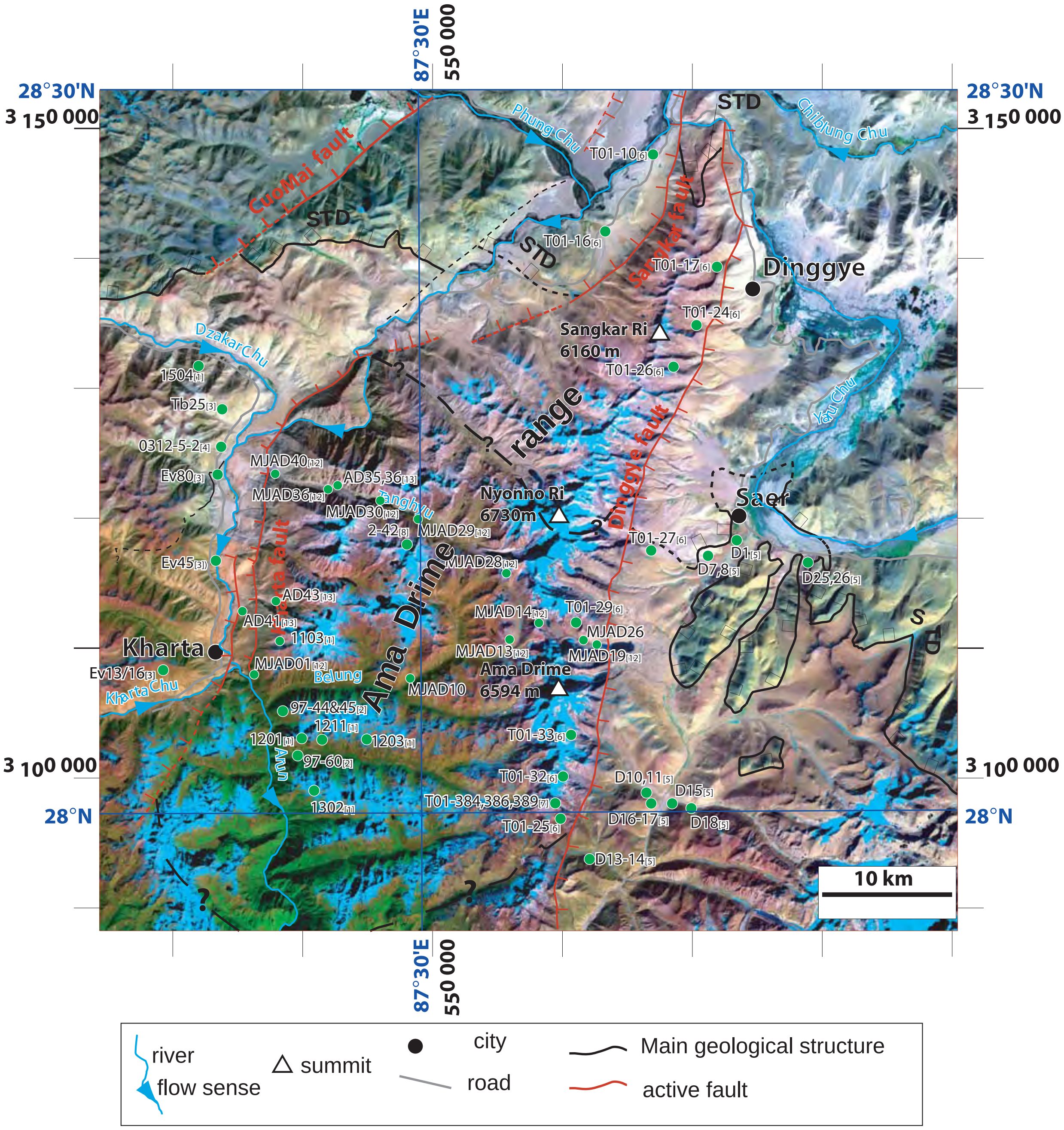

Figure DR7: Landsat image corresponding to Fig. 2a.

Composite R (Chanel 7), V (Chanel 4), B (Chanel 2) Landsat TM image. Major structures as on Fig. 2a. Samples from the literature discussed in text are located. [1] Liu et al., 2007 (samples 1504, 1211, 1201, 1302); [2] Lombardo and Rolfo, 2000 (samples 97-44 and 97-45); [3] Borghi et al., 2003 (samples Ev 13, 16, 45, 80); [4] Li et al., 2003 (sample 0312-5-2); [5] Hodges et al., 1994 (samples D1, 7, 8, 10,11,13,14,15,16,17,18, 25,26); [6] Zhang and Guo, 2007 (samples T01-10, 16, 24, 25, 26, 27, 29, 32, 33); [7] Liu et al., 2005 (samples T01-384, 386, 389); [8] Groppo et al., 2007 (samples EV02-42, 45).[12] Jessup et al., 2008 (samples MJAD1, 10, 13, 14, 19, 26, 30, 36, 40). [13] Cottle et al., 2009 (samples AD35, 36, 41 & 43).

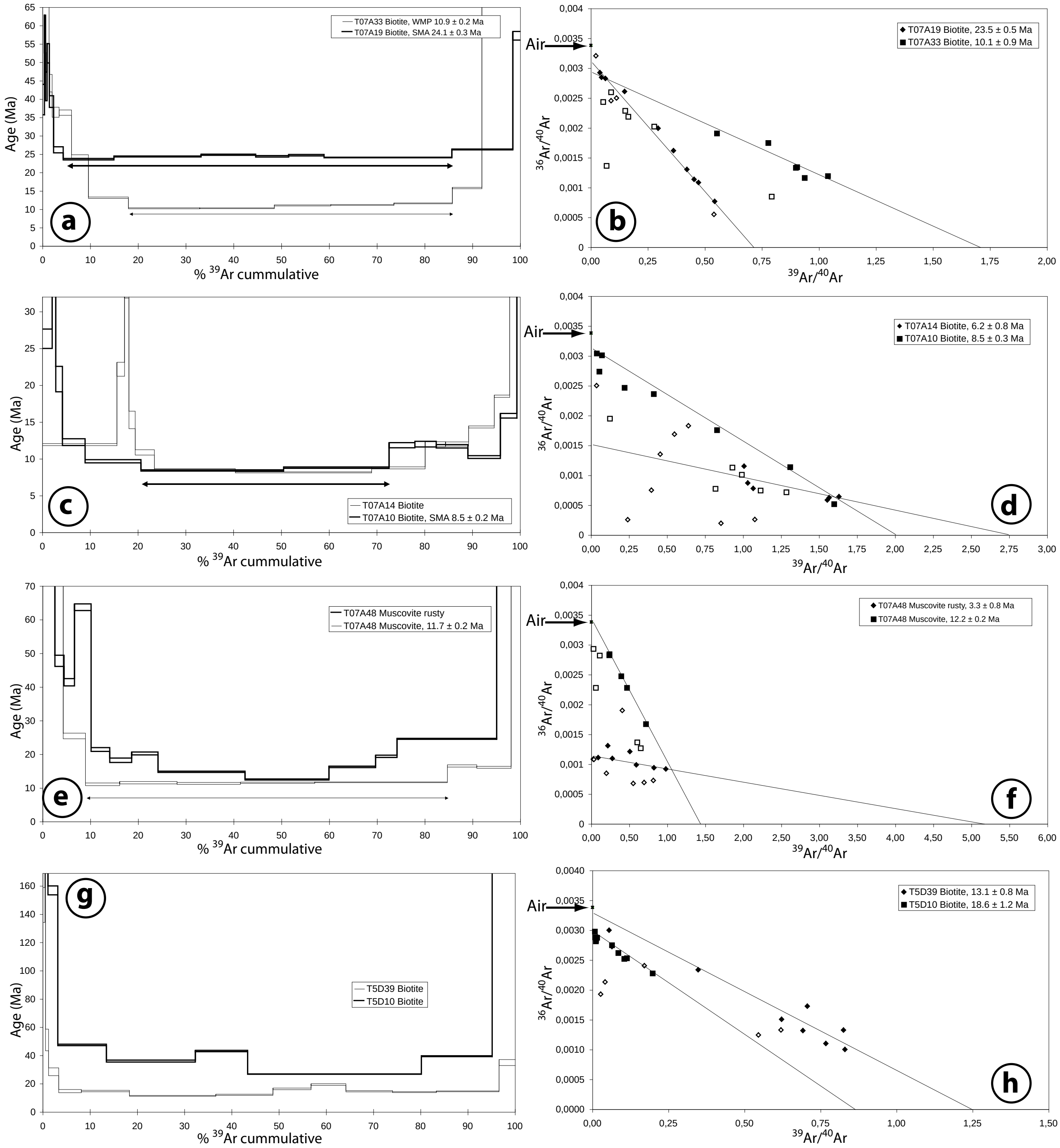

Figure DR8: Argon Data

See table DR5 for detailed data. For inverse isochron plots, empty symbols where not used in the regression calculation. a, b) T7A33 and T7A19 biotites age spectra and inverse isochrons. c,d) T7A14 and T7A10 biotites age spectra and inverse isochrones. e,f) T7A48 muscovites (normal and rusty) age spectra and inverse isochrone. g,h) T5D39 and T5D10 biotites age spectra and inverse isochrone.